



Project Documentation
Report #0021
Revision A

ATST Site Survey Working Group Final Report



Site Survey Working Group

Oct. 6, 2004

Revision Summary:

1. Date: Oct. 6, 2004
Revision: A
Changes: Original release
2. Date:
Revision:
Changes:
3. Date:
Revision:
Changes:

Contributors

Site Survey Working Group:

Jacques Beckers, University of Chicago (Ex-Chair)
Tim Brown, High Altitude Observatory (Chair)
Manuel Collados, Instituto Astrofisica de Canarias
Carsten Denker, New Jersey Institute of Technology
Frank Hill, National Solar Observatory
Jeff Kuhn, University of Hawaii
Matt Penn, National Solar Observatory
Hector Socas-Navarro, High Altitude Observatory
Dirk Soltau, Kippenheuer Institute
Kim Streander, High Altitude Observatory

Other major contributions were made by:

Peter Brandt, Kippenheuer Institute
John Briggs, University of Chicago/National Solar Observatory
Matthew Dawson, Brockton High School, Brockton MA
Steve Fletcher, National Solar Observatory
Jill Gerke, University of Arizona
Robert Hammerschlag, Utrecht
Mark Komsa, National Solar Observatory
Haosheng Lin, University of Hawaii
Steve Hegwer, National Solar Observatory
David Hiriart, Observatorio Astronomico Nacional, UNAM
Alice Lecinski, High Altitude Observatory
Bill Marquette, Big Bear Solar Observatory
Raul Michael, Observatorio Astronomico Nacional, UNAM
Don Mickey, University of Hawaii
Kimberly Moody, University of Arizona
Steven Ocnley, Atmospheric Technology Division, NCAR
Richard Radick, USAF
Thomas Rimmele, National Solar Observatory
Liu Zhong, Yunnan Observatory

Table Of Contents

1.	Executive Summary	1
2.	Goals	10
3.	Scientific Requirement GOALS.....	11
3.1	Seeing	11
3.2	Sky brightness and IR.....	12
4.	Brief History of the SSWG	14
5.	Preliminary Selection Process	14
6.	Description of the Sites	16
6.1	Big Bear Lake, California.....	16
6.2	Haleakala, Hawaii	19
6.3	La Palma, Canary Islands, Spain.....	21
6.4	Panguitch Lake, Utah	23
6.5	Sacramento Peak, New Mexico.....	25
6.6	San Pedro Martir, Baja California, Mexico.....	27
7.	Historical Data and Long Term Trends.....	29
8.	Instrumentation and Operations	31
8.1	S-DIMM and SHABAR	31
8.2	Sky Brightness Monitor.....	32
8.3	Dust Counter.....	33
8.4	Weather Station	33
8.5	Test Stand.....	33
8.6	Technical Staff	35
8.7	Deployment and Maintenance History	35
8.7.1	Instrument configurations	35
8.7.2	Major Instrument Events.....	36
8.8	Calibration and testing.....	37
8.8.1	Validation tests, Assembly level	37
8.8.2	Validation tests, end-to-end system level.....	38
8.8.3	Certification tests	38
8.8.4	Results of SHABAR assembly tests and calibration.....	38
8.8.5	S-DIMM Plate Scale Measurements	41
9.	Data Reduction	41
9.1	Ingest	41
9.2	Data Culling and Flags	42
9.3	SHABAR/S-DIMM Analysis.....	42
9.3.1	The Inversion Methods.....	44
9.3.2	Verification Tests	49
9.4	SBM Analysis.....	55
9.4.1	Overview of Data Analysis	55
9.4.2	Details of the “Global Calibration” Technique	57
9.4.3	Extrapolation to compute IRspec	62
9.5	Clear Time Fraction.....	63
9.6	Statistics.....	64
9.7	Time Block Distribution.....	64
9.8	Correction for Observing Schedule and Weather.....	64
10.	Results	66

10.1	Data Coverage.....	66
10.2	Seeing	67
10.2.1	Seeing Time Distribution	70
10.3	Clear Time	82
10.4	Sky Brightness	83
10.4.1	Results of the Global Calibration Analysis	83
10.4.2	Extrapolation from the IR requirement to measured values.....	87
10.4.3	Comparison with Sky Brightness Goals.....	89
10.4.4	Caveats and Future Work.....	91
10.5	Water Vapor.....	96
10.6	Dust.....	97
10.7	Meteorology.....	97
10.8	Conclusions.....	98
11.	Acknowledgments.....	98
12.	References	98
13.	Appendices	99
13.1	Seeing instrumentation paper (Exp. Astron.).....	99
13.2	Cn2 analysis report (RPT-0014)	99
13.3	Hector's Integral	99
13.4	Crane test details.....	99
13.5	Haleakala stellar DIMM data.....	99
13.6	SBM instrumentation paper	99
13.7	SBM analysis paper	99
13.8	VSP Calibration	99
13.9	Quick-look plot example	99
13.10	La Palma height comparison.....	99
13.11	Dependence of seeing on season, time of day, wind speed, wind direction	99
13.12	Weather statistics	99
13.13	High-altitude winds.....	99
13.14	Dust statistics	99

1. EXECUTIVE SUMMARY

This report contains the final results of the ATST site survey, initiated in 2000 to determine the location of the Advanced Technology Solar Telescope. This report supersedes ATST RPT-0016, *ATST Site Survey Working Group Interim Report*. The interim report contained results from analyses that are now known to be incomplete. Note that even with this extensive survey, there are still caveats. The data presented here were collected over too short a period to reflect long-term temporal variations. Also, the tests were limited to only six promising sites.

The results of this report come from a measurement and analysis technique that uses an array of scintillometers to estimate the seeing as a function of height above the ground. A considerable amount of effort has gone into testing and verifying the method, and the Working Group is of the opinion that the method gives an acceptable estimate up to a height of 50 m above the ground. This report contains the results of the verification tests, as well as two independent approaches to the analysis to allow the reader to judge the level of uncertainty in the results.

The ATST Site Survey Working Group (SSWG) has overseen the development and construction of instrumentation to measure daytime solar seeing, sky brightness, clear time fraction, dust levels, and water vapor content. These quantities have been measured at six candidate sites:

- Big Bear Solar Observatory, California
- Mees Solar Observatory, Haleakala, Hawaii
- Observatorio Roque de los Muchachos, La Palma, Canary Islands, Spain
- Panguitch Lake, Utah
- Sacramento Peak Observatory, Sunspot, NM
- Observatorio Astronomico Nacional, San Pedro Martir, Baja California, Mexico

These six sites were selected from an initial list of 72 candidates. The list was culled down primarily by considerations of feasibility and observing conditions. In a few cases, site visits eliminated candidates on the basis of changing environmental conditions, particularly drought. The six tested sites represent a cross-section of geographical locales: continental mountain (Sac Peak), continental mountain lake (Panguitch), peninsula mountain (San Pedro), coastal mountain lake (Big Bear), Atlantic island mountain (La Palma), and Pacific island mountain (Haleakala).

With the release of the interim report it became clear that the six sites could be grouped into two classes based on the observing conditions. A meeting of the ATST Science Working Group in November 2003 resulted in the recommendation that testing be continued only at the top group of sites (Big Bear, Haleakala, and La Palma). Thus those sites have an additional year of data included in this report, and are the main subject of the final report. Note that the overall classification of the sites into two groups remained unchanged when the improved seeing analysis was applied to all six sites.

As of August 31, 2004 data have been collected over various time periods at the six sites ranging in length from 0.5 to 2.1 years (1.9 to 2.1 years for the top group of sites) to determine which sites fulfill the scientific site requirement goals for the ATST. Those goals are:

- Clear daytime fraction of 70%, 3000 hours annual sunshine.
- 1800 annual hours with r_0 (500 nm) > 7 cm (measured at the telescope aperture), including at least 100 continuous 2-hr periods.
- 200 annual hours with r_0 (500 nm) > 12 cm (measured at the telescope aperture) including at least 10 continuous 4-hr periods.

- Large isoplanatic angle, i.e., good atmospheric conditions at high altitudes.
- 480 annual hours with a sky brightness less than or equal to 25 ± 10 millionths at 1.1 radii at 1 micron with a radial profile equal to or steeper than $R^{-0.8}$, including at least 40 continuous 4 hour periods.
- 600 annual hours with the precipitable water vapor below 5 mm, including at least 40 continuous 4-hour periods.

The instrumentation used for the survey comprised two major pieces – a seeing monitor, and a sky brightness monitor. The seeing monitor included two components: a solar differential image motion monitor (S-DIMM), and an array of six scintillometers known as the shadow band ranger (SHABAR). Both seeing monitor components were designed and developed by Jacques Beckers and constructed at Sac Peak Observatory. The S-DIMM measures the total value of r_0 integrated from the observing height to the top of the atmosphere with no height weighting of $C_n^2(h)$. The SHABAR measures the steady and fluctuating intensity of sunlight in six detectors giving the clear time fraction and a measure of the seeing with $C_n^2(h)$ weighted towards lower heights h by a factor $h^{-1/3}$. The SHABAR also measures the cross-covariance of scintillation between the 15 possible pairs of detectors which are arranged in a non-redundant array. These covariances are used to estimate $C_n^2(h)$ and hence r_0 as a function of height above the 8-m height at which the seeing monitor entrance aperture is mounted. Since the height of the ATST primary mirror is expected to be around 25 m, the inferred $r_0(h)$ is a vital piece of information. The seeing monitor is mounted on a substantial 6-m tall test stand that is designed such that the dominant motion of the instrument platform is a horizontal translation without tilting. The additional height of the telescope pier and telescope itself places the entrance aperture of the seeing monitor at 8 m above the ground. The sampling time and cadence of the seeing monitor is 10 sec.

The sky brightness monitor (SBM) comprises a miniature coronagraph that compares the sky brightness in three wavelength bands (450, 530, and 890 nm) to the solar disk intensity. The SBM was designed and developed by Haosheng Lin and constructed at the Institute for Astronomy in Hawaii. It is sensitive to sky brightness below 1×10^{-6} of disk center intensity with a field of view of 4 to 8 solar radii. It also provides an intensity measurement in the 940-nm water vapor absorption band. In addition to the SBM, a commercial dust counter was installed to count particulates in five size ranges (0.3, 0.5, 1, 2, and 3 microns). The dust counter was mounted at the 6-m height of the top of the seeing monitor test stand, while the SBM was located at ground level.

In addition to the seeing monitor and SBM, a weather station recorded wind speed, wind velocity, pressure, relative humidity, and temperature at two locations (top and bottom of the test stand).

Calibration of the S-DIMM instrument consisted of measuring the plate scale of the detector using observations of double stars. The SHABAR detectors were tested using generated laboratory signals as inputs and standard electronic measuring devices and techniques for the outputs. In addition, all field units were run for a brief period co-located with a constant “standard” unit at Sac Peak. Similar tests were performed for the SBM in Hawaii before shipment.

The data analysis to estimate $r_0(h)$ proved to be challenging. It essentially comprises the fitting of the observed cross-covariances as a function of detector separation with a model of the structure function, $C_n^2(h)$, composed of weighting functions derived from the theory of atmospheric turbulence. In addition, the integral of the model over the atmosphere is required to fit the observed S-DIMM value of r_0 , and the total observed scintillation. This requires the inclusion of an estimate of high-altitude seeing. Several tests of the analysis have been performed -- simulations, comparisons between simultaneous SHABAR/S-DIMM r_0 estimates at different heights, and comparison with in-situ measurements of C_n^2 . In all cases the analysis appears to provide a reasonable estimate of $r_0(h)$. This report contains the results of the

verification tests as well as two independent inversions of the seeing data so that the reader can judge the reliability of the results.

The SBM analysis to obtain sky brightness measurements involves the extraction of portions of the recorded images, averaging, correction for extinction and air mass, and fitting for radial and wavelength power laws. These power-law exponents are then used to extrapolate the sky brightness at the location and wavelength specified in the science requirements. This analysis also was challenging, primarily due to instrumental difficulties.

The clear time fraction (CTF) is estimated from the steady intensity level of the scintillometers in the SHABAR. The estimated CTF is sensitive to how certain instrumental data flags are interpreted: either as clouds, or as instrumental outages. When the flags are designated as instrumental outages, we find very good agreement between the CTF estimated here and those estimated by the earlier GONG site survey. Since the two methods of treating the flags represent the upper and lower limits of the CTF, we report the results from both treatments of the data.

An effort was made to reduce the impact of site-specific observing habits, equipment outages, and bad weather on the extrapolation of the measured seeing statistics to estimates of annualized hours of quality observing conditions. Once the relevant measurements are estimated for each sample, corrections are applied to the data to obtain the summary quantities that are shown in the following figures and table. The figures in this executive summary show a few of the seeing (Figures ES.1 and ES.2) and sky brightness (Figures ES.3 and ES.4) characteristics of the sites, as summarized in the captions. The summary tables contain the statistical outline of the seeing (Table 1) and sky brightness (Table 2) results. In addition to these overall summaries, this report contains detailed information on the statistical dependence of seeing as a function of time of day, time of year, wind speed and wind direction.

A striking result of the seeing analysis is the qualitative difference between the Big Bear site and the sites on Haleakala and La Plama (or more generically, between lake sites and island mountain sites). Many seeing properties, including the distributions of near-ground-level turbulence and the contribution from high-altitude scintillation, are systematically different between the two kinds of site. Based on the studies described in this report, the SSWG is satisfied that these differences are real, and result from the absence of a near-surface layer of solar-heated air at Big Bear. Earlier studies have suggested such a difference between lake sites and mountain sites, and the current work confirms this distinction.

The ATST site survey is one of the few comparative studies of solar site characteristics, and has been done with new instrumental and analysis techniques that can provide new details about the height dependence of the atmospheric turbulence. The reader should keep in mind the limitations of this work: the short observational time span, and the limited number of sites that have been tested.

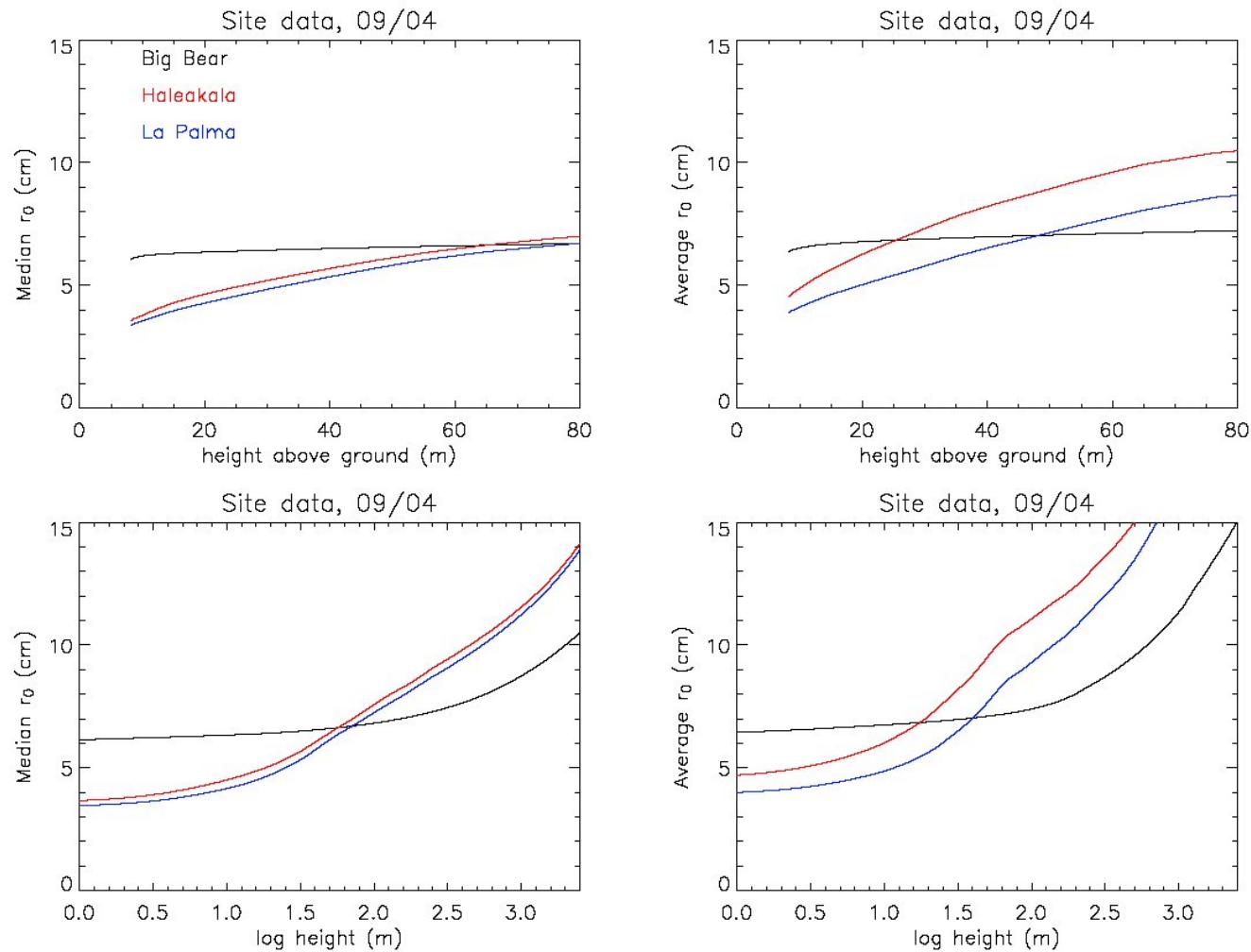


Figure ES.1 – These plots show the behavior of r_0 as a function of height as derived from the SHABAR and S-DIMM analysis. The left column shows the median values for each site; the right column shows the average r_0 . The bottom row is on a logarithmic height scale to show high-altitude seeing, and the top row is on a linear scale to show the low-level seeing.

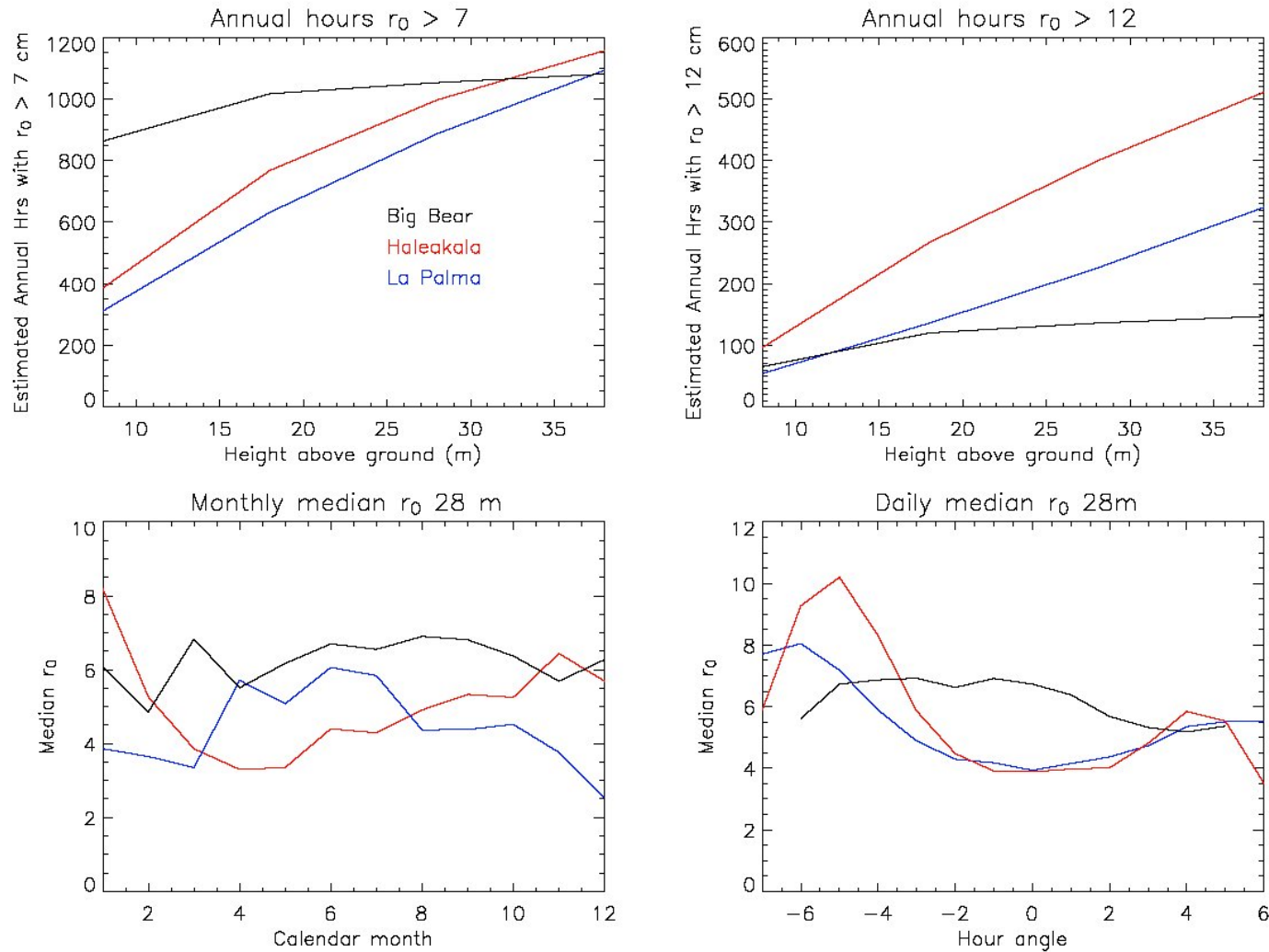


Figure ES.2 – These plots show some temporal characteristics of r_0 at the sites. The top row shows the corrected estimated annual number of hours during which r_0 was greater than 7 cm (upper left panel) or 12 cm upper right (right panel) as a function of height above the ground. The qualitative difference between the lake site (Big Bear) and the mountain sites (Haleakala and La Palma) is likely due to the absence of a surface layer at the lake. The lower row shows the median values of r_0 as a function of calendar month (lower left) and hour angle (lower right).

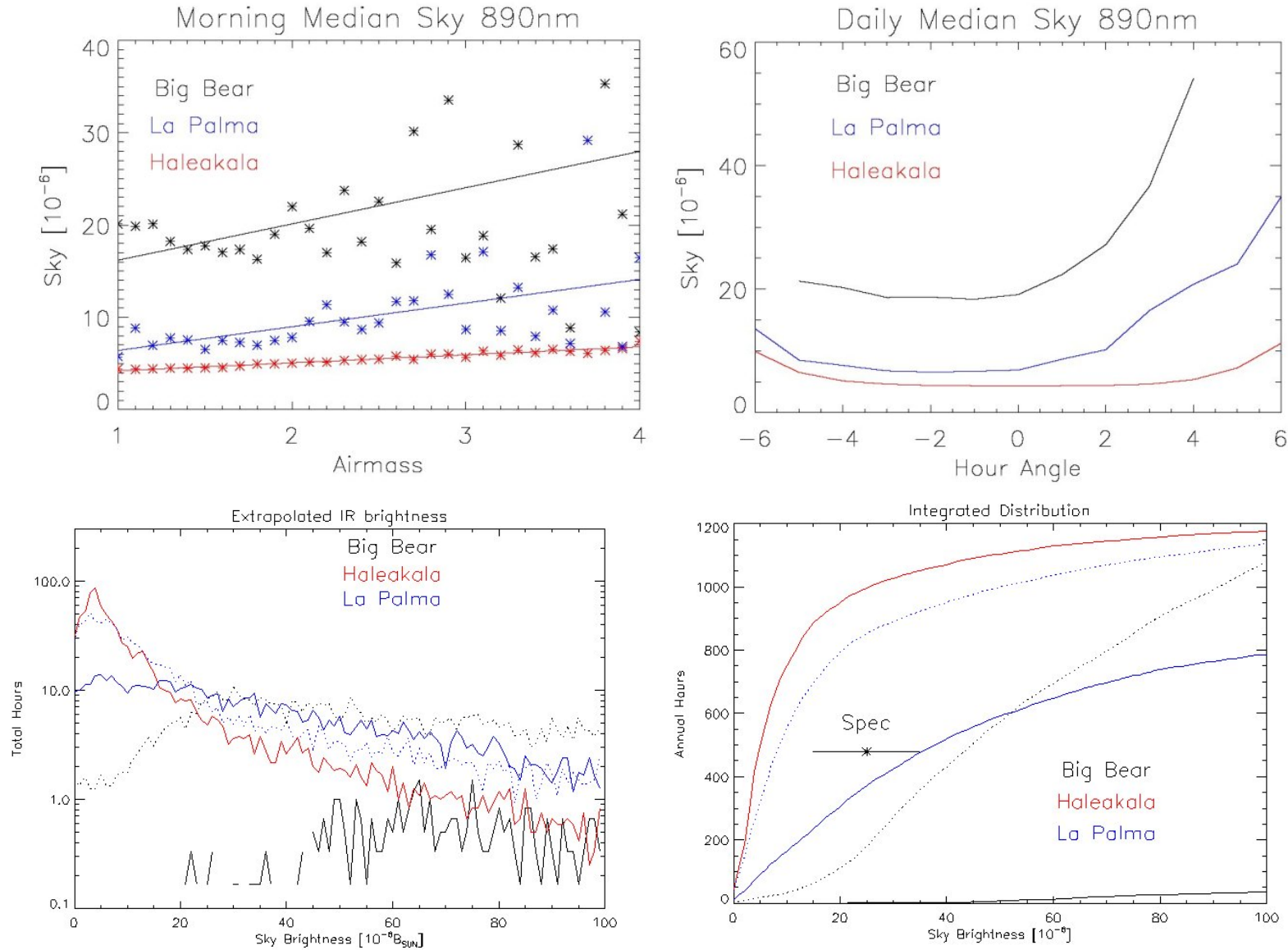


Figure ES.3: These plots show some of the Sky brightness results. Upper left: The median sky brightness at 890 nm as a function of morning air mass. Upper right: The median 890-nm sky as a function of hour angle. Lower left: a histogram of the sky brightness extrapolated to 1000 nm and 1.1 radii. Lower right: The cumulative histogram of the extrapolated sky brightness. See Figure 10.21 for further details.

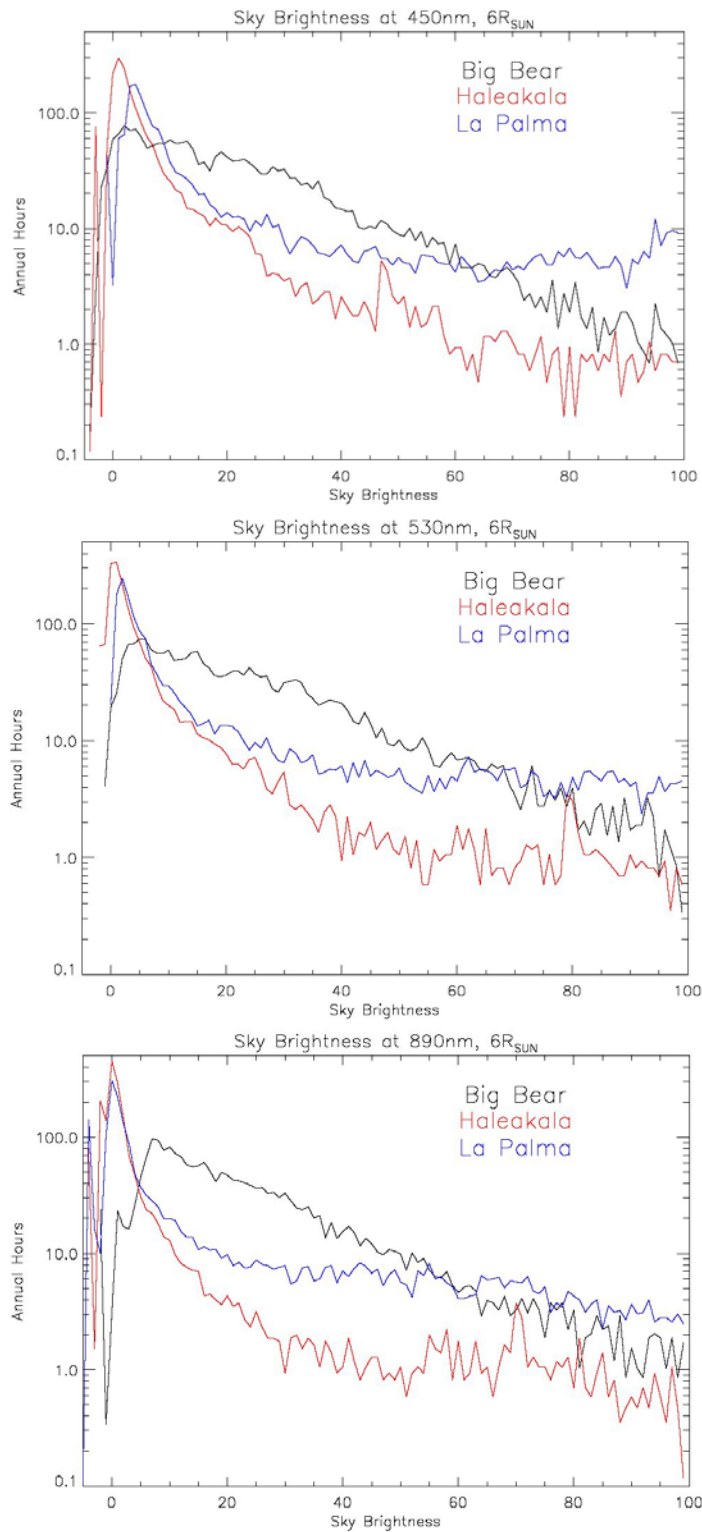


Figure ES.4 – These plots show histograms of the sky brightness measurements for the three sites.

Seeing	Big Bear	Haleakala	La Palma
Time Period Start	18-Jul-2002	6-Aug-2002	28-Sep-2002
Time Period End	30-Aug-2004	30-Aug-2004	30-Aug-2004
N days observed	774	755	702
N valid seeing measurements	820434	713678	718370
Smoothed S-DIMM r0 Median (5-min running mean)	6.04	3.53	3.42
S-DIMM Corrected Annual hours r0 >7 cm	856	389	313
S-DIMM Corrected Annual hours r0 > 12 cm	64	96	53
S-DIMM Corrected Annual N 2-hr blocks r0 > 7 cm	62	15	14
S-DIMM Corrected Annual N 2-hr blocks r0 > 12 cm	1	2	0
Results from IAC analysis -- CASE 2 Clear time fraction			
S-DIMM/SHABAR r0 18 m Median, cm	6.33	4.42	4.15
S-DIMM/SHABAR r0 28 m Median, cm	6.42	4.99	4.73
S-DIMM/SHABAR r0 38 m Median, cm	6.49	5.48	5.25
S-DIMM/SHABAR 8 m Corrected Annual hours r0 >7 cm	863	386	311
S-DIMM/SHABAR 18 m Corrected Annual hours r0 >7 cm	1017	768	632
S-DIMM/SHABAR 28 m Corrected Annual hours r0 >7 cm	1053	997	887
S-DIMM/SHABAR 38 m Corrected Annual hours r0 >7 cm	1081	1157	1093
S-DIMM/SHABAR 8 m Corrected Annual hours r0 > 12 cm	65	96	54
S-DIMM/SHABAR 18 m Corrected Annual hours r0 > 12 cm	120	267	136
S-DIMM/SHABAR 28 m Corrected Annual hours r0 > 12 cm	136	399	225
S-DIMM/SHABAR 38 m Corrected Annual hours r0 > 12 cm	147	511	324
S-DIMM/SHABAR 8 m Corrected Annual N 2-hr blocks r0 > 7 cm	49	15	17
S-DIMM/SHABAR 18 m Corrected Annual N 2-hr blocks r0 > 7 cm	71	47	43
S-DIMM/SHABAR 28 m Corrected Annual N 2-hr blocks r0 > 7 cm	83	82	60
S-DIMM/SHABAR 38 m Corrected Annual N 2-hr blocks r0 > 7 cm	84	106	80
S-DIMM/SHABAR 8 m Corrected Annual N 2-hr blocks r0 > 12 cm	0	2	0
S-DIMM/SHABAR 18 m Corrected Annual N 2-hr blocks r0 > 12 cm	1	3	2
S-DIMM/SHABAR 28 m Corrected Annual N 2-hr blocks r0 > 12 cm	1	10	4
S-DIMM/SHABAR 38 m Corrected Annual N 2-hr blocks r0 > 12 cm	1	18	4

Summary Table 1: Seeing results from the S-DIMM and for one of the inversion methods at heights of 8, 18, 28, and 38 m above the ground.

Weather			
Clear Time fraction Case 1: Flags are clouds	0.465	0.574	0.475
Corrected annual clear hours Case 1	1684	2725	2403
Clear Time fraction Case 2: Flags are down	0.712	0.619	0.639
Corrected annual clear hours Case 2	2579	2931	3197
Clear Time fraction GONG (Teide for La Palma)	0.714	0.647	0.708
Wind Speed median m/s	4.7	4.5	3.6
Sky Brightness			
Time Period Start	25-Feb-03	3-Jan-03	23-Apr-03
Time Period End	31-Aug-04	31-Aug-04	31-Aug-04
N days observed	216	189	186
N valid measurements	51036	62188	80432
Sky brightness median, 1.e-6 extrap to 1.1 r, 1 micron	96 to 800	5.8	31 to 114
Sky brightness median, 1.e-6 at 6 r and 890 nm	20	1.1	5.4
Sky brightness median, 1.e-6 at 6 r and 530 nm	21	2.4	11
Sky brightness median, 1.e-6 at 6 r and 450 nm	19	3.1	14
Radial exponent median at 890 nm	2.20	1.03	1.92
Wavelength exponent median at 4 r	0.32	0.53	0.51
Water vapor absorption median at 950 nm	0.12	0.10	0.09
Corrected annual hours satisfying sky brt req	2 to 198	1004.0	384 to 861
Corretced Annual N 4-hour blocks satisfying sky brt req	0 to 4	212	62 to 107
0.3 Dust Median	721197	27909	654435
0.5 Dust Median	36783	5229	10845
1.0 Dust Median	7938	927	5355
2.0 Dust Median	1728	216	450
5.0 Dust Median	234	45	81
N measurements	10292 to 10340	1217 to 2343	2654 to 3073

Summary Table 2: Weather and sky brightness quantities.

2. GOALS

The Advanced Technology Solar Telescope (ATST) Site Survey Working Group (SSWG) was formed to test probable sites for the ATST. This goal is summarized in the charge to the SSWG:

SSWG charge:

The main objective of the ATST site survey is to ensure that the ATST is located at the best feasible site. The task of the Site Survey Working Group (SSWG) is to advise the ATST project scientist on how to perform the ATST site test campaign. The goal of the site survey is to ensure that the ATST is located at a site that allows the ATST to meet its science requirements. The SSWG is composed of solar physics community members with a range of expertise that includes site testing and solar observing. The SSWG reports to the Project Scientist on a regular basis.

The SSWG will:

- Develop, review and evolve a site-testing plan
- Specify site requirements based on science requirements stated in the ATST proposal
- Consult with the Project Scientist and ASWG on site requirement specification
- Recommend the initial sites to be tested
- Recommend site test procedures and equipment
- Review the data reduction methods
- Periodically monitor the results
- Prepare a report on the site survey results

This report fulfills the obligation of the last item in the charge. It contains descriptions of the instrumentation; discussions of the data analysis including the limitations of the methods, and presents the results to date.

In addition to selecting the ATST site, there were two goals:

- Provide ATST engineering input
- Study daytime seeing

The ATST engineering effort requires information about the meteorological conditions at the site. These are provided by the weather station component of the site survey instrumentation. In addition, the engineering studies are modeling the performance of the telescope which requires actual observed statistical distributions of the site characteristics.

The final goal of the survey was perhaps the most interesting to the SSWG. The SSWG is aware of only two useful earlier comparative studies of daytime seeing at multiple sites with consistent instrumentation and methods. The CalTech survey that selected Big Bear examined some 38 sites in southern California (Zirin and Mosher 1985) using visual observations and trained observers. The JOSO site survey that selected two sites on the Canary Islands (Brandt & Wöhl 1982) studied nearly 40 sites in southern Europe with a variety of atmospheric sounding methods. With the ATST site survey, the details of the height and temporal variations of C_n^2 have been recorded over a wide range of meteorological and geographical conditions. This information might eventually lead to a method of identifying new potential solar observing sites.

3. SCIENTIFIC REQUIREMENT GOALS

This section duplicates ATST Project Document Specification #0006 Revision #A

3.1 SEEING

The highest ATST scientific priority is high-resolution studies of solar fine structure, such as magnetic field generation, evolution, and flux-tubes. This, in turn requires high spatial resolution; the ATST 4-m aperture has a diffraction limit of 0.03 arcsec at a wavelength of 500 nm. This can only be achieved if r_0 is 4m, which will never occur. Thus, adaptive optics is required, and the limitations of these systems must be considered in deriving the site requirements. In addition, the key scientific requirement is the S/N ratio of the intensity measured by the ATST, since $I(\lambda, x, y, t)$ is the fundamental measurement from which all other physical parameters are derived.

The Strehl ratio is a key determinant of the S/N ratio. Experience with A/O suggests a minimum Strehl of 0.2-0.3 is needed (see ATST Science Requirements Document (SRD)). Examining Fig. 3.1 shows that a Strehl of 0.2 can be reached with a 400-element A/O system at an r_0 of 7 cm. However, since r_0 typically varies over a wide range during the day, it is better to have more elements to reduce the Strehl ratio variation. A/O systems with 1000 elements are available now; such a system would provide a Strehl greater than 0.4 at an r_0 of 7 cm. A 7-cm r_0 is also the minimum aperture at which granulation can be resolved in the visible, which sets the fundamental lower limit of the A/O wavefront sensor subaperture size. In addition, the number of elements required to correct over an aperture D at a given r_0 is $(D/r_0)^2$, so for 1000 elements. I.e., the cost, complexity and performance of the AO system are strong functions of r_0 . For a 4-m aperture and an AO system with 1000 elements (largest system operational to date; Starfire), r_0 must be at least 12.7 cm in order to achieve the high Strehl A/O performance called for in the SRD.

Putting all this together suggests that r_0 must be greater than 7 cm for substantial periods of time, and preferably should be at least 12-13 cm as much as possible, assuming an A/O system with on the order of 1000 elements.

AO corrected FOV: For flux tube studies, a FOV of 10 arcsec should be sufficient, but for active regions an FOV of 2-5 arcmin is needed, requiring MCAO. A site with large isoplanatic patch is therefore highly desirable. In addition to r_0 , the isoplanatic patch, θ , plays an important role in determining the performance of an A/O system. The wavefront sensor noise decreases as the FOV of the correlating Shack-Hartmann sensor increases. A typical minimum FOV for effectively tracking granulation is 8-10 arcsec. However, the field of view of the A/O subapertures that is used to determine the wavefront errors should not be larger than the isoplanatic patch. If the wavefront sensor FOV contains several isoplanatic patches only turbulence close to the telescope aperture is corrected. The site requirement is: large isoplanatic angle ($\theta > 10$ arcsec is desirable) for substantial periods of time.

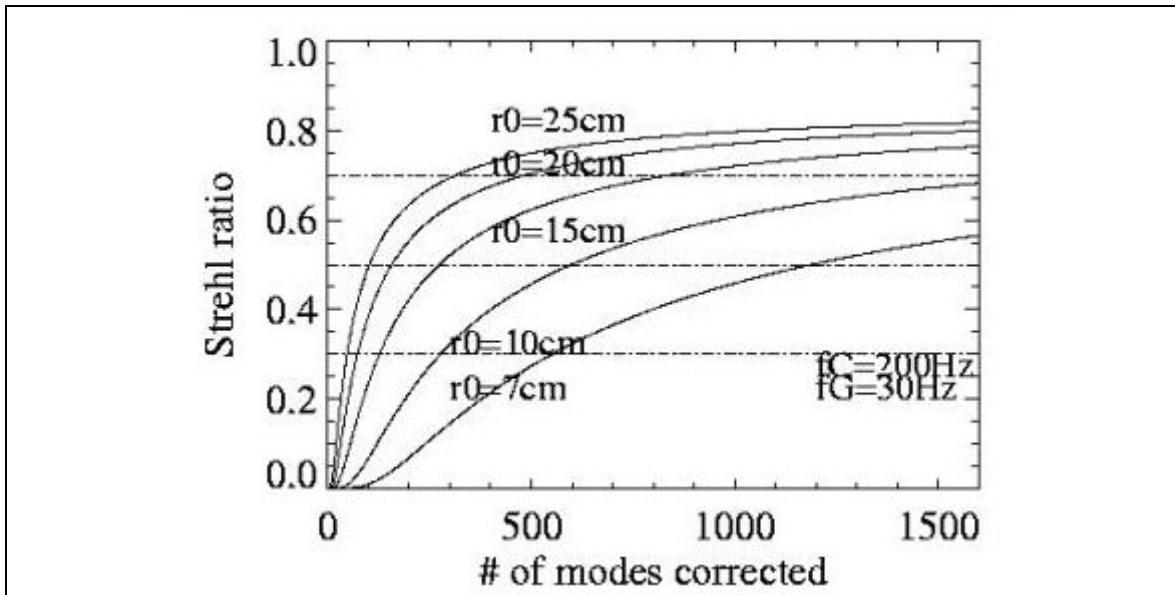


Figure 3.1: Plot of achievable Strehl ratio as a function of number of modes or elements in an A/O system for selected values of r_0 . Plot courtesy of T. Rimmele.

To provide a requirement on the temporal distribution of r_0 , flux tube studies can be done with 1-hour time series, but active region evolution occurs over many hours. A reasonable compromise might be 4 hours for $r_0 > 7$ cm, 2 hours for $r_0 > 12$ cm. The other major input for the temporal distribution is the overall fraction of clear time. In order to ensure sufficient productivity, the clear time fraction during the day should be at least 70% (i.e. 3000 annual sunshine hours). Given the ATST science priorities, 60% of the clear time (i.e. 1800 hours annually) would be a reasonable allocation for high-resolution work, with the remaining 40% split equally between coronal and IR studies.

Since there may be no tested site that fulfills all requirements, the desired site characteristics are described as goals. In practice, sites coming close to these goals will be highly ranked.

Summarizing, the draft ATST site requirement goals for high-resolution conditions are:

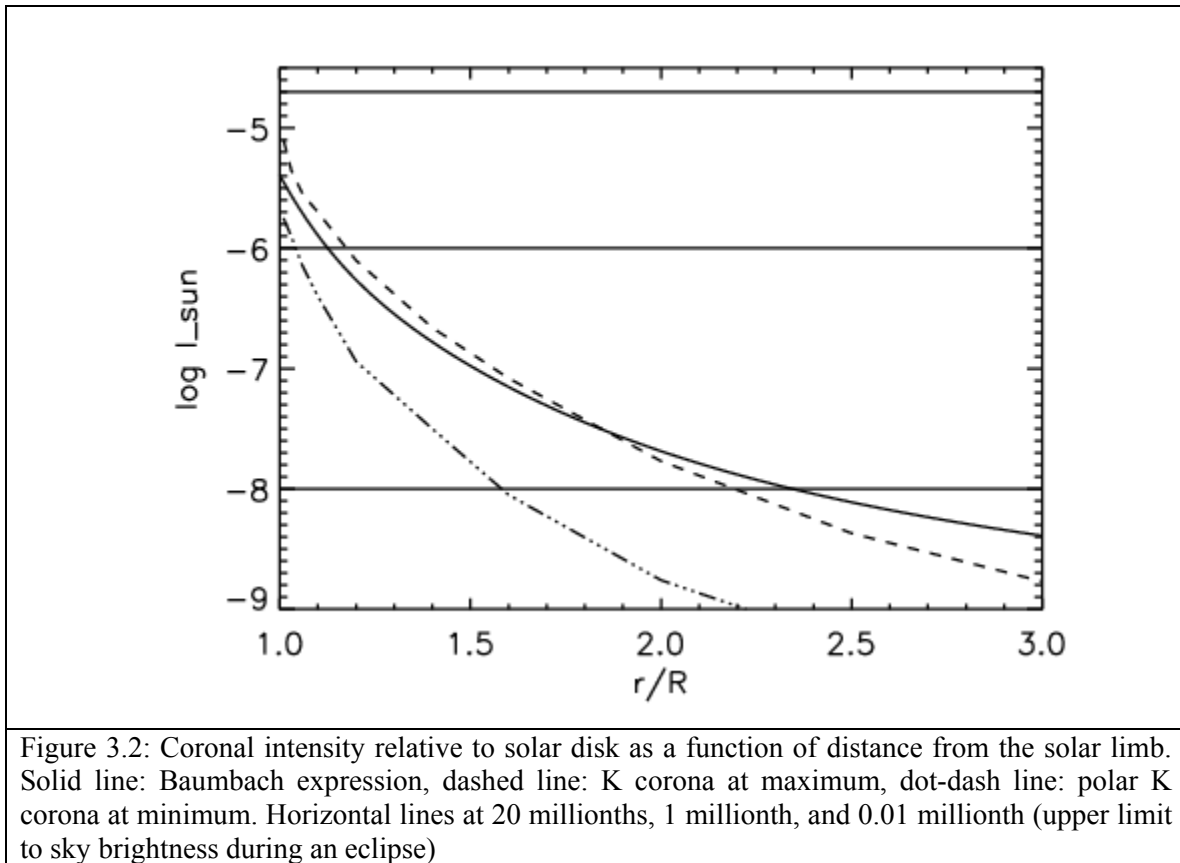
- Clear daytime fraction of 70%, 3000 hours annual sunshine.
- 1800 annual hours with r_0 (500 nm) > 7 cm (measured at the telescope aperture), including at least 100 continuous 2-hr periods.
- 200 annual hours with r_0 (500 nm) > 12 cm (measured at the telescope aperture) including at least 10 continuous 4-hr periods.
- Large isoplanatic angle, i.e., good atmospheric conditions at high altitudes.

3.2 SKY BRIGHTNESS AND IR

The second-level science priority for the ATST is coronagraphy and IR studies. During the remaining 40% of the clear time (i.e. 1200 annual hours), the site should supply conditions that allow this science to be performed. The corona has a very low intensity compared to the solar disk and the coronal intensity falls off very rapidly with distance from the solar limb, as shown by the classical Baumbach expression:

$$I_c = I_{\text{disk}} * 10^{-6} * (0.0523 \rho^{-2.5} + 1.425 \rho^{-7} + 2.565 \rho^{-17})$$

where I_c is the coronal intensity, I_{disk} is the intensity of the solar disk, and ρ is the distance from the limb in units of solar radii. Figure 3.2 shows a plot of this function, along with two examples of the K corona intensity profile.



According to Golub & Pasachoff, the best coronal sites often have a sky brightness less than 20 millionths of the solar disk center, and sometimes as low as 1 millionth. These levels are indicated in figure 3.2, along with the upper limit to the sky brightness during a total eclipse. It is obvious that even the best coronal site cannot compete with an eclipse for sky brightness. However, the brightest coronal emission lines can exceed 100 millionths at line center. It is thus desirable for the ATST site to provide useful coronal spectroscopic conditions. A draft requirement is that 16% of the clear time provides a sky brightness less than or equal to 25 ± 10 millionths at a distance of 1.1 radii from the limb at 1 micron, with a radial slope equal to or steeper than $R^{-0.8}$.

The impact of water vapor on infrared solar observations is somewhat controversial. For broad-band photometry, the precipitable water vapor (PWV) content can strongly influence the observations, particularly during the night. On the other hand, spectroscopic solar observations may not be severely affected particularly if the solar lines are unblended with water vapor. In addition, techniques for correcting water/solar blends have been developed. To minimize any adverse effects on IR observations with the ATST, it is prudent to set a site requirement that 20% of the clear time occur with a PWV less than 5 mm over several hours. This needs to be translated into a requirement on the strength of the water vapor bands around 9400 Å.

Summarizing, the draft ATST site requirement goals for sky brightness and water vapor are:

- 480 annual hours with a sky brightness less than or equal to 25 +/- 10 millionths at 1.1 radii at 1 micron with a radial profile equal to or steeper than $R^{-0.8}$, including at least 40 continuous 4 hour periods.
- 600 annual hours with the precipitable water vapor below 5 mm, including at least 40 continuous 4-hour periods.

4. BRIEF HISTORY OF THE SSWG

The SSWG was initially formed at the 2000 SPD meeting at South Lake Tahoe. During the course of a community meeting on the ATST, a call for SSWG volunteers was made. A number of community members agreed to serve on this group. The membership has gone through some changes during its existence for various reasons. The following list shows the current and past members of the group.

Current Members:

- Jacques Beckers, U. Chicago
- Timothy Brown, High Altitude Observatory (Chair)
- Manuel Collados, Instituto de Astrofisica de Canarias
- Carsten Denker, New Jersey Institute of Technology
- Frank Hill, National Solar Observatory
- Jeff Kuhn, U. Hawaii - Institute of Astronomy
- Matt Penn, National Solar Observatory
- Hector Socas-Navarro, High Altitude Observatory
- Dirk Soltau, Kiepenheuer-Institut fuer Sonnenphysik
- Kim Streander, High Altitude Observatory

Past Members:

- K.S. Balasubramaniam, National Solar Observatory
- Peter Brandt, Kiepenheuer-Institut fuer Sonnenphysik
- Mark Giampapa, National Solar Observatory
- Harrison Jones, NASA/Goddard
- Haosheng Lin, U. Hawaii - Institute of Astronomy
- Sara Martin, Helio Research Corp.
- Matthew Penn, National Solar Observatory
- Richard Radick, Air Force Cambridge Research Labs
- Richard Shine, Lockheed-Martin Solar & Astrophysics Lab

The SSWG has had a number of telecons. In 2001, there were a total of eight telecons during which the list of 72 candidate sites was discussed along with the process to reduce it to the small number of sites that were testable within the resource constraints of the survey. That task was accomplished in October 2001. There then ensued a long interval until the next telecon in December 2002. During the hiatus, the seeing instruments were being built and tested and there was a reduced need for SSWG interaction. Once the instruments were deployed and the data began to be collected, the telecons became more frequent. Six were held in 2003 and 16 in 2004 as of the time of this report.

5. PRELIMINARY SELECTION PROCESS

The site selection process began with the making of a list of potential sites with the only constraint being that the candidates had to be reasonably sunny. The list was inserted into a spread sheet, along with some basic geographic and climate data. The spread sheet is shown in Table 1. There are 72 sites in the list, but only six could be tested given the resources of the survey. The problem was how to cull the list down from 72 to 6 sites.

Site Name	ID	Elevation (ft)	Lake area (Acres)	Shortest Distance to Ocean (miles)	Annual Sunshine hours	Number of ocean sides (<100 miles away)	score
Normalization		5,000	1000	25	3000	4	
Power		1.0	0.5	1.0	2.0	1.0	
Abiquiu Lake, NM	20	6309	6811.4	655	2800	0	0.18
Bear Lake, UT	52	5922	82003.2	670	2400	0	0.41
Big Bear, CA	30	6781	2725.8	70	2800	0	1.39
Caballo Reservoir, NM	1	4190	8115.2	535	3000	0	0.22
Castaic Lake, CA	40	1561	3705.6	30	2400	1	2.61
Cerro Tololo, Chile	46	7267	0.0	37	3100	1	1.87
Cone Peak, Monterey, CA	60	4920	0.0	3	1200	1	11.62
El Vado Lake, NM	8	6919	3206.9	650	2800	0	0.16
Elephant Butte, NM	4	4360	27027.2	525	3000	0	0.34
Great Salt Lake, UT - Carrington Island	69	4708	1280000.0	575	3000	0	1.64
Guillermo Haro Obs, MX	55	8136	0.0	285	3200	0	0.24
Haleakala, HI	43	10020	0.0	7	2800	4	13.84
Heron Lake, NM	37	7165	4761.6	650	2800	0	0.17
Isabella Lake, CA - Rocky Point Peninsula	16	2856	7539.2	110	2400	0	0.90
Jelm Mountain, WY	53	9593	0.0	900	2200	0	0.07
Jungfrau, SW	25	11729	0.0	460	1700	0	0.14
Junipero Serra Peak, CA	71	5837	0.0	11	1600	2	4.44
Kitt Peak, AZ	36	6955	0.0	275	2600	0	0.19
La Crescenta, CA	48	2060	0.0	21	3000	2	2.28
La Palma, Canaries	3	7631	0.0	5	2600	4	16.39
Laguna Verde, BO	62	13970	5600.0	215	3000	0	0.72
Lahontan Reservoir, NV	19	4167	6575.8	215	3200	0	0.53
Lake Arrowhead, CA	50	5121	742.4	60	2800	0	1.15
Lake Cachuma, CA	63	758	3129.6	9	2400	2	8.50
Lake Casitas, CA - Island	68	835	2075.0	6	2600	2	11.91
Lake Elsinore, CA	21	1247	4243.2	23	2800	2	4.00
Lake Havasu, AZ	31	456	11148.8	195	3600	0	0.62
Lake Henshaw, CA - Monkey Hill Island	51	2803	5420.8	35	2800	1	2.86
Lake Mathews, CA	22	1398	2499.1	29	2800	2	2.79
Lake Mead, AZ	57	1220	148448.0	260	3200	0	1.30
Lake Mohave, AZ	47	650	4780.8	215	3600	0	0.44
Lake Pleasant, AZ	61	1561	2176.0	290	3200	0	0.25
Lake Powell, AZ	28	3707	66412.8	435	2800	0	0.56
Lake Tahoe, CA	10	6240	117856.0	160	2400	0	1.99
Lake Titicaca, Peru/Bolivia	32	12506	2240000.0	178	2500	0	7.10
Lowell Obs, AZ	12	7222	0.0	360	2400	0	0.14
Lyman Lake, AZ	45	5984	1295.4	455	2800	0	0.18
Manashtash Ridge, WA	64	3187	0.0	175	2000	0	0.15
Mauna Kea, HI	17	13828	0.0	17	2800	4	6.82
Mauna Loa, HI	33	11000	0.0	24	2800	4	4.24
Mono Lake, CA - Paoha Island	70	6595	41184.0	172	2400	0	1.22
Mount Locke, TX	24	6766	0.0	460	2800	0	0.12
Mt. Graham, AZ	56	10683	0.0	380	2400	0	0.18
Mt. Hamilton, CA	26	4188	0.0	30	2000	1	1.28
Mt. Hopkins, AZ	2	8349	0.0	290	2400	0	0.20
Mt. Laguna, CA	42	6285	0.0	46	2800	1	1.29
Mt. Lemmon, AZ	35	9025	0.0	325	2400	0	0.19
Mt. Wilson, CA	38	5715	0.0	29	3000	1	2.06
Nacimiento Reservoir, CA	9	807	5740.8	16	2000	2	5.47
Navajo Lake, NM	58	6093	10112.0	605	2800	0	0.22
Panguitch Lake, UT	65	8222	1139.2	410	3200	0	0.23
Paranal, Chile	14	8908	0.0	7	3800	1	12.99
Pathfinder Reservoir, WY	67	5860	21145.6	875	2200	0	0.18
Perris Reservoir, CA - Island	27	1769	2393.6	41	2800	2	2.00
Pic Du Midi, FR	5	9386	0.0	130	2500	0	0.49
Pine Flat Reservoir, CA	15	958	5600.0	130	2800	0	0.66
Pyramid Lake, NV - island	54	4139	109830.4	215	3200	0	1.45
San Antonio Reservoir, CA	39	787	5273.6	18	2000	2	4.72
San Carlos lake, AZ	29	2503	9670.4	370	2600	0	0.29
San Pedro Martir, MX	7	9284	0.0	37	2600	2	2.10
San Vicente Reservoir, CA - island	59	656	1203.2	20	2800	1	2.94
Santa Rosa Lake, NM	49	4726	11622.4	725	2800	0	0.18
Seminole Reservoir, WY	41	6371	16678.4	880	2200	0	0.17
Sierra La Laguna, Baja	72	7500	0.0	18	2500	3	4.09
Silverwood Lake, CA	11	3383	889.6	58	2800	1	1.18
Strawberry Reservoir, UT - Island	44	7657	13280.0	620	3000	0	0.25
Sunspot, NM	18	9223	0.0	570	2200	0	0.10
Teide, Canaries	23	7858	0.0	8	2600	4	10.38
Theodore Roosevelt Lake, AZ	66	2100	12450.5	350	3200	0	0.36
Utah Lake, UT	13	4488	84294.4	580	3000	0	0.48
Walker Lake, NV	34	3970	35532.8	210	3200	0	0.94
White Mountain, CA	6	11327	0.0	160	2000	0	0.42

An attempt was made to determine a “quality score” based on the elevation, lake area, distance to ocean, annual sunshine hours, and number of ocean sides (defined as the number of cardinal directions in which the ocean was less than 100 miles distant). Drawing from the collective experience of the SSWG, this formula was weighted to increase the score if the site was high in elevation, had a large lake, was close to the ocean, sunny, and had several ocean sides. The formula used was

$$S = \left(\frac{Elevation}{N_{el}} \right)^{P_{el}} + \left(\frac{LakeArea}{N_{la}} \right)^{P_{la}} + \left(\frac{Sunshine}{N_{sh}} \right)^{P_{sh}} + \left(\frac{OceanSides}{N_{os}} \right)^{P_{os}} \times \left(\frac{N_{od}}{OceanDist} \right)^{P_{od}}$$

where the quantities of the type N are the normalizations and the quantities P are the powers shown in Table 1, which also shows the scores computed in this way. The various values of N and P could be adjusted and the scores easily recomputed. A similar analysis was used to test common assumptions about the environmental influences on seeing.

Since this approach proved unable to reproduce the results obtained by the Big Bear site survey (Zirin & Mosher 1985), it was eventually discarded in favor of simple debate amongst the SSWG members. This debate quickly led to the conclusion that Big Bear, La Palma and Sac Peak should be tested since they are well-established productive solar observatories. It was also agreed that Hawaii should be tested, but there was vigorous discussion as to which one of the three established sites (Haleakala, Mauna Kea, Mauna Loa) would be a candidate. After looking at feasibility issues, the SSWG selected Haleakala as the Hawaiian candidate. This left two open slots to fill.

The process to fill the last two slots generated more discussions. It was felt that the set of candidates should have at least one additional lake site since there is ample evidence that lakes are very beneficial for solar observing. It was also felt that the inclusion of another non-US site could be advantageous in the search for international partners for the project. Further discussions pared the list for the two final sites down to:

- Abiquiu Lake, NM
- Lake Henshaw, CA
- Navajo Lake, NM
- Panguitch Lake, UT
- San Pedro Martir, Mexico
- Strawberry Reservoir, UT
- Lake Tahoe, NV/CA

After discussing the pros and cons of these sites and conducting a visit to Abiquiu Lake (which has a very low water level due to the prolonged drought in the southwest US), the SSWG took a vote and selected Panguitch and San Pedro Martir as the last two candidate sites.

6. DESCRIPTION OF THE SITES

6.1 BIG BEAR LAKE, CALIFORNIA

Location: 34° 14' 31" N 116° 58' 34" W

Elevation: 6717 feet (2067 m)

Lake Area: 82,000 acres

Distance to ocean: ~70 miles

Estimated sunshine: 2800 hrs/year

Big Bear Lake is the site of the Big Bear Solar Observatory operated by the New Jersey Institute of Technology. The lake is situated in the San Bernardino Mountains east of Los Angeles, and can be classified as a costal mountain lake. The observatory was constructed at the lake as the result of the extensive CalTech survey of sites in southern California (Zirin & Mosher 1985). Figures 6.1 and 6.2 show views of the observatory dome located at the end of a man-made causeway on the north side of the lake. The location of the site and the terrain around the lake are shown in Figure 6.3.



Figure 6.1: A view of the dome at Big Bear Solar Observatory



Figure 6.2: The Big Bear dome viewed from the lake

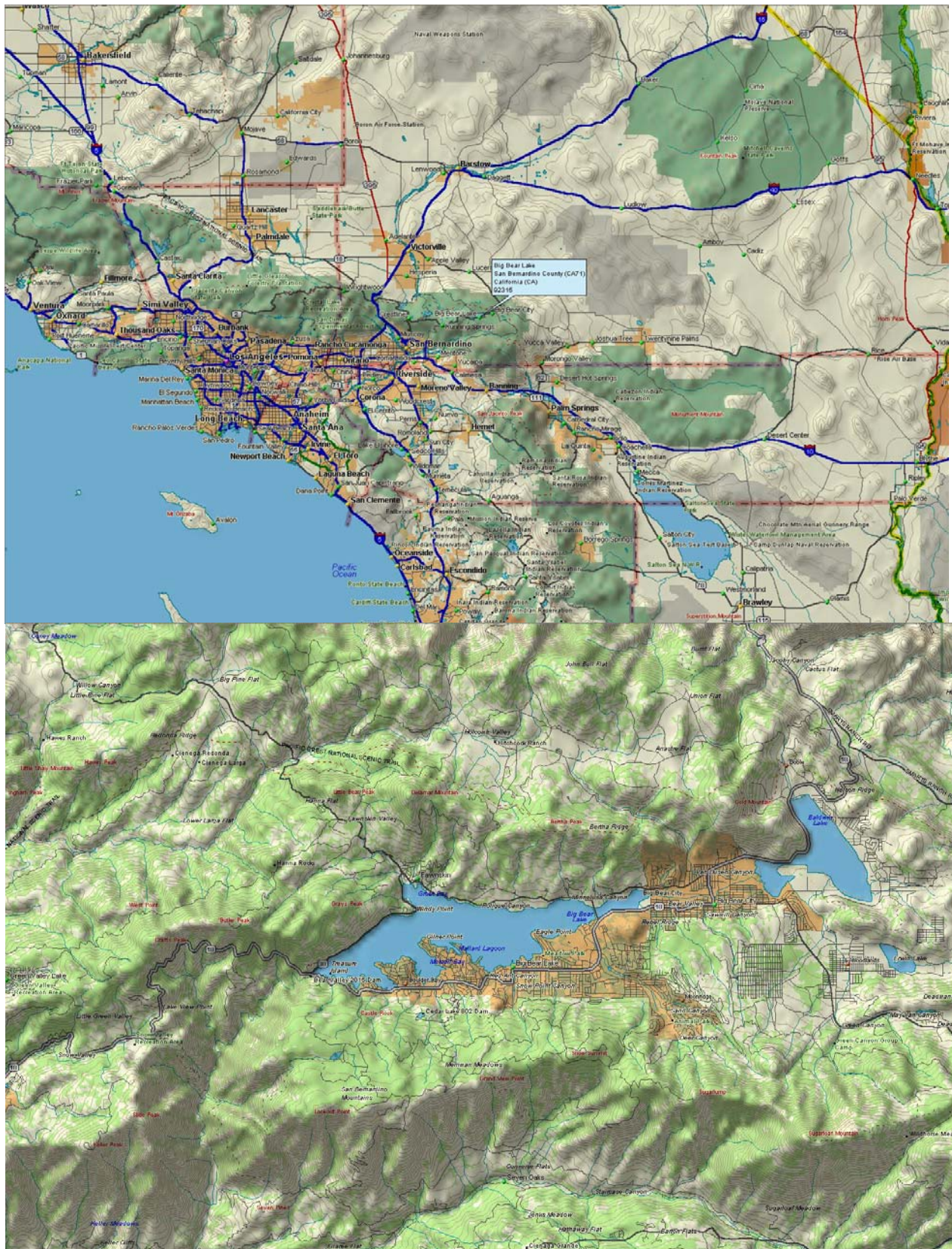


Figure 6.3: The location and terrain of Big Bear Lake. North is up.

6.2 HALEAKALA, HAWAII

Location: 20° 42' 17" N, 156° 10' 36" W

Elevation: 10,023 feet (3084 m)

Lake Area: None

Distance to ocean: 7 miles

Estimated sunshine: 2800 hrs/year

Haleakala is the site of the Mees Solar Observatory, operated by the Institute for Astronomy of the University of Hawaii. Haleakala is the mountain that mainly forms the island of Maui in the Pacific Ocean, and is classified as a Pacific Ocean island mountain. Figure 6.4 shows a general view of the top of the mountain. Figure 6.5 shows location and terrain maps



Photograph by Ray Mains

Figure 6.4 – An aerial view of the top of Haleakala

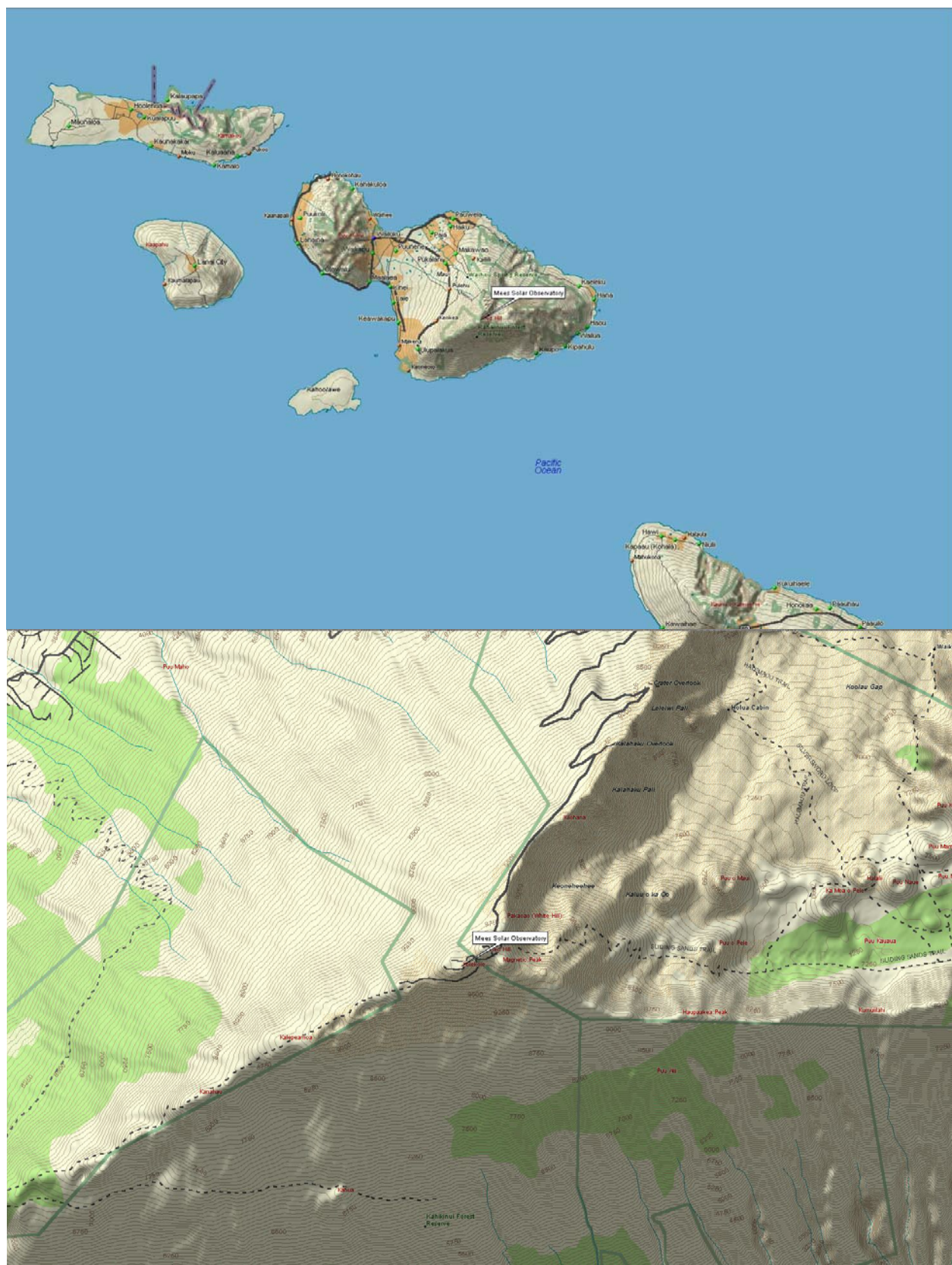


Figure 6.5: The location and terrain of Haleakala. North is up.

6.3 LA PALMA, CANARY ISLANDS, SPAIN

Location: 28° 45' 33" N, 17° 52' 33" W

Elevation: 7800 feet (2400 m)

Lake Area: None

Distance to ocean: 5 miles

Estimated sunshine: 2600 hrs/year

La Palma is the site of the Observatorio del Roque de los Muchachos, operated by the Instituto de Astrofísica de Canarias. La Palma is one of the Canary Islands, Spain in the Atlantic Ocean, and is classified as an Atlantic Ocean island mountain. Figure 6.6 shows an aerial view of the observatory. Figure 6.7 shows location and terrain maps

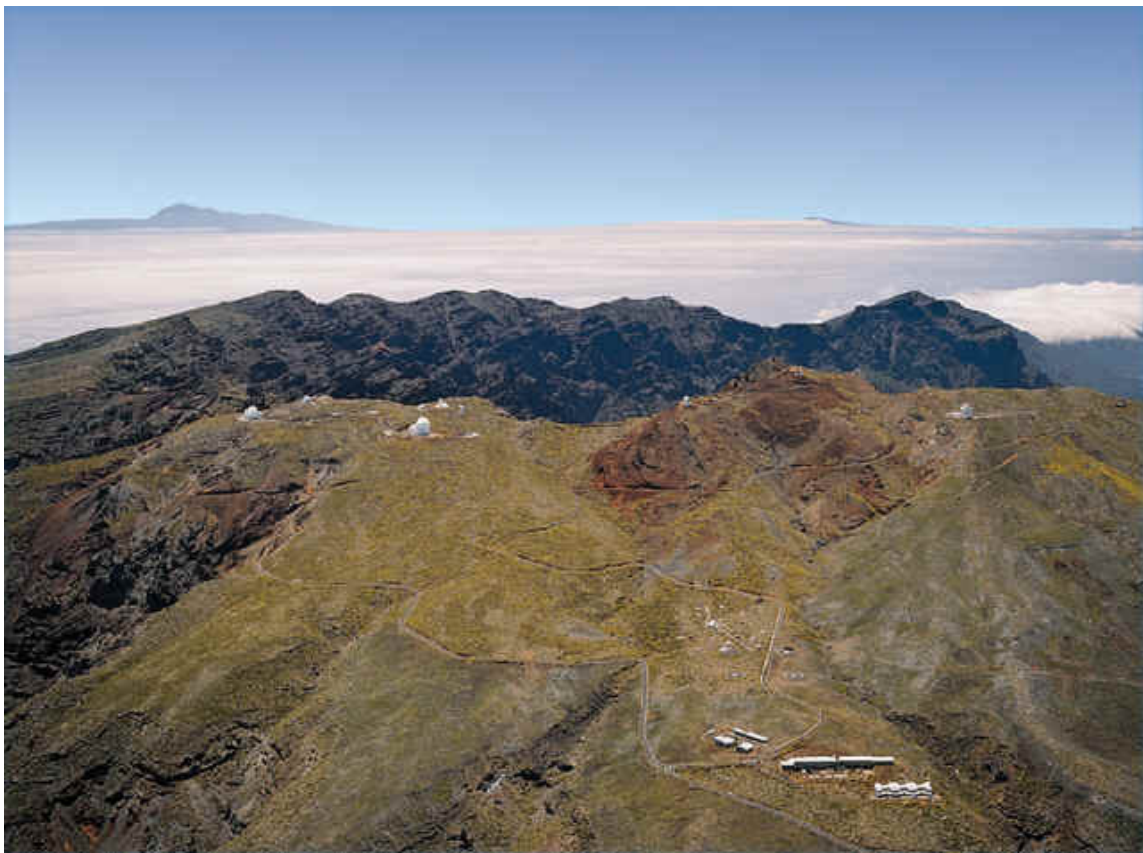


Figure 6.6 – An aerial view of the Observatorio del Roque de los Muchachos, La Palma, Canary Islands, Spain

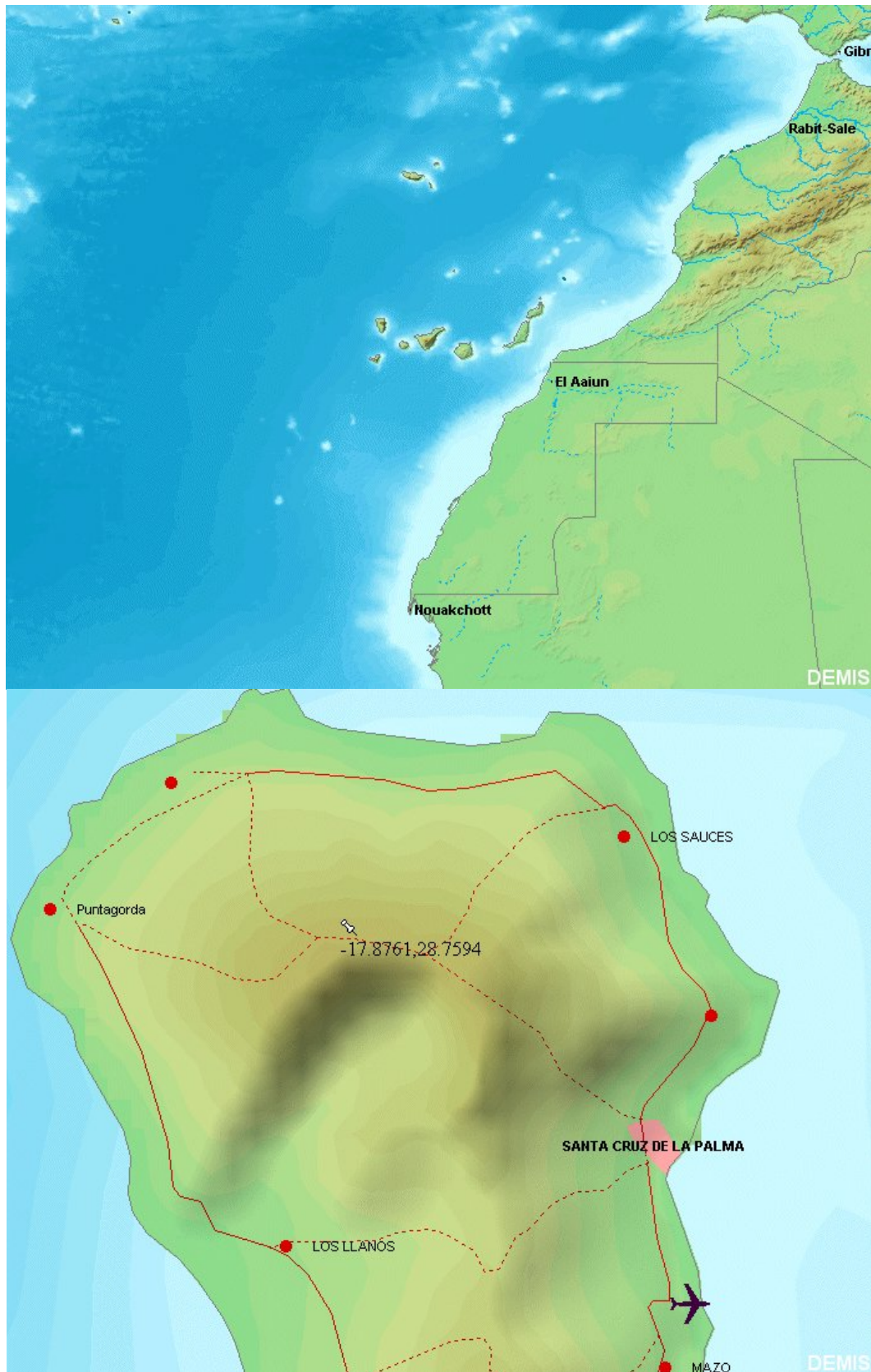


Figure 6.7 – location and terrain of La Palma

6.4 PANGUITCH LAKE, UTAH

Location: N 37 42.942', W 112 38.530'

Elevation: 8222 feet (2506 m)

Lake Area: 1139.2 Acres (4.6 sq km, 1.25 km NS, 3.25 km EW)

Distance to ocean: 410 miles to the west

Estimated sunshine: 3200 hrs/year

Panguitch Lake is in the Dixie National Forest. There is no observatory located at Panguitch Lake. There are a number of summer cabins and resorts, and a general store around the lake which is noted for its fishing. Panguitch can be classified as a continental mountain lake. Figure 6.8 shows a view of Panguitch in winter, and Figure 6.9 shows the location and terrain of the site.



Figure 6.8 -- A view of Panguitch Lake in the winter when the lake is frozen. The view is from the south shore, looking across the lake to the north shore where the site survey is being conducted.

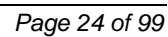


Figure 6.9 – Location and terrain of Panguitch Lake. The location being tested for the ATST is at the top of the vertical line across the lake in the terrain map. North is up.

6.5 SACRAMENTO PEAK, NEW MEXICO

Location: 32° 47' 16" N, 105° 49' 13" W

Elevation: 9255 feet (2847 m)

Lake Area: None

Distance to ocean: 570 miles to the west

Estimated sunshine: 2200 hrs/year

Sacramento Peak is the location of one of the two sites of the National Solar Observatory. The site is classified as a continental mountain. Figure 6.10 shows an aerial view of the observatory. Figure 6.11 shows location and terrain maps.



Figure 6.10 – An aerial view of Sacramento Peak Observatory, NSO.

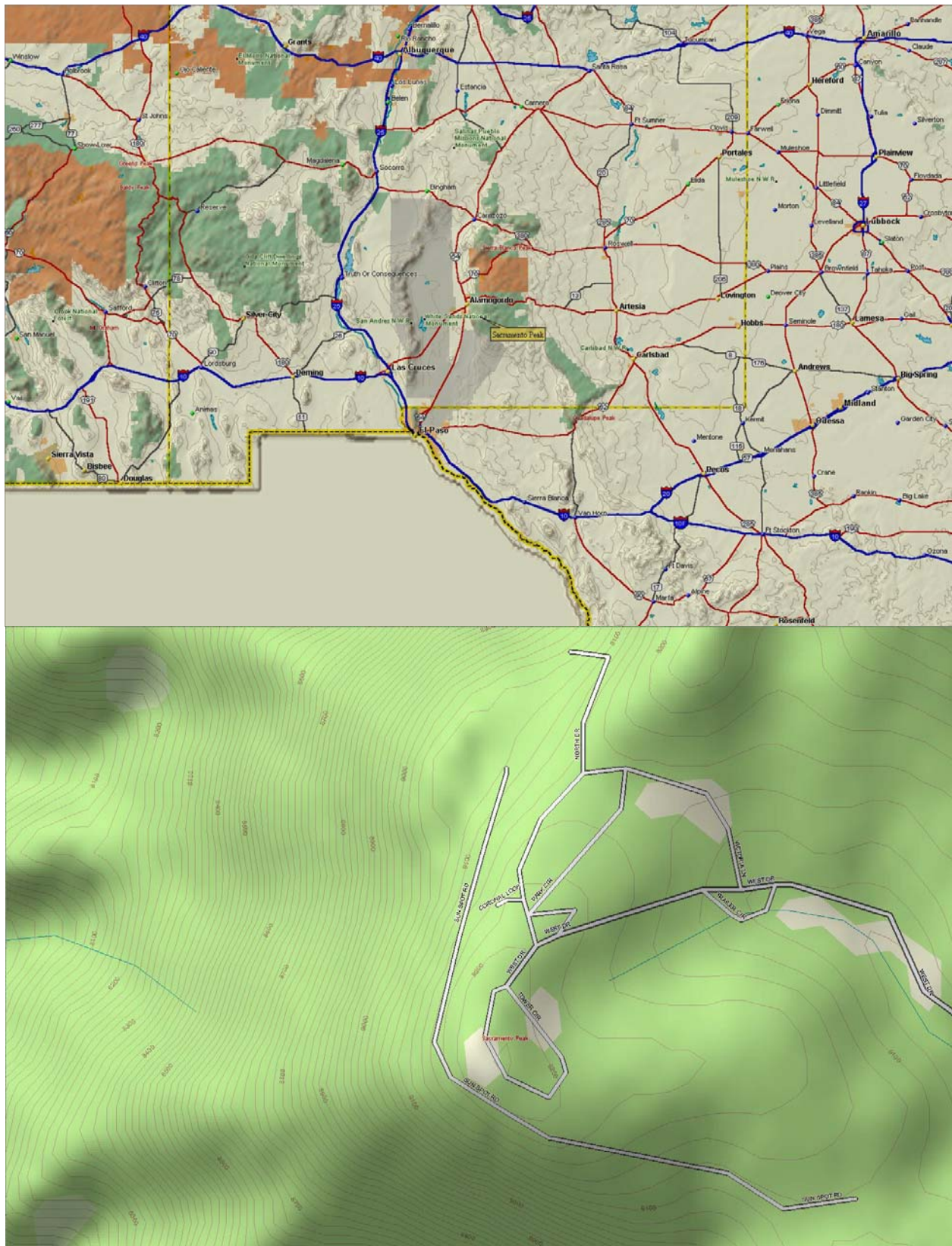


Figure 6.11 – Location and terrain for Sacramento Peak. North is up.

6.6 SAN PEDRO MARTIR, BAJA CALIFORNIA, MEXICO

Location: 31° 02.65' W 115 27.82'

Elevation: 9186 feet (2800 m)

Lake Area: None

Distance to ocean: 61 km to the west (Pacific Ocean), 61 km to the east (Gulf of California)

Estimated sunshine: 2600 hrs/year

San Pedro Martir is located in Baja California Norte, Mexico. It is the site of the Observatorio Astronomico Nacional, operated by the Universidad Nacional Autonoma de Mexico (UNAM). The site is classified as a peninsula. Figure 6.12 shows an aerial view of the observatory, and Figure 6.13 shows location and terrain for the site.



Figure 6.12 – An aerial view of the Observatorio Astronomico Nacional at San Pedro Martir, Mexico

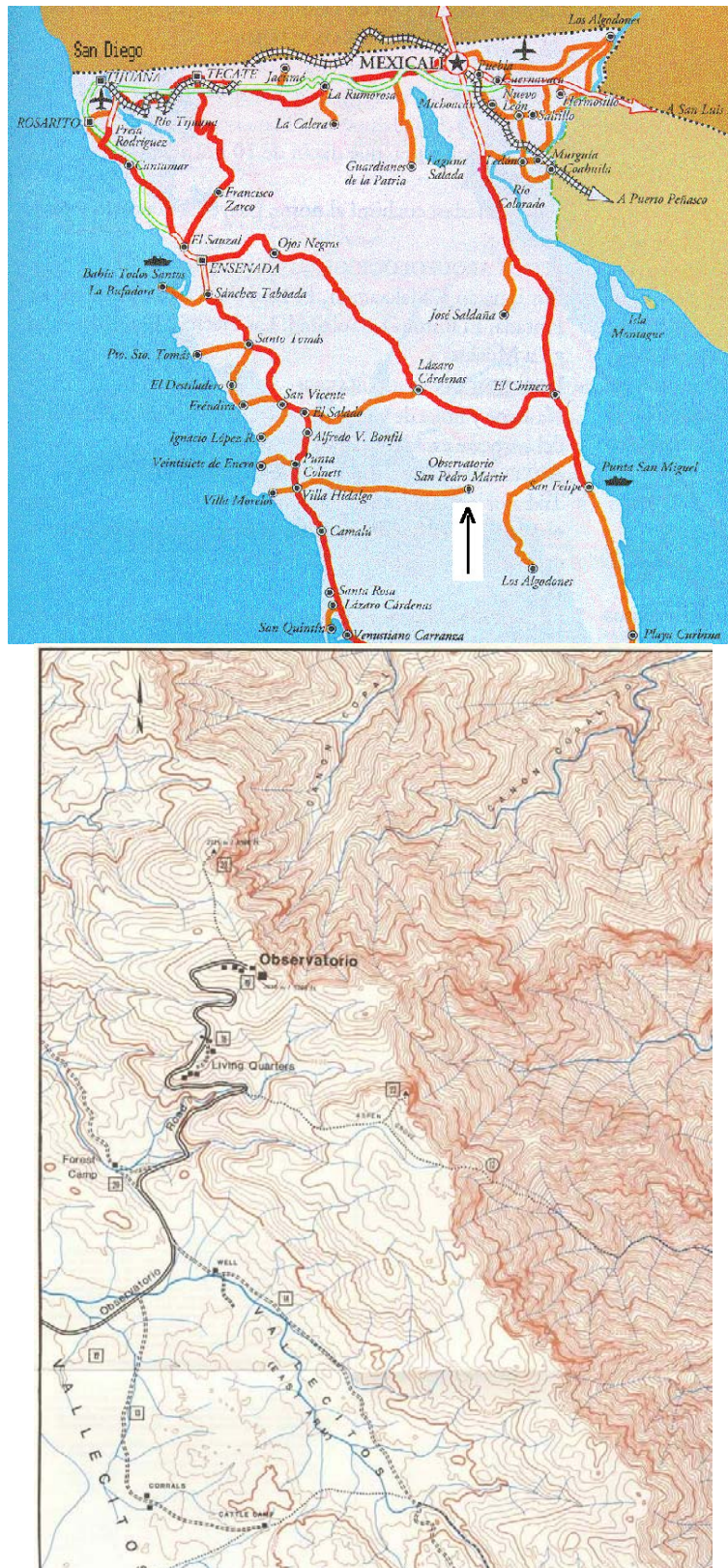


Figure 6.13 – Location and terrain of San Pedro Martir. North is up.

7. HISTORICAL DATA AND LONG TERM TRENDS

Since this survey has only covered a maximum of 2.1 years at any site, it is useful to consider historical data to get a feel for the validity of the short-term results reported here. A thorough analysis of existing data sets remains to be done. As an example of the information in the long-term data sets, Figure 7.1 shows about 15 years of sky brightness data from Haleakala and Sac Peak, obtained with the Evans Sky Photometers. The Sac Peak data shows a strong annual variation, which the ATST survey has not sampled adequately. The Haleakala data does not show a prominent annual variation, but does show the effect of the Mt. Pinatubo eruption with the sky brightness decreasing from 1991 to 1995. Labonte (2003) has published the long-term sky brightness variations. Any long-term trends in the parameters discussed in this report will not be apparent.

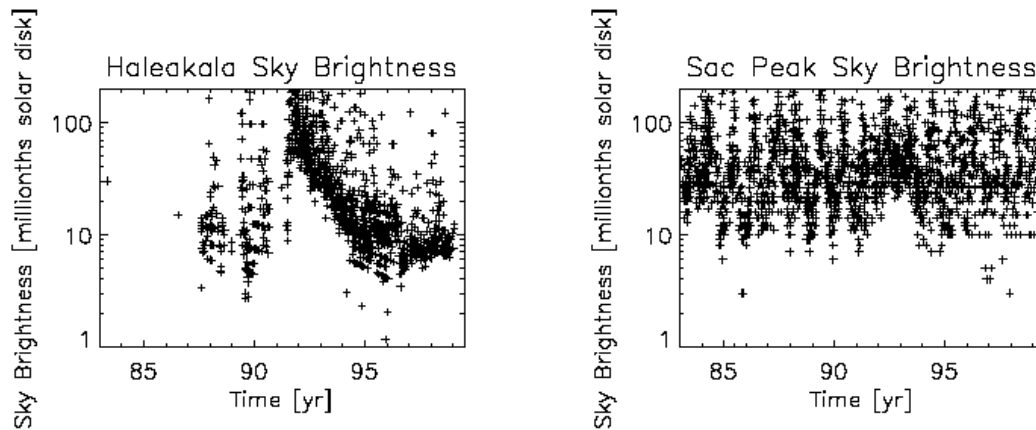


Figure 7.1 – Long-term sky brightness measurements at Haleakala and Sac Peak. The effects of the Mt. Pinatubo eruption are evident in the Haleakala data starting in 1991. From Kuhn et al. (2002)

Other long-term climate patterns of concern are the extended drought in the southwest US, and fluctuations in cloud cover and precipitation associated with El Niño. The current so-called mega drought in the US eliminated Abuquiu Lake from the list of potential sites due to the extremely low level of water in the lake at the start of the survey. Since most lakes in the southwest US are used as reservoirs, keeping the water level up for solar astronomy is not a high priority. Information about annual fluctuations in cloud cover can be found in the GONG site survey results (Hill et al. 1994)

In addition to historical trends in the past, some attempt should be made to anticipate long-term future changes. An example of this is shown in Figure 7.2 which shows two maps of jet aircraft contrails in 1992, and predicted in 2050. This figure shows a marked increase in the coverage of the world by contrails, particularly in the southwest US. The amount of particulates and pollution in the atmosphere cannot be substantially reduced with technology. On the other hand, there is a hope that the continued development of adaptive optics technology will improve the ability to correct for seeing. Thus, clear air may be the most precious resource for solar astronomy.

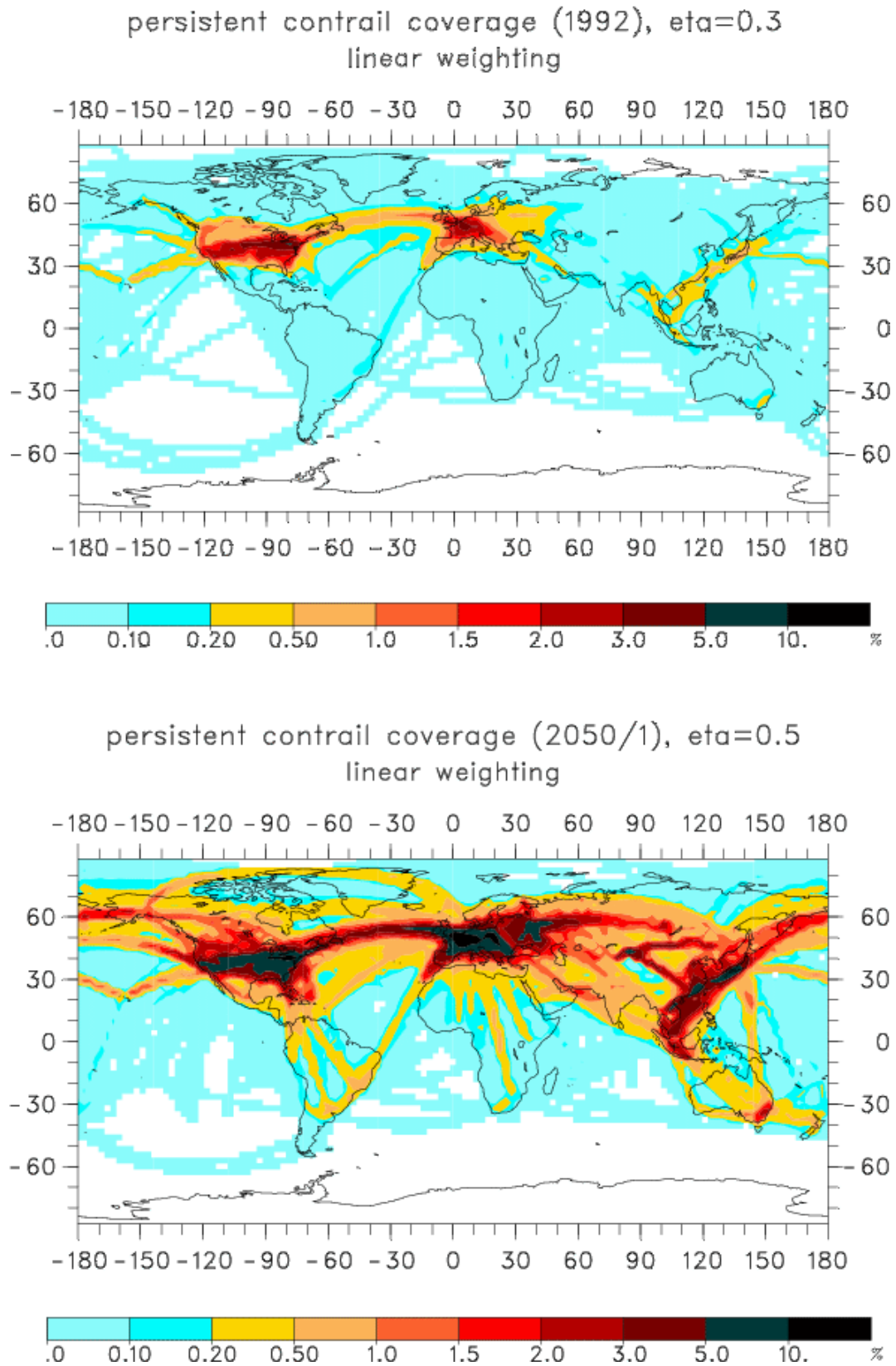


Figure 7.2 – World map of jet aircraft contrails in 1992 (top), and predicted for 2050 (bottom)

8. INSTRUMENTATION AND OPERATIONS

8.1 S-DIMM AND SHABAR

The Solar Differential Image Motion Monitor (S-DIMM) is based on the well-established night time DIMM with the exception that a slit image of the solar limb is used as the target instead of a stellar point source. The instrument was developed by Jacques Beckers, and full details can be found in Appendix 13.01.

The SHABAR (a contraction of the phrase Shadow Band Ranging), is a new instrument developed by Jacques Beckers. It is based on the well-known fact that the localized variations of the index of refraction in the atmosphere produce fluctuations in the intensity of stars. This was extended to the Sun by Seykora (1993), who used a single scintillometer to estimate daytime seeing. Beckers (see Appendix 13.01) realized that an array of scintillometers could be used to estimate the daytime seeing as a function of height. The method has also been applied to night-time observations, using the moon as a source, by Hickson & Lanzetta. Figure 8.1 shows the S-DIMM and the SHABAR detector head mounted on the Meade telescope during a test at Sac Peak.

Figure 8.2 shows the computer screen displayed during the operation of the seeing monitor. On the left is an image of the S-DIMM slits. The relative motion of the ends of the slits is related to the value of the Fried parameter, r_0 integrated over the entire atmosphere. The instantaneous value of r_0 over 10-s intervals is shown as the yellow curve in the upper panel on the right side of the screen. The middle panel on the right side of the screen shows the average intensity as the red curve, and the scintillation as the green curve. The anti-correlation between r_0 and the scintillation can be clearly seen. Finally, the lower panel on the right shows three of the 15 cross-correlation curves between pairs of scintillometers. It is these curves that contain information on the height variation of the seeing.



Figure 8.1 – The ATST seeing monitor. Visible are the two circular apertures for the S-DIMM, the linear array of six scintillometers for the SHABAR, and the Meade telescope.

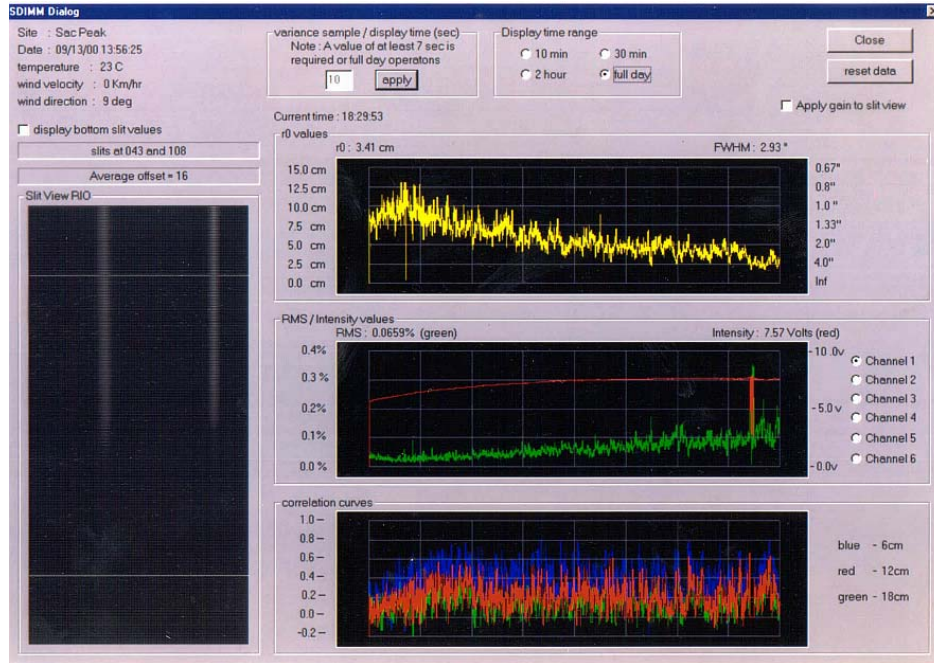


Figure 8.2 – The real-time operations screen of the seeing monitor. Left: images of the S-DIMM slit. Right top: yellow curve shows measurements of r_0 from the S-DIMM. Right center: red curve shows average intensity; green curve shows scintillation. Right bottom: three of the 15 cross-correlation curves.

8.2 SKY BRIGHTNESS MONITOR

The sky brightness monitor was designed by Haosheng Lin at the University of Hawaii, and is described in detail in Appendix 13.6. It essentially is a miniature coronagraph, with a field of view of 2 to 6 solar radii, a CCD, and a filter wheel with bandpasses of 450, 530, 890, and 940 nm. Figure 8.3 shows the instrument under development at Haleakala.



Figure 8.3 – The sky brightness monitor.

8.3 DUST COUNTER

The dust counter is a Met One model GT-321 handheld aerosol particulate monitor with a sample time of one minute. It counts the particles with a vacuum system to collect 0.1 cubic ft of air, and a laser optical system to count and size the particles as they enter the vacuum orifice. The device is polled by the computer every ten minutes. The device is mounted on the top of the test stand, at a height of 6 m. This places the instrument above the ground where normal daily activities can stir up dust and affect the measurements. A picture of the device is shown in Figure 8.4

In practice, this instrument suffered from severe battery problems. Continual charging of the batteries resulted in their early demise. A strategy of frequent battery replacement instead of charging was adopted, but only a relatively small number of particulate samples were actually obtained.



Figure 8.4 – The Met One GT-321 aerosol particulate monitor

8.4 WEATHER STATION

The weather station provides measurements of wind speed in mph, wind direction in one of 16 directions, maximum wind gust during a sample, relative humidity, barometric pressure, and two temperatures. One of the temperature sensors is placed at the top of the test stand, and the other at the base. This gives a rough measure of the near-ground temperature gradient.

8.5 TEST STAND

In order to lift the seeing monitor above the ground boundary layer, the equipment was mounted on a test stand. The height of the test stand platform was specified at 6 m as a compromise between construction costs and the desire to place the monitor at a height that the ATST entrance aperture could be at. With the height of the Meade telescope pier and the telescope itself, the resulting effective height of the seeing measurement is 8 m.

The test stand was designed by John Briggs based on the ideas of Robert Hammerschlag, the designer of the Dutch Open Telescope tower. The ATST site survey test stand is designed such that the movement of the platform at the top of the stand is restricted to be translational in the horizontal plane without any tilting. This allows the S-DIMM to operate in winds up to 23 mph before the slit images do not remain in the measurement area. Figure 8.5 shows the top of the test stand with the seeing monitor. Figure 8.6 shows the test stand installation at each of the six sites.



Figure 8.5 – The top of the test stand with the seeing monitor (right), weather station anemometer (left), and mobile SHABAR unit (center)



Figure 8.6 – The test stand installation at the six sites. Top row, left to right: La Palma, Big Bear, San Pedro. Lower row, left to right: Haleakala, Panguitch, Sacramento Peak

8.6 TECHNICAL STAFF

- Steve Hegwer – Project manager
 - John Briggs – Project engineer
 - Larry Wilkins – Electronics engineer
 - Mark Komsa – Electrical Engineer
 - Ed Leon – Electronics
 - Scott Gregory – mechanical design & fabrication
 - Robert Rentschler – Civil engineering
 - Steve Fletcher – Programmer
 - Tony Spence – Electrical Engineer
 - Dylan Sexton – Electronics technician
-
- Panguitch Observer -- Jim Mason, Terry Bender
 - La Palma Observer -- Noel D. Torres Taño, Eberhard Besenfelder
 - BB observers – Randy Fear, Bill Marquette
 - HA observers – Les Hieda, Garry Nitta, Dan Ogara
 - SPM observers – Dave Hiriart, Raul Michael
 - Sac Peak Observers – John Cornett, Tim Henry

8.7 DEPLOYMENT AND MAINTENANCE HISTORY

This section contains a list of the instrument configurations and a list of the major maintenance events during the course of the survey.

8.7.1 Instrument configurations

Local Standard system:

Computer: SDIMM3
SDIMM head: SM2
Meade telescope: 126165
SHABAR amplifier box: #3

Sunspot system on "Menzel Test Stand" (MTS).

Computer: SDIMM2
SDIMM head: SM1
Meade telescope: 126539
SHABAR amplifier box: #6 (later changed)

Panguitch system.

Computer: SDIMM6 (later changed)
SDIMM head: SM6
Meade telescope: 1219
SHABAR amplifier box: #0

Baja system.

Computer: AURA1
SDIMM head: SM3
Meade telescope: 129319
SHABAR amplifier box: #1 (later changed to #7)

Big Bear system (BBSO).

Computer: AURA4

SDIMM head: SM4

Meade telescope: 129320

SHABAR amplifier box: #4

La Palma system.

Computer: SDIMM1

SDIMM head: SM7

Meade telescope: 129317

SHABAR amplifier box: #5

Hawaii system (MSO).

Computer: SDIMM4

SDIMM head: SM5

Meade telescope: 129318

SHABAR amplifier box: #9

8.7.2 Major Instrument Events

March 9, 2002: SDIMM wedge tests at Big Bear; also SDIMM stellar scale observations the evening of March 9-10.

April 4-5, 2002: SDIMM stellar scale observations for the Hawaii system after installation in Hawaii

April 5, 2002: Wedge tests at Hawaii.

July 14, 2002: Simultaneous run with Panguitch system and Local Standard at Evans.

August 28, 2002: Stellar scale measurements conducted after installation at Panguitch.

September 30, 2002: Two runs of stellar scale measurements after installation at La Palma.

October 30, 2002: Hawaii's SDIMM science camera (#366111) dies; unit is serviced at Sunspot using replacement camera #366112.

November 14, 2002: The hard disk crashed on computer AURA1 of the Baja system.

November 16, 2002: Baja system and Local Standard ran together at Evans on this day and also November 19, 20, and 21.

November 21, 2002: Repeat SDIMM stellar scale measurements for the Baja system.

January 14, 2003: SDIMM head returned broken from La Palma. At Sunspot, replaced broken science camera with one recently refurbished by the manufacturer.

January 15, 2003: Afternoon run of La Palma's rebuilt SDIMM unit "SM7" using the Local Standard telescope (#126165) and computer at Evans. Similar runs on Jan. 17 and 21.

January 20, 2003: The computer at Panguitch was changed from SDIMM6 to SDIMM5. SDIMM6, repaired, becomes spare at Sunspot.

February 6, 2003: First data after installation at Baja. SDIMM wedge tests Feb. 7th. Visit cut short by bad weather.

March 21, 2003: Lightning strike at Sunspot killed the photodiode array and SHABAR amplifier box #6. Temporarily moved the diode array from Local Standard to the Sunspot system and began using SHABAR box #8 on the Bridge. Began building a replacement diode array named "MTS2."

April 8, 2003: Recently shielded the ground-level T2 temperature sensor at Sunspot from direct sunlight, to match installations at other sites (except Big Bear, for which the T2 sensor is near the lake water line, but is nonetheless usually exposed).

April 11, 2003: Final tests of the new MTS2 photodiode array at Evans; installation in the Sunspot system was shortly afterwards. The array original to Local Standard was returned to Local Standard at this time.

August 26, 2003: Jim Mason reports camera failure at Panguitch. His SDIMM unit "SM6" is returned to Sunspot. The dead science camera #366899 was replaced with #229117. Mason did SDIMM wedge tests after JWB's reassembly at Panguitch.

October 20, 2003: The Baja SHABAR has been inoperative for some time, likely because of a lightning strike. The SDIMM and Meade were repaired and functional briefly recently, but the Meade has failed in a new way. JWB returns to Baja and replaces the SHABAR and Meade components.

November 2003 The SDIMM, SBM and Shabar instrument operations were terminated at Sac Peak, Panguitch Lake and San Pedro Martir. Most of the instruments were returned to Sac Peak. The Panguitch Lake SBM was sent to Haleakala.

Jan 2004 An SDIMM was setup at Erie, Colorado for a cross calibration check with the ATD Sonic Anemometers mounted on the 300 meter tower

March 2004 The Evans Visual Sky Photometers were sent to Big Bear, Haleakala and La Palma to provide a sanity check for the SBM measurements

April 20, 2004 Replaced Wx station at BBSO

April 21, 2004 Replaced La Palma SBM camera and controller

April 21, 2004 Replaced La Palma SDIMM computer

April 27, 2004 Replaced Haleakala Meade controller board

April 2004 The new 2.0 reflective ND filters are installed on the SBMs to replace those with pinhole problems

April 2004 The sonic anemometer/hygrometer/scintillometer system was deployed on a crane at Big Bear for 30 days

June 2004 The sonic anemometer/hygrometer/scintillometer system was deployed on a crane at Haleakala for 30 days

July 8, 2004 Replaced BBSO weather station

July 15, 2004 Replaced La Palma SDIMM computer

August 6, 2004 Replaced Haleakala Meade controller board

8.8 CALIBRATION AND TESTING

8.8.1 Validation tests, Assembly level

8.8.1.1 SHABAR

- Electrical gain measurements for all DC and AC channels; AC bandpass measurement (lower limit), all channels.
- Electrical response tests (2), diagnostic data mode. One sequence with DC input only (output at ~8 v), another with both DC (output at ~8 v) plus AC (output at ~ 10 mv, 50 hz(?)). Same input presented to all channels, at diode end of cable. (LW & RR)
- Correlation test, normal data mode, 2-sec cadence. Inject DC (~8v) and AC (~10mv) into all channels at diode end of cable. Step AC through 50, 100, 250, 500, 750, 1000, 1500, 2000 hz, dwelling about 3 minutes per step. Takes about 1 hour. (JB or LW)
- Optical response tests, diagnostic data mode (10-sec bursts), to characterize pickup, dark current, crosstalk, etc. One sequence with micro-telescopes covered (dark), a second with all micro-telescopes open to sunlight, finally, a series of six, each with only one of the micro-telescopes open, in sequence. Requires clear sky. (JB)
- Common input test. Output from one reference diode, exposed to sunlight, distributed through all inputs of unit under test. (LW & JB)
- Transit scan tests, normal data mode, 2-sec cadence. One scan with bar oriented E-W, another N-S Requires clear sky. (JB)

- Raster scan test, normal data mode, 2-sec cadence E-W & W-E scan pairs, spaced about 1/2 degree in declination, sampling the entire FOV of the microtelescopes. Takes 2-3 hours on Meade mount, labor-intensive, requires clear sky. (JB)
- Cable check. (LW)

8.8.1.2 SDIMM

- Wedge tests.
- Double star separation measurements to determine plate scale.

8.8.2 Validation tests, end-to-end system level

Clear sky throughout.

- Optical response tests, diagnostic data mode (10-sec bursts). One sequence with micro-telescopes covered (dark), a second with all microtelescopes open to sunlight, finally a series of six, each with only one of the telescopes open, in sequence.
- Software tests. Exercise various SOH (state of health) conditions.
- Exercise observing procedure & scripts, including SHABAR and SDIMM diagnostic modes and normal observing mode.

8.8.3 Certification tests

8.8.3.1 DAILY

- SHABAR optical response test, diagnostic data mode. One sequence with all micro-telescopes open to sunlight.
- SDIMM response, diagnostic data mode. One sequence after setup, focus adjustment, etc, completed.

8.8.3.2 MONTHLY (OR AS SPECIFIED)

- Optical response tests (8), diagnostic data mode (10-sec bursts). One sequence with micro-telescopes covered (dark), a second with all micro-telescopes open to sunlight, finally a series of six, each with only one of the telescopes open, in sequence.
- Transit scan test, normal data mode, 2-sec cadence. One scan with bar oriented E-W on the Meade mount.
- Wedge tests.

8.8.4 Results of SHABAR assembly tests and calibration

8.8.4.1 TEST A1

R. Radick & L. Wilkins 30 Nov 01

Summary of SHABAR assembly level test A1: Electrical gain measurements for all DC and AC channels; AC bandpass measurement (lower limit), all channels.

Electrical gain measurements were made on SHABAR boxes #'s 0-9 by L. Wilkins, using a digital meter, and compared with previous measurements made by E. Leon. Box #3 was remeasured three times, and two digital diagnostic files were also recorded by computer for that box. One of these two files (... 011116 165637) was compared in detail to its corresponding manual file.

1. The four manual measurements for box #3 show very high repeatability (rms distance 8.7 ppm, or about 0.1%) in the DC/AC gain ratios. The comparison between the digital and manual measurements showed differences that averaged less than 0.03% (!).

2. The Wilkins and Leon measurements were compared by computing percentage differences, rms distances and correlation coefficients. In general, the agreement was poorer than for the repeat measurements on the same box (#3) by a factor of 5x or so, even in the best cases. Some of the discrepancies may have arisen when some of the amplifiers were changed, which happened at some point between the two sets of gain measurements. Overall, the agreement seems satisfactory for box #'s 0,1,2,4,5,6, and 8. It appears that boxes 3 and 7 may have been interchanged at some time between the two sets of gain measurements.
3. Recommend updating gain ratios as shown in Table 8.1. The values are those measured by Wilkins except for box #3, which is the average of the four manual measurements plus the one diagnostic file analyzed.

Table 8.1 – Preliminary AC/DC gain ratios for the SHABAR arrays

	Chan 0	Chan 1	Chan 2	Chan 3	Chan 4	Chan 5
Box 0	0.009313	0.009625	0.009775	0.009985	0.009104	0.009958
Box 1	0.009453	0.009947	0.009479	0.009751	0.009401	0.009541
Box 2	0.009784	0.009373	0.009965	0.009656	0.009305	0.009588
Box 3	0.009562	0.009445	0.009431	0.009387	0.009382	0.009453
Box 4	0.009682	0.010151	0.009568	0.009484	0.009511	0.009548
Box 5	0.009307	0.009343	0.009477	0.009443	0.009149	0.009487
Box 6	0.009332	0.009555	0.009196	0.009417	0.009410	0.009316
Box 7	0.009957	0.009788	0.009518	0.009174	0.009582	0.009316
Box 8	0.009340	0.009429	0.009564	0.009468	0.009404	0.009435
Box 9	0.009632	0.009435	0.009121	0.009621	0.009502	0.009658

4. Bandpass measurements showed no anomalies.

Addendum - R. Radick & L. Wilkins - 03 Jan 02

After modification of unit #8, as described in test report A2, the gains for that unit were re-measured. The updated gain table is shown below (new values for Box 8 highlighted in **boldface**):

Table 8.2 – Final AC/DC gain ratios for the SHABAR arrays

	Chan 0	Chan 1	Chan 2	Chan 3	Chan 4	Chan 5
Box 0	0.009313	0.009625	0.009775	0.009985	0.009104	0.009958
Box 1	0.009453	0.009947	0.009479	0.009751	0.009401	0.009541
Box 2	0.009784	0.009373	0.009965	0.009656	0.009305	0.009588
Box 3	0.009562	0.009445	0.009431	0.009387	0.009382	0.009453
Box 4	0.009682	0.010151	0.009568	0.009484	0.009511	0.009548
Box 5	0.009307	0.009343	0.009477	0.009443	0.009149	0.009487
Box 6	0.009332	0.009555	0.009196	0.009417	0.009410	0.009316
Box 7	0.009957	0.009788	0.009518	0.009174	0.009582	0.009316
Box 8	0.009616	0.009418	0.009117	0.009620	0.009487	0.009654
Box 9	0.009632	0.009435	0.009121	0.009621	0.009502	0.009658

8.8.4.2 TEST A2

R. Radick & L. Wilkins -- 18 Dec 01

Summary of SHABAR assembly level test A2: Electrical response tests (2), diagnostic data mode. One sequence with DC input only (input set to create a ~8 to 9 V output on the DC outputs), another with both

DC input (input again set to create a ~8 to 9 V output on the DC outputs) plus AC (input set to create $\sim \pm 8$ to 9 V, or roughly 6 V rms, on the AC outputs, at ~ 50 Hz). With the gain setting we have chosen, and with the resistor values we are using to split up the signal, this requires 7 VDC and .040 VAC rms. Same input presented to all channels, at diode end of cable.

Electrical response measurements were made on SHABAR units 0-9 by L. Wilkins, using signal generators to supply the inputs and recording the digitized data using the SHABAR diagnostic data application (acdc data file ...). Evaluation of test data was performed by R. Radick

1. The first series of tests indicated the presence of spiky pickup at the level of about 100 mv pk to pk ($\sim 0.5\%$) in all AC outputs of all units. Further analysis indicated that this was not 60 Hz pickup - the indicated frequency was, if anything, around 20 Hz. Further investigation showed that the sensor cable shield, attached to chassis ground, was coupling power supply noise to the AC outputs, which were referenced to a separate ground. To correct this, the two grounds were made common at the SHABAR box.
2. Retest indicated that the pickup problem had been eliminated – no artifacts were observed at a level exceeding 0.1%, except for unit #8, which showed 90-100 Hz noise present in several AC output channels, ranging up to 200 mv pk to pk ($\sim 1\%$) in one channel. Investigation showed that capacitors involving the input amplifier, which had been changed for the other units, had not been changed for this unit.
3. After modification, retest of unit #8 showed no DC or AC output anomalies.
4. At present, none of the units show DC or AC output anomalies at levels exceeding 0.1%, and units 8 and 9 appear to be particularly well-behaved. Gain measurements (test A1) will be repeated for the modified unit #8.

8.8.4.3 TEST A3

R. Radick & L. Wilkins -- 04 Jan 01

Summary of SHABAR assembly level test A3: Correlation test, normal data mode, 10-sec cadence. Inject DC and AC into all channels at diode end of cable, with inputs set to create 8-9 V outputs, both DC and AC. Step through 50, 100, 250, 500, 750, 1000, 1500, 2000 Hz, dwelling about 3 minutes per step.

Measurements were made on SHABAR boxes #'s 0-9 by L. Wilkins. Evaluation of the test data was performed by R. Radick.

1. Background: Last summer, test measurements performed by P. Jibbons showed that the AC correlation between SHABAR output channel pairs, when driven by nominally identical electrical inputs, was significantly less than the expected value of unity. Further test measurements showed that the degradation increased with the frequency of the input and with the time interval between the A/D samples, ranging from as much as 1% at 100 Hz to as much as 20% at 500 Hz. The worst pairs showed anticorrelation above about 1200 Hz. This behavior was attributed to delays associated with polling the A/D, which was done in an interrupt-driven mode, roughly 330 times per second with about 26 μ sec between sequential A/D channel reads. To remedy this, the software was rewritten to poll the A/D in burst mode, which captures 14x10000 samples over 10 seconds, with about 4 μ sec between sequential A/D channel reads. This alleviated the problem substantially – retest of one unit showed the degradation had been reduced to about 0.1%, at worst, at 100 Hz, and about 0.3%, at worst, at 500 Hz.

2. Subsequent modifications to the circuitry to reduce settle time appear to have alleviated the problem even further, especially at the low frequencies that are of greatest concern for measuring solar scintillation. The degradation now appears to be 0.01% or less, at worst, at 100 Hz, and 0.2% or less, at worst, at 500 Hz. It was discovered, however, that the progression of the degradation does not always follow the expected sequence, in the sense that the correlation between two channels (0 and 4, say) might be closer to the expected value of unity than that for two channels (0 and 3, say) sampled more closely in temporal sequence. This behavior was found in units 0, 2, 4, 6, 7, and 8, but not the others. We suspect it may have to do with variations in the lag intrinsic to the circuit, but also conclude that it does not merit further attention at this time.
3. The following table list representative results of the measurements for 100, 250, and 2000 Hz. Degradation is the reduction of the correlation coefficient below the expected value of unity, in percent, for the worst pair of channels, generally (0,5). Order is the progression of the degradation in channel pairs (0,1), (0,2), (0,3), (0,4), and (0,5) = (1,2,3,4,5) – the expected sequence is 12345. An “x” indicates presence of at least one deviation from the expected order.

8.8.5 S-DIMM Plate Scale Measurements

In order to calibrate the S-DIMM measurements from limb displacements to r_0 in cm, it is necessary to know the plate scale of the S-DIMM in arcsec per pixel. This was done by repeatedly observing double stars with well-known separations through the S-DIMM optical system. The analysis of this data provides table 8.3 of S-DIMM plate scales.

Table 8.3 – S-DIMM Plate Scale Measurements

Site	System (Telescope + SDIMM Head)	Measurement 1 (Arcsec/pixel)	Measurement 2 (Arcsec/pixel)	Measurement 3 (Arcsec/pixel)	Measurement 4 (Arcsec/pixel)
Local Standard	165+SM2	0.428 ± 0.022	0.445 ± 0.003	0.435 ± 0.003	0.441 ± 0.003
Haleakala	318+SM5	0.422 ± 0.003	0.445 ± 0.003	---	---
San Pedro	319+SM3	0.447 ± 0.004	0.433 ± 0.005	0.439 ± 0.003	---
Big Bear	320+SM4	0.458 ± 0.004	0.458 ± 0.003	0.426 ± 0.003	0.442 ± 0.003
Sac Peak	539+SM1	0.421 ± 0.004	---	---	---
La Palma	317+SM7	0.407 ± 0.004	0.453 ± 0.005	---	---
Panguitch	994+SM6	0.429 ± 0.004	---	---	---

The mean and standard deviation of all measurements is 0.437 ± 0.014 , with a peak-to-peak variation of 12.5% and an expected variation of 3.2%. The peak-to-peak variations and scatter in the measurements are probably due primarily to temperature variations during the nights when the observations were obtained. However, the overall variation between instruments is better estimated by the expected variation of 3.2%.

9. DATA REDUCTION

9.1 INGEST

The data arrives in Tucson on a CD which typically contains 1 to 8 weeks of seeing data. SBM data also arrives on CDs which are usually separate from the seeing CDs. The seeing CDs are copied onto a Sun workstation and file name problems resulting from Windows naming conventions are resolved by opening every file and constructing a new file name from information in the header. Quick-look plots which display every quantity are generated. An example of one of these plots is shown in Appendix 13.9.

9.2 DATA CULLING AND FLAGS

The data files contain a state of health flag whose bits are set to indicate various problems with the instrument as listed in Table 9.1.

Table 9.1 – Data flags

Flag Value	Event
0	Good data
1	Failed video
2	Failed Meade
4	Failed Weather station
8	Failed SHABAR
16	Non-zero rail count (high wind)
32	Observing log entry

Simultaneous events add numerically, i.e. If the weather station and the SHABAR have both failed, then the flag value is 12. Of these flags, the most commonly occurring in the data are 2 and 8. The 2 flag (FAILED MEADE) is associated with a timeout condition when the S-DIMM software is attempting to read the Meade's right ascension position during Meade communication port initialization or if the read of the Meade's right ascension was not completed during normal operations. The intent of the flag is to identify periods of possible RA drift. If this flag is set just once it remains set throughout the data run. Data obtained with only the flag 2 set is still valid since a read of the RA position of the telescope will not affect the data. The 8 flag (FAILED SHABAR) indicates that the average value of a DC channel over a 10 second sample period differs by greater than 30% from the average value of any other DC channel over the same 10 second sample. This condition occurs almost exclusively when there is no light reaching the SHABAR detectors. In virtually all cases this means that the seeing instrument is stowed but still powered on to collect weather data. The 16 flag (NONZERO RAIL COUNT) indicates that the slit images of the S-DIMM have moved outside the designated measurement area. This happens when a high wind occurs, typically greater than 10 m/s. The existence of these flags is checked in the course of the processing and data is discarded on the basis of these values. In particular, the presence of the 8 or 16 flag, as well as a zero reading from the S-DIMM, is commonly present when the S-DIMM/SHABAR is shut down but the weather station is running.

9.3 SHABAR/S-DIMM ANALYSIS

The data analysis to estimate $r_0(h)$ proved to be challenging. It essentially comprises the fitting of the observed scintillation cross-covariances as a function of detector separation with a model of the structure function, $C_n^2(h)$, composed of weighting functions derived from the theory of atmospheric turbulence. In addition, the integral of the model over the atmosphere is required to fit the observed S-DIMM value of r_0 . Since the release of the interim report, a considerable amount of effort has gone into understanding and improving this analysis. Several verification tests have been performed -- simulations, comparisons between simultaneous SHABAR/S-DIMM r_0 estimates at different heights, comparison between completely different methods of estimating r_0 and, most recently, comparison with in-situ measurements of $C_n^2(h)$. In all cases the analysis provides a reasonable estimate of $r_0(h)$ up to 50 m in height.

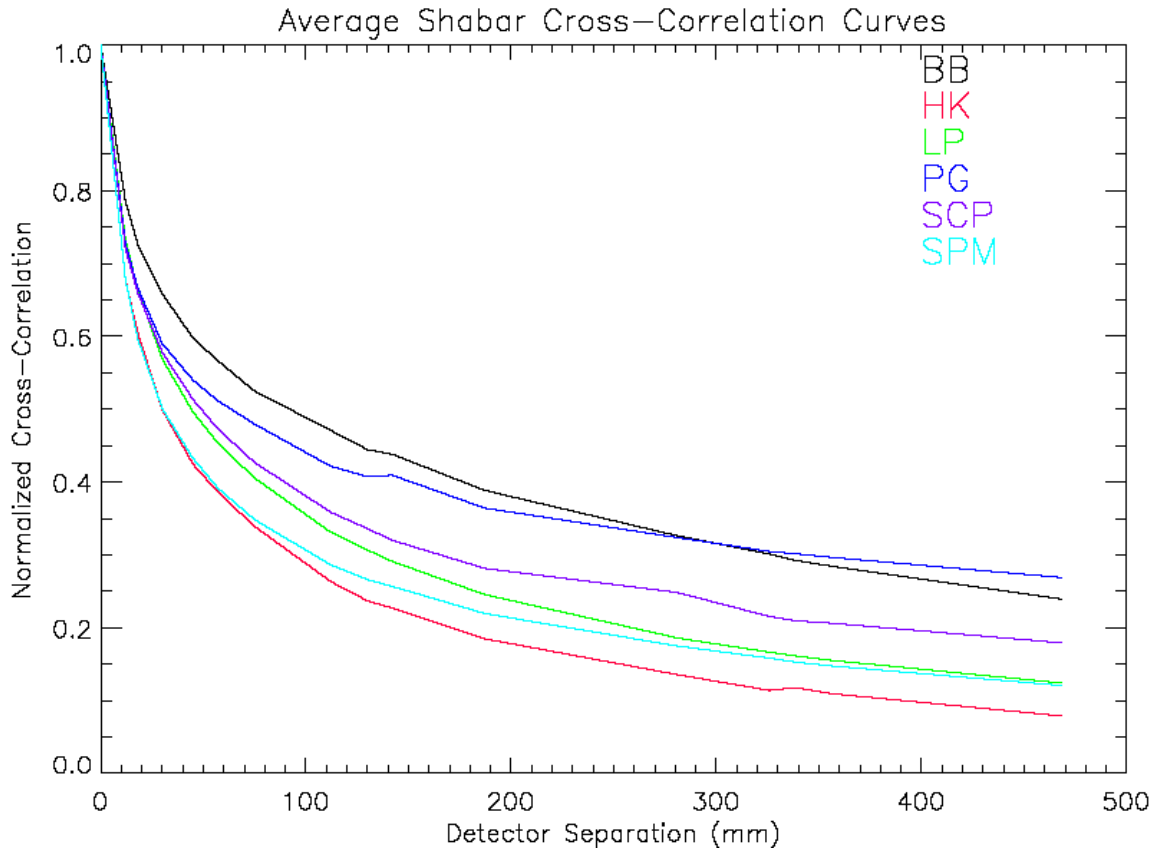


Figure 9.1 – The average cross-correlation curves for the sites as of October 2003. The two lake sites, Big Bear (BB) and Panguitch (PG), have relatively shallow curves as a function of detector separation which indicates that the seeing arises from a region far above the instrument. The four non-lake sites have a relatively steeper cross-correlation as a function of separation, indicating a boundary layer near the telescope.

As an illustration of the method, Figure 9.1 shows the average observed normalized cross-correlation (not cross-covariance) for each of the six sites. The cross-correlation, normalized by the observed scintillation, ranges in value from +1 (complete correlation, achieved with the correlation of a detector with itself), to -1 (complete anticorrelation). The theory shows that cross-correlation curves are more sharply curved when the seeing is close to the detector, and less so when the seeing is far away. This behavior can be seen in Figure 9.1.

To estimate the physical magnitude of $C_n^2(h)$, the cross-covariances with the scintillation measurements must be used. Thus, the observed cross-correlation functions must be rescaled by the observed scintillation to produce the cross-covariance functions that are then fitted by the model. Ideally, all of the detectors would be exactly similar in their response to intensity fluctuations and the rescaling factor for each detector pair would be the square root of the product of the scintillation measured by each detector in the pair. In practice there are gain variations as discussed in section 8.8.4. Thus, the rescaling factor is the average scintillation observed by all six detectors during the sample interval.

The details of the theoretical foundations and some tests of the method are contained in the appendices (13.2, 13.3, and 13.10). Since the interim report, we have implemented two independent algorithms to perform the analysis. Here we present the details of the two methods, discuss some of the caveats of the method and illustrate some additional tests of the reliability of the results.

9.3.1 The Inversion Methods

The two methods were developed by Manuel Collados (the IAC method), and Hector Socas-Navarro (the HAO method.) They both perform a fit of a model $C_n^2(h)$ to the observed cross-covariances $B_I(d)$, which are the cross-correlations seen in Fig. 9.1 normalized by the observed scintillation and d is one of the 15 possible detector separations. In addition to these values, the models must also fit r_0 (or $r_0^{-5/3}$) as measured by the S-DIMM, and the observed total scintillation s . The methods differ in the details of the fitting procedure, pre-treatment of the data, and the inclusion of the high-altitude seeing which is not sampled by the SHABAR but substantially affects the S-DIMM measurement.

9.3.1.1 IAC METHOD

Before proceeding with the inversion, the data is processed thusly:

1. The median of the six measured scintillation values is taken as s at each sample. The median is used, instead of the mean, as sometimes individual detectors show anomalously large values due to flying dust or insects during the integration time.
2. A 31-point running mean is applied to the temporal variation of each parameter, corresponding to a five-minute average. This reduces the larger fluctuations in the parameters caused by turbulence. Note that the output number of points is the same as the input, except for the first and last 2.5 minutes. These two intervals are discarded and not used in the analysis. All points with an instantaneous S-DIMM $r_0 = 0$, or a SHABAR flag equal to 8 or 10 are not included in the average. A minimum of five points in every five-minute interval is required. Otherwise, the interval is rejected and not analyzed.
3. The zenith angle z of the sun at each moment is computed. The only input required here is the Universal Time and geographical coordinates of the site. The zenith angle is needed to compute the kernel functions for a particular time

The cross-covariance $B_I(d)$ between the normalized intensity fluctuations measured by two detectors separated by a distance d and observing the entire solar disk is given by the equation

$$B_I(d) = \int_0^\infty W(h, d) C_n^2(h) dh. \quad (9.1)$$

The scintillation s follows the same equation with $d=0$. Figure 9.2 shows the weighting functions or kernels $W(h, d)$ for the scintillation and the 15 baselines between the six SHABAR detectors as a function of height up to 10 km. Details of the calculation of $W(h, d)$ can be found in Appendix 13.2.

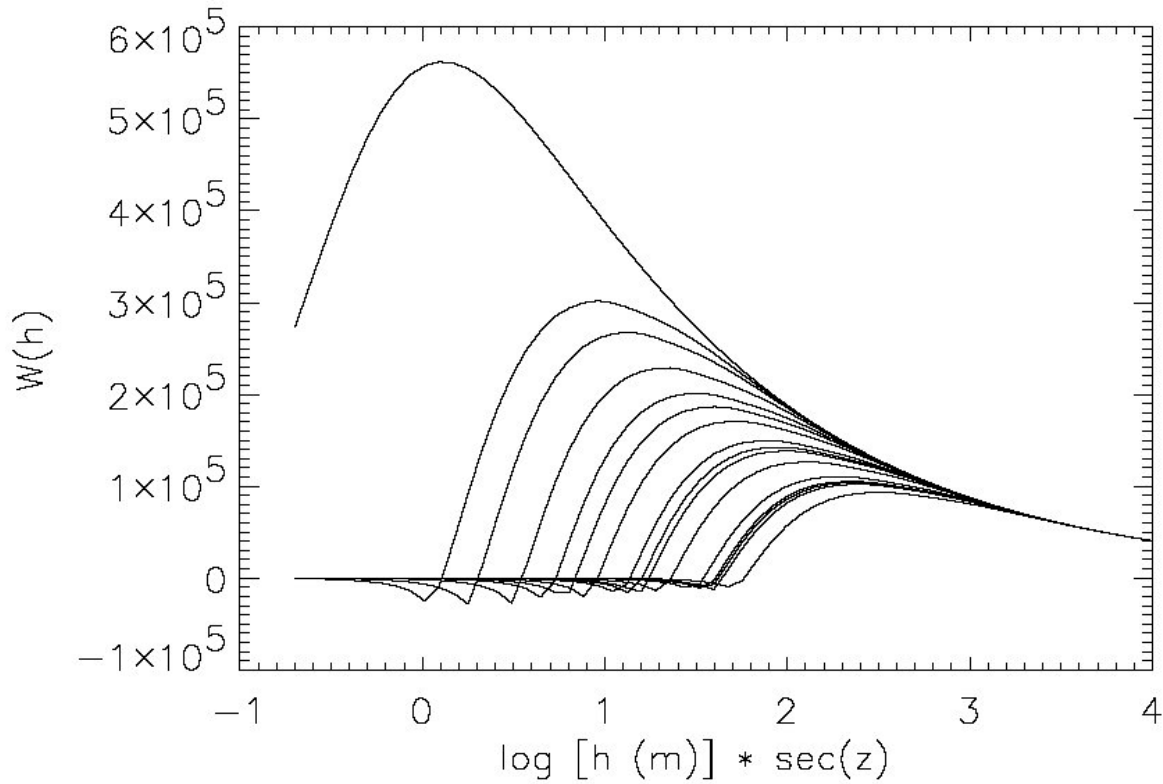


Figure 9.2 – Height dependence of the weighting function $W(h,d)$ for the scintillation and the fifteen values of d available in the SHABAR. The upper and lower curves correspond, respectively, to the smallest and largest separations (0 and 468 mm). z is the solar zenith angle.

The Fried parameter is given by

$$r_0^{-5/3} = C \sec(z) \int_0^\infty C_n^2(h) dh, \quad (9.2)$$

where C is a constant.

The procedure for determining $C_n^2(h)$ is as follows:

- 1) Define N reference heights (nodes) h_i , $i = 1, \dots, N$ at which C_n^2 will be estimated. The first node is located 20 cm above the instrument, the second 1 meter, and the remaining are equidistant in the logarithm of the height up to a maximum value defined by the user. For the ATST site survey, $N=68$ and the maximum height is 40 km. This location of the nodes proved to be efficient during the testing of the method.
- 2) Evaluate the interpolation coefficients that allow the determination of $C_n^2(h)$ at any height h from the values at the nodes. A linear interpolation in a $(\log(h), C_n^2)$ grid is used.
- 3) Compute the weighting functions $W_{node}(h_i, d_j)$ for nodes $i = 1, \dots, N$ and detector separations r_j , $j = 1, \dots, 16$. Then the equations relating the observables and $C_n^2(h)$ can be written as

$$B_I(d_j) = \sum_{i=1}^N W_{node}(h_i, r_j) C_n^2(h_i), \quad (9.3)$$

and

$$r_0^{-5/3} = \sum_{i=1}^N W_{node}^{r_0}(h_i) C_n^2(h_i). \quad (9.4)$$

Here, the weighting function W for r_0 is simply the constant $C \sec z$ [MANOLO – is this right?]

4) To ensure that $C_n^2(h_i)$ is always positive, it is replaced by $\exp[y(h_i)]$. Then any positive or negative value of y will produce a positive value of $C_n^2(h_i)$.

5) A standard non-linear least-squares technique is used to obtain the values of $C_n^2(h_i)$ that minimize the χ^2 of the fit, with

$$\chi^2 = \sum_{i=1}^{17} \left(\frac{x_i^{obs} - x_i^{synth}}{\sigma_i} \right)^2, \quad (9.5)$$

where the vectors x_i^{obs} and x_i^{synth} , $i = 1, \dots, 17$, are constructed from the observed and modeled values of the 15 cross-covariances plus the scintillation and r_0 . The values σ_i are the standard deviations of the observed quantities during the time interval being considered.

In practice, it turned out that a significant number of points could not be successfully inverted because the observed scintillation and cross-covariances were too small to be consistent with the observed r_0 . To account for this “missing scintillation”, a new parameter, Δs , was added to the observed scintillation and cross-covariances. This changes Eq. 9.3 to

$$B_I(d_j) + \Delta s = \sum_{i=1}^N W_{node}(h_i, r_j) C_n^2(h_i). \quad (9.6)$$

Equation 9.4 is unchanged.

With this addition, the minimization procedure is the same as before, with a constant value of Δs . Starting with $\Delta s = 0$, the stratification of $C_n^2(h)$ and the corresponding values of r_0 , s , and $B_I(d)$ are computed. If the modeled value of r_0 is larger than the observed value by more than one percent, then the value of Δs is increased by a given value and the procedure repeated until convergence between the model and observed values of r_0 is reached. The value of Δs is not allowed to be negative. If the modeled value of r_0 is less than the observed value for $\Delta s = 0$, the result is considered to be valid. The maximum allowed value of Δs is three times the observed scintillation. If this maximum is reached during the iteration, the point is rejected as invalid.

The fact that Δs is a constant added to both the observed scintillation and all of the cross-covariances implies that it somehow arises from high-altitude layers. This is evident from Figure 9.2, which shows that all of the kernels are identical above a height of about 1 km. However, the physical meaning of Δs is still obscure. Its presence implies that a source of image degradation, not producing scintillation, is required. One possible explanation is the existence of a finite outer turbulence scale. Turbulence can be thought of as being composed of cells of all sizes. Large eddies will produce corresponding large-scale

wavefront distortions, while small eddies will produce small-scale distortions. The S-DIMM will respond to large-scale distortions with high values of r_0 , and small-scale distortions with low r_0 values. In addition, the S-DIMM is most sensitive to small eddies due to the $-5/3$ exponent in Equation 9.2. On the other hand, scintillometers average phase fluctuations over a large area that increases with altitude. This spatial averaging will decrease the effects of small eddies and increase the sensitivity of the scintillometers to large-scale turbulence. With this scenario, the missing scintillation arises from a lack of large-scale eddies, i.e. a finite outer scale. The lack of the large eddies will not affect the S-DIMM measurements. The inclusion of Δs in the analysis produces a $C_n^2(h)$ profile consistent with the observed r_0 and a scintillation value that would have been measured if all scales of turbulence (up to infinitely large) had been present.

An alternative explanation for the need to include a missing scintillation term is as follows. The scintillation s is related to $C_n^2(h)$ by $s \propto \int h^{-1/3} C_n^2(h) dh$ and r_0 is related by $r_0 \propto \left[\int C_n^2(h) dh \right]^{3/5}$. Thus, the value of s is weighted towards low-altitude seeing and is less sensitive to high-altitude seeing, while r_0 is an unweighted integral. Thus, if the turbulence is located primarily at high elevations, then the value of s could be apparently inconsistent with r_0 . If this is the case, then more missing scintillation should be needed for successful fits at sites where there is little or no near-ground turbulent boundary layer. Figure 9.3 shows the distribution of the missing scintillation at the three sites. This plot clearly shows that the site with the most “missing scintillation” is Big Bear. This site is at a lake, which presumably substantially reduces the turbulence at low altitudes.

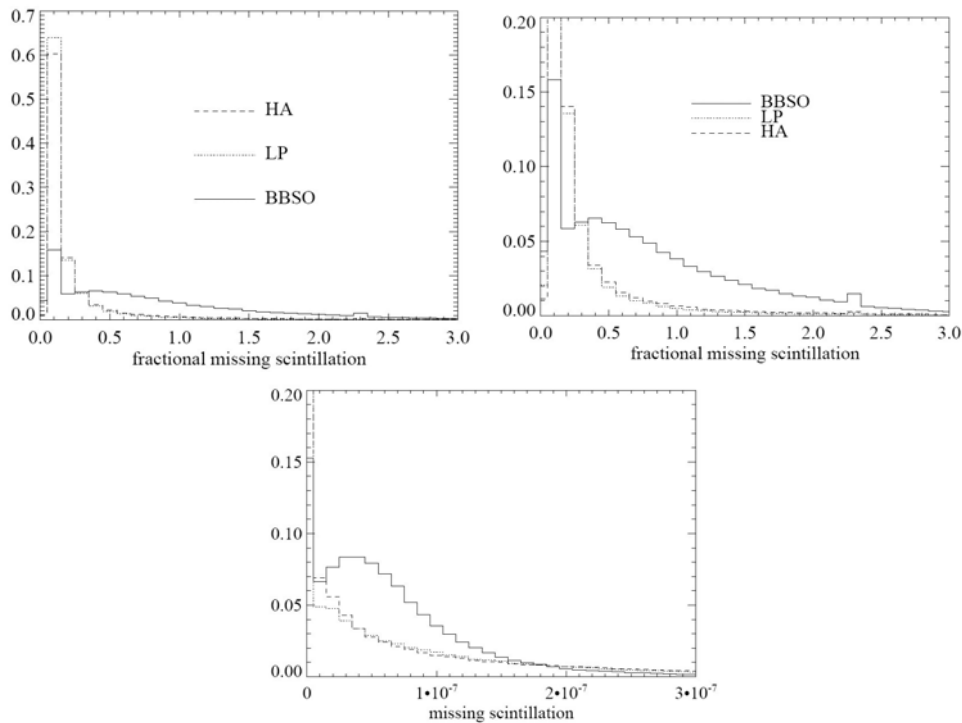


Figure 9.3: Histograms of the relative frequency of occurrence of “missing scintillation” Δs values at the three sites. Top two panels: relative occurrence of Δs as a fraction of the observed scintillation; left: entire distribution; right: zoom of lower portion. Bottom panel: relative occurrence of Δs as an absolute scintillation measure. Solid line: Big Bear; Dashed line: Haleakala; Dotted line: La Palma. Note that the two mountain sites (La Palma and Haleakala) typically require 10-20% fractional Δs while the lake site (Big Bear) frequently needs a substantially larger value.

9.3.1.2 HAO METHOD

This inversion code performs an iterative least-squares fit to the measured B_I . The fitting procedure is based on the Levenberg-Marquardt algorithm combined with Singular Value Decomposition (Press et al 1986) of the covariance matrix.

The SHABAR data are block-averaged in 5-minute intervals before the inversion. The SDIMM r_0 values are averaged in the same way, but taking into account the $-5/3$ exponent (see Eq. 9.9). During this step the presence of thin clouds is identified by looking for sign changes in the derivative of the intensity measured by the instrument. When this derivative changes sign two or more times within a 5-minute period, the entire block is flagged as cloudy. These points are considered as bad weather and the inferred $r_0(h)$ is set to zero for all heights.

The set of free parameters is a vector containing the values of C_n^2 at each height plus two other parameters, B_I^{high} and α , that account for high-altitude seeing. We start with a guess model that has 49 points equi-spaced in $\log(h)$ from -0.7 to 3.1 . The values of C_n^2 in this model are used to compute synthetic B_I according to Eq. 9.7. The integral in that equation is only evaluated from the model C_n^2 up to its maximum height H_m (approximately 1000 meters). The rest of the integral represents the high-altitude turbulence, and is retrieved by the inversion as a free parameter B_I^{high} :

$$B_I(d) = \int_0^{H_m} W(h,d) C_n^2(h) dh + B_I^{\text{high}} \quad (9.7)$$

with

$$B_I^{\text{high}} = \int_{H_m}^{\infty} W(h,d) C_n^2(h) dh \quad (9.8)$$

Notice that the high altitude contribution to r_0 has an important difference with respect to Eq. 9.8, namely the absence of the kernel function $W(h,d)$. Since the kernel is height dependent, it is not possible to convert B_I^{high} to an equivalent contribution to $r_0(h)$. We thus introduced an additional free parameter α so that:

$$r_0^{-5/3} = C \sec z \left(\int_0^{H_m} C_n^2(h) dh + \alpha B_I^{\text{high}} \right) \quad (9.9)$$

The integrals from $h = 0$ to $h = H_m$ that appear in Eqs. 9.7 and 9.9 are solved with parabolic accuracy using the following scheme. Let x_1 , x_2 , and x_3 represent $\log(h)$ at three successive grid-points. We assume that the kernel varies as a parabola: $W = w_1 x^2 + w_2 x + w_3$ for $x_1 \leq x \leq x_3$.

The function C_n^2 , on the other hand, exhibits an exponential variation with $\log(h)$: $C_n^2 = 10^{(ax^2 + bx + c)}$. This scheme requires some tedious algebra (details are provided in Appendix 13.3), but has the advantage of improved accuracy for a given height discretization.

The derivatives of B_I with respect to C_n^2 that enter the minimization algorithm are computed numerically by perturbing slightly the model atmosphere at each grid point. A standard regularization method is applied so that the algorithm has a preference for smooth models whenever possible. Several tests were carried out with a small subsample (May 2003 for the three candidate sites) varying the regularization parameter. We picked the largest value that yielded a satisfactory fit to the data.

In order to ensure that the inversion algorithm is robust and avoids secondary minima we use a multiple initialization strategy. For each observation we perform at least 5 different inversions with different initializations. The solution corresponding to the best fit (lowest χ^2) is selected. If the fits obtained from

the best solution are still not satisfactory, the code attempts up to 10 different inversions with random initializations.

9.3.2 Verification Tests

A number of tests have been performed to verify the technique. These tests are comparison of the two inversion methods, and comparison of the inversion results with in-situ measurements of C_n^2 at a number of sites. These tests supplement the simulations and multiple height comparisons that were described in the interim report.

The results of the comparison between the two inversion methods are summarized in Figure 9.4. This figure shows the cumulative distribution of the estimated r_0 at the three sites and at five heights, as derived from the HAO method (solid line) and the IAC method (dashed line). The agreement is quite good. There are discrepancies that appear at higher heights, where the SHABAR sensitivity is decreasing. This effect is also seen in the ATST/in-situ comparison.

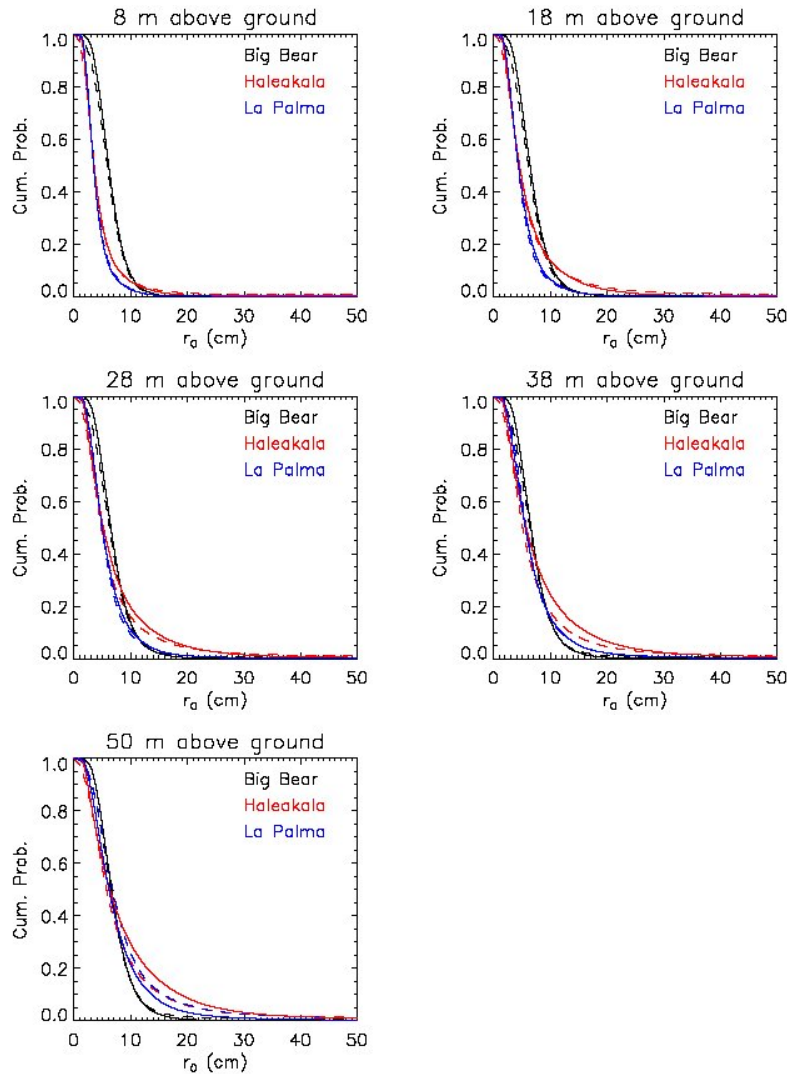


Figure 9.4: A comparison between the two inversion methods. Here we show the cumulative distribution of the estimated r_0 at the three sites and at five heights, as derived from the HAO method (dashed line) and the IAC method (solid line).

For a more detailed look at the inversion method comparison, Figure 9.5 shows $C_n^2(h)$ and $r_0(h)$ average curves for the month of May 2003 at the three sites.

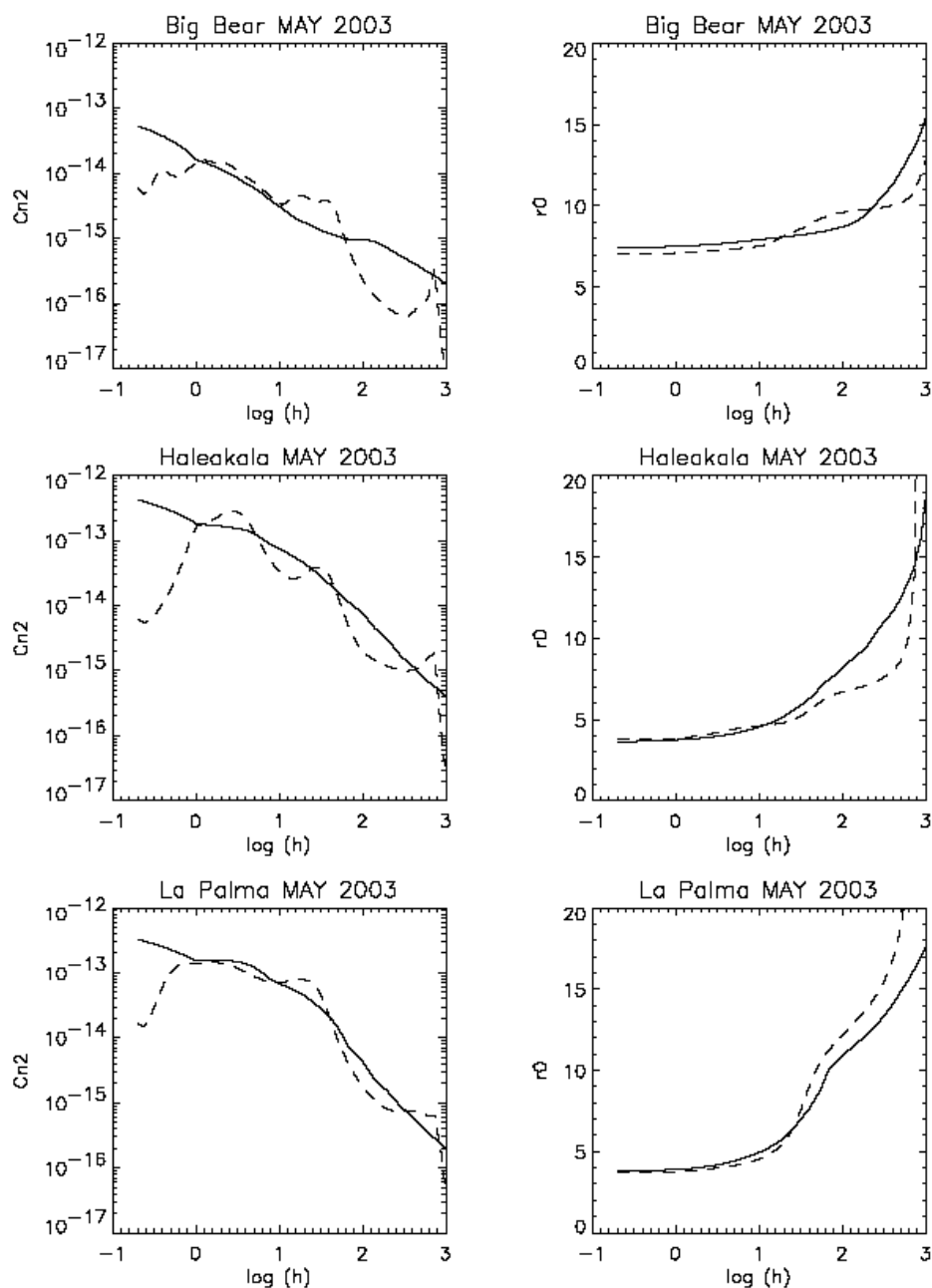


Figure 9.5: The estimated curves of $C_n^2(h)$ and $r_0(h)$ averaged over May 2003 for Big Bear, Haleakala, and La Palma. The two sets of lines are for the two inversion methods -- Dashed: HAO method, Solid: IAC.

Arguably the best verification of the method is to compare completely independent estimates of $C_n^2(h)$. To this end, an ATST seeing monitor was installed in Erie, Colorado, at the base of a tower that carried hygrometers, sonic anemometers, and other instruments (Hill et al. 2004, Figure 9.6) that could make in-situ measurements (Oncley and Horst 2004) of C_n^2 (derived from C_T^2 and C_q^2) at specific heights.

Temperature (T) and humidity (q) fluctuations were monitored at a 30 Hz rate; higher data rates were not warranted due to path averaging of the sonic anemometer. This data was then used to produce C_T^2 and C_q^2 (and thus C_n^2).



Figure 9.6: Sensors (hygrometers and sonic anemometers) mounted on a tower in Erie, Colorado for in-situ measurements of C_n^2 . These estimates are used to verify the ATST seeing analysis.

The results of this comparison are shown in Figure 9.7 which shows scatter plots of the ATST estimates verses those of the in-situ measurements for heights 5, 10, 22, 50, and 100 m. The Pearson correlation coefficient is shown on the plot, along with a line that indicates strict equality. This plot shows good agreement between the two measurements up to a height between 22 and 50 meters, verifying the measurements at heights relevant to the ATST. It should be noted that agreement between the two measurements is expected to drop off at a linear distance greater than 50 meters because the largest separation of the SHABAR solar irradiance scintillometers is 47 cm. This drop-off is more severe for the Erie measurements than is expected for measurements at the candidate ATST sites, because of the low sun angle ($\sec(z)$ always larger than 2.0) that prevailed during these mid-winter tests.

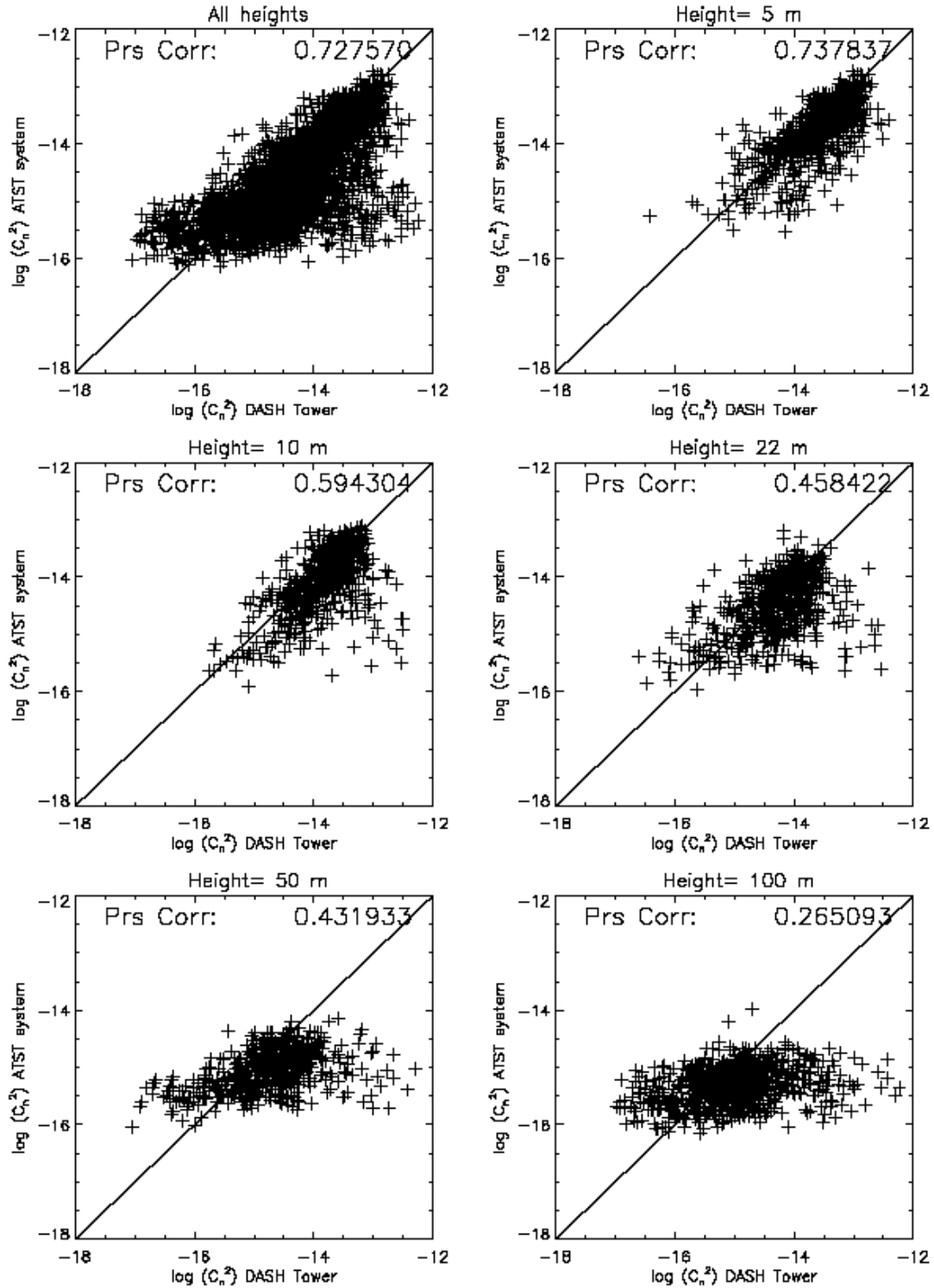


Figure 9.7: Results of the comparison of C_n^2 from the ATST system with in-situ measurements in Colorado.

To represent a lake and mountain environment the experiment was then repeated for three heights using a crane at Big Bear and Haleakala. Figure 9.8 shows the crane test at Big Bear and Haleakala; Figure 9.9 illustrates the spacing of the sensors. Additional details of the crane setup and experimental procedure can be found in Appendix 13.4.



Figure 9.8: The in-situ C_n^2 measurements underway at Big Bear (left) and Haleakala (right).

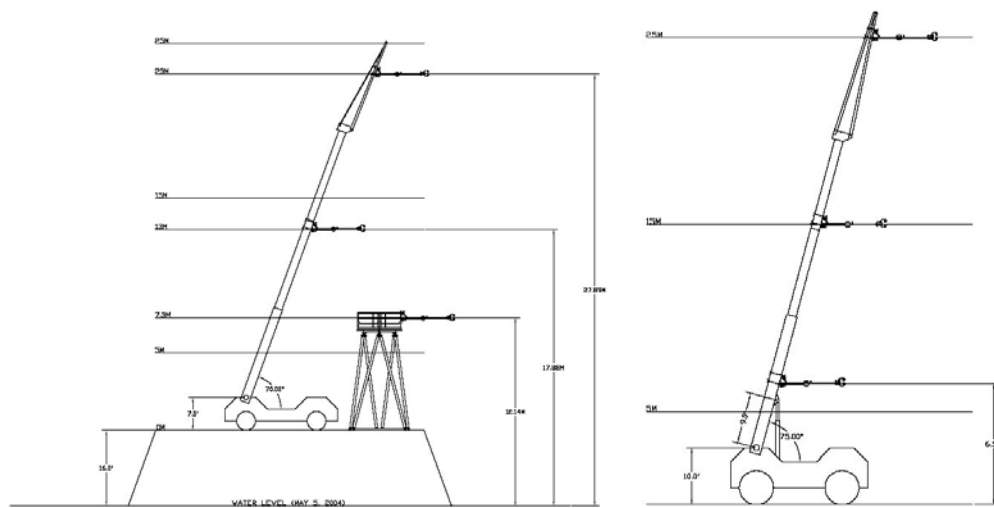


Figure 9.9: The crane at Big Bear (left) and Haleakala (right) with the in-situ probes, showing the heights of the sensors.

Figure 9.10 shows scatter plots of the ATST estimates versus those of the in-situ measurements for various heights at the two sites. Note that Pearson correlation coefficient shows good agreement (~ 0.87) between the two measurement techniques for the Haleakala data but only moderate agreement (~ 0.23) for the Big Bear data. The obvious differences between the two sites are: a significant difference in the level of humidity; the local topography and environment; and the probable lack of a near-ground boundary layer at Big Bear.

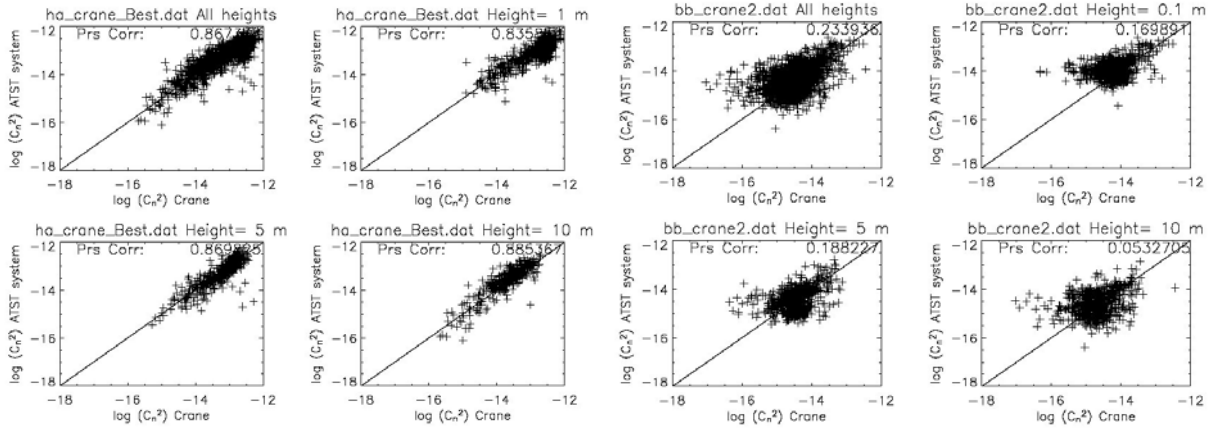


Figure 9.10: Scatter plot comparisons between the ATST estimates and the in-situ measurements of C_n^2 at Haleakala (left four panels) and Big Bear (right four panels). In each four-panel set the comparison is for the three heights of the in-situ measurements, plus all of the points combined. The straight line is strict equality, and each plot is labeled with the Pearson correlation coefficient (Prs Corr) of the data.

The presence of humidity does complicate in-situ measurements of C_n^2 as the correction to sonic temperature for humidity is of the same magnitude as the correction of C_T^2 to obtain C_n^2 . The corrections for humidity have been determined in terms of the Bowen ratio (Wesely 1976), so measurements of sensible heat flux and water vapor flux should have been adequate to correct both sonic temperature and C_T^2 for humidity.

The data set from crane measurements at Big Bear did however show a higher level of noise than that obtained from Haleakala. It is possible that the discrepancy with the Big Bear data could have been due to contamination of the temperature spectra by velocity spectra, which is caused by the finite time difference between successive sonic pulses. This is particularly important for small values of C_T^2 and hence C_n^2 . It is also possible that the lack of a boundary layer at Big Bear has reduced the scintillation signal to the point that the SHABAR measurements are dominated by noise. This is consistent with the site-dependent behavior of the “missing scintillation” discussed in Section 9.3.1.1. The Pearson correlation coefficient increases to ~ 0.58 if outlying data points ($> 2\sigma$), as well as points that may have been contaminated by clouds, are removed. This is shown in Figure 9.10

Of particular note for Big Bear data is May 12th 2004, which demonstrated the data’s dependence on wind speed and direction (Figure 9.11). On that day the typical westerly winds of 8 to 10 m/s changed to variable directions with velocities of 5 m/s or less. The resulting Pearson correlation coefficient for that data set was ~ 0.77 . This increased correlation may result from the presence of a ground boundary layer when the winds are not out of the west.

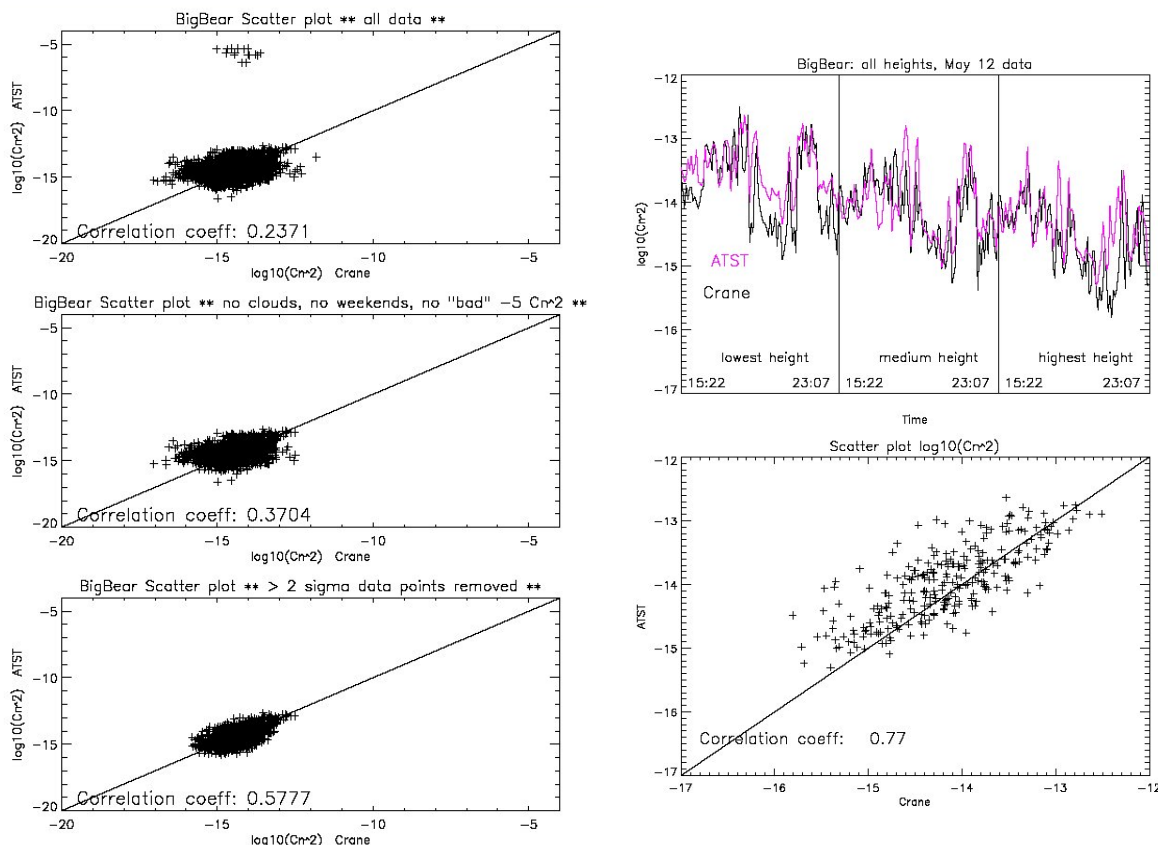


Figure 9.11: Left panels: The influence of noise on the correlation between the ATST and in-situ measurements of C_n^2 . Top Left: all data; middle: excluding possibly cloudy points; bottom: excluding points more than 2σ from the mean. Right panels: The correlations for Big Bear on May 12, 2004 when the winds were atypically variable. Top right: the time series for the three heights; bottom: the correlation for this day.

As a result of the comparisons between the ATST system and the in-situ measurements of C_n^2 we conclude that the SHABAR/S-DIMM analysis gives reliable results up to a linear distance of about 50 m from the instrument as long as there is sufficient near-ground turbulence to provide a significant scintillation signal.

9.4 SBM ANALYSIS

9.4.1 Overview of Data Analysis

A detailed treatment of the data analysis is discussed in Appendix 13.7, where one day from Sunspot and one day from Haleakala are analyzed.

The SBM images from all sites were examined to determine regions of valid sky measurements. In several sites the edge of the telescope tube is visible at the outer image edge; this defines the outer edge of the valid field-of-view. In all sites the diffraction from the occulter edge is visible which determines the inner edge of the valid FOV. Also the azimuth angles must be limited to avoid the shadow of (and diffraction from) the occulter support arms. A set of pixels with outer radial, inner radial and azimuthal limits was determined which avoided these problems in all images (i.e. from all sites and at all wavelengths). The same set of pixels is used for the images from all sites for all wavelengths. Figure 9.12 shows the valid sky pixels overlaid on a sample image from each site in the 890 nm wavelength channel.

Within these valid sky pixels several measurements are made. They include the mean sky brightness, sky brightness as a function of radial distance (γ), and the wavelength dependence of the mean sky brightness (β).

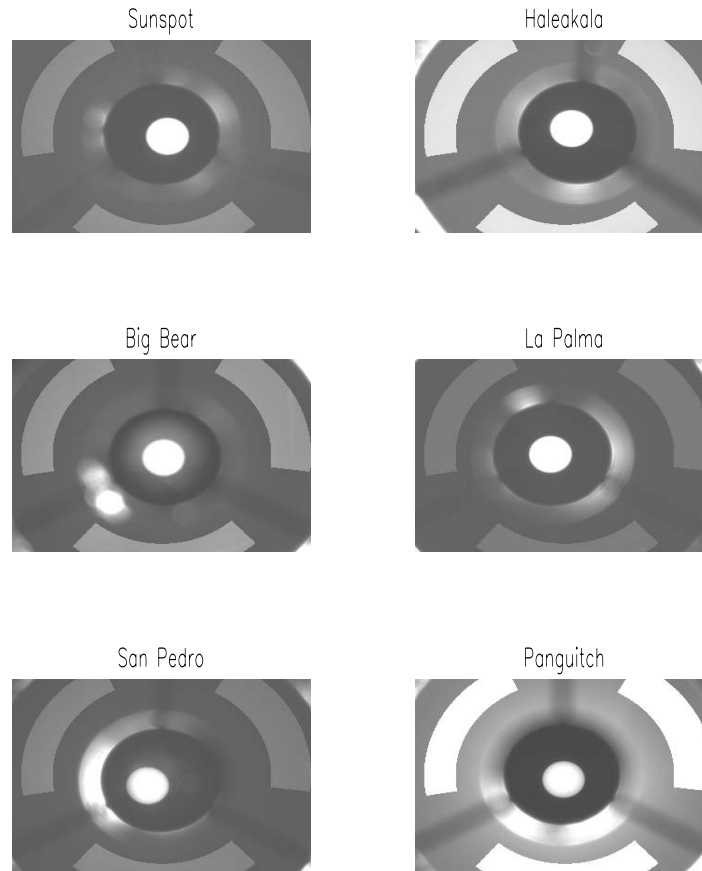


Figure 9.12: Sample images at 890 nm from all six sites, showing the valid sky pixel regions as three highlighted arcs. These pixel locations are identical in all images and are used for all wavelength channels as well. The inner, outer and azimuthal boundaries of these arcs were selected to avoid diffraction from the occulter edge, telescope tube front and the occulter support arm shadows. These obstacles are avoided at all wavelengths.

The SBM occulter developed problems with pinhole damage at each of the sites after they were originally deployed in 2003. The original occulter contained a single ND4 filter, and as it degraded this filter developed holes and transmitted significantly more light than 10^{-4} of the solar disk. At the three sites a first fix was made by replacing the ND4 filter with an absorptive filter from manufactured by CVI. This filter had a large transmission variation from 450nm to 940nm, and provided less than optimal data. The second replacement used a set of 2 ND2 filters, tilted to prevent reflection images, to replace the CVI filters. If one of these filters developed a pinhole it would result in only a 1% change in the transmitted solar disk intensity. The only true failure mode would be if both of the filters happened to develop pinholes which were precisely aligned; so far this problem has not been seen in the data.

The SBM instrument was designed to capture the solar disk image simultaneously with an image of the surrounding sky, by using these filters as occulter rather than an opaque occulting disk. This design

allowed a “local calibration” on each image, where the sky brightness was normalized to the central solar disk brightness. In this way changing sky conditions or changing instrumental properties would not affect the sky measurement, since the Sun and sky were measured simultaneously. This design was meant to mimic the successful visible sky photometer built by Evans and used at many observatories.

With the advent of the pinhole problem, it was determined that the local calibration technique could not be used, and that a “global calibration” technique should be used. Because the image of the sky taken by the SBM does not pass through the ND filters which suffered degradation, the sky images should be relatively unaffected by the pinhole problem. (A caveat is that the pinholes do introduce more stray light into the SBM, but this is found to be a minimal problem.) This global calibration technique relies on knowledge of the atmospheric extinction at each wavelength at the sites, the instrumental count rate at each wavelength, and it relies upon the assumption that the extinction and the instrumental gain do not vary significantly during the observing periods. Through examining the data with various tests these are found to be valid assumptions, within the error bars that are quoted. Thus this technique is used to reduce all of the SBM data from the three sites.

9.4.2 Details of the “Global Calibration” Technique

The idea is simple: use a mean extinction value and a constant instrumental response to predict the solar intensity for each image, instead of trying to measure the solar intensity from the central FOV which is corrupted with pinholes. If the solar disk center intensity at a particular time t and a particular wavelength is given by $I_{\lambda}(t) = I_{0,\lambda} e^{-\tau_{\lambda}(t)}$ then we can compute this value if we know τ_{λ} and $I_{0,\lambda}$ for a particular image. Since the optical depth τ_{λ} is given by the product of the extinction κ and the air mass M , we could compute the optical depth exactly if we knew both quantities. We can compute M for any given image, and if we assume that the extinction is equal to some median value measured with valid ND4 or 2ND2 data, then we would know enough to compute the optical depth.

The second assumption involves the zero air mass measured intensity $I_{0,\lambda}$. This can be represented as the product of the solar intensity, the filter (and optics) transmission, and the gain of the detector $I_{0,\lambda} = I_{Sun,\lambda} T_{\lambda} g_{\lambda}$. The solar intensity should vary only slightly as the Earth-Sun distance changes throughout the year; here we assume it is constant. If we assume that the instrumental parameters (the transmission and detector gain) are constant, then we can compute this quantity using the zero-intercept of the $\log(I)$ vs M relationship and use it to analyze the entire data set.

9.4.2.1 VALUES FOR EXTINCTION AND INSTRUMENTAL COUNT RATE

Figure 9.13 plots histograms of the instantaneous extinction measured in the May 2003 data ND4 data and also from all 2ND2 data the three test sites. Table 9.2 lists the median values taken from these distributions, with exception of the 2ND2 data from La Palma at 890nm. Here the computed median extinction is negative, due to problems with image drift and vignetting in the central FOV, and also due to the fact that only 20 days of 2ND2 data were collected at La Palma. The modal value of the extinction is listed in Table 9.2 in this case.

Table 9.2 – Measured median extinction (κ) values

Site – Date	450nm	530nm	890nm
Big Bear May 2003	0.25	0.19	0.11
May-Aug 2004	0.20	0.14	0.04
Haleakala May 2003	0.17	0.12	0.04
Mar-Aug 2004	0.17	0.11	0.04
La Palma May 2003	0.20	0.14	0.05
Jun-Aug 2004	0.16	0.09	0.06*

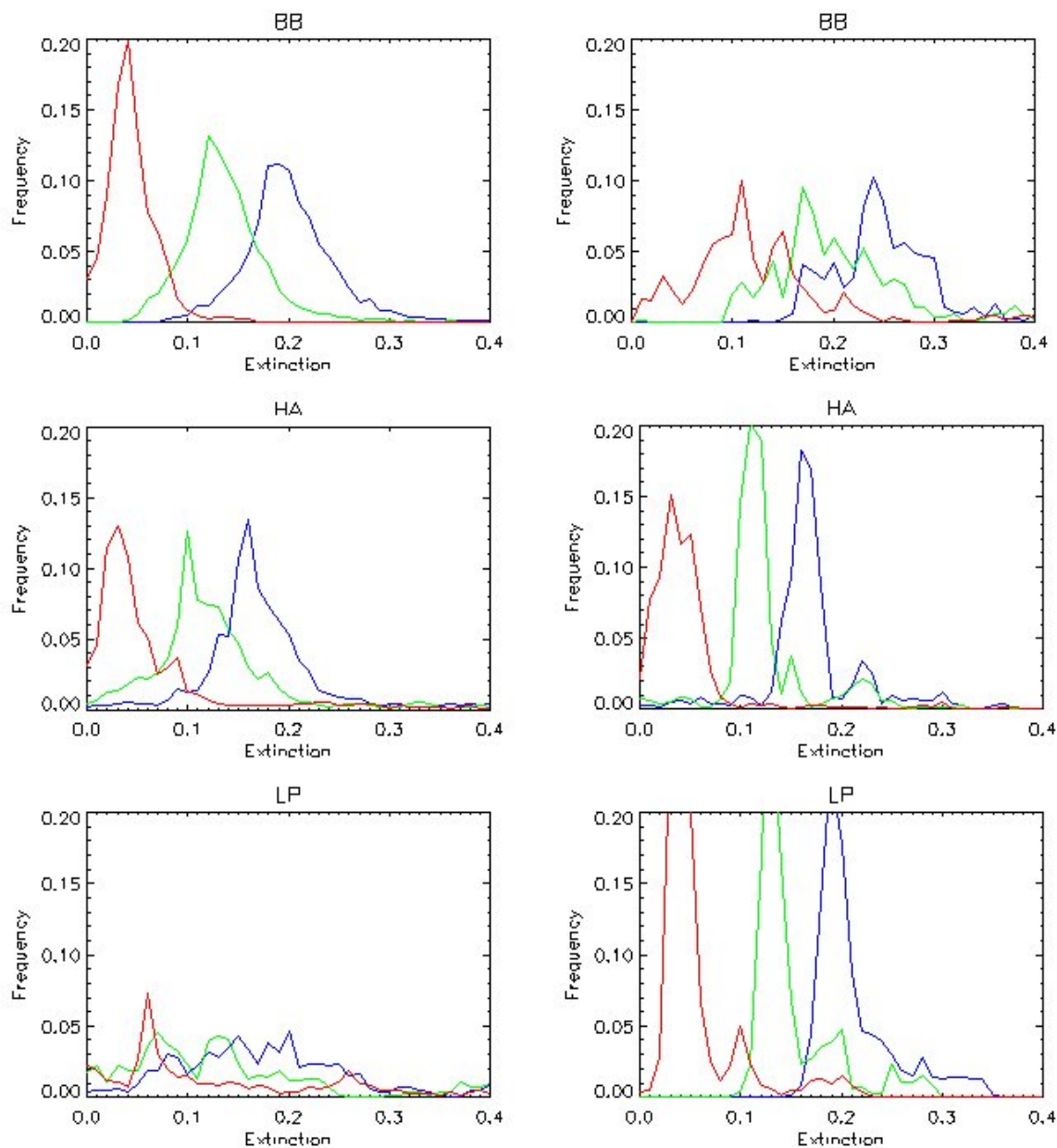


Figure 9.13. – Plotted are histograms of the measured extinctions at all three sites at three wavelengths for the May 2003 data with the ND4 filter (right column) and for all data taken from the site with the 2ND2 filter (left column). The medians of these distributions are listed in Table 9.2.

There is little variation seen between the 2003 and the 2004 extinction medians, and widths of about ± 0.05 are seen in the distributions for the extinction. The values used in the data analysis, and the associated measurement errors used in the error analysis are listed in Table 9.3.

Table 9.3. Values of extinction (κ) used in analysis

Site	450nm	530nm	890nm
Big Bear	0.23 \pm 0.05	0.17 \pm 0.05	0.07 \pm 0.05
Haleakala	0.17 \pm 0.05	0.12 \pm 0.05	0.04 \pm 0.05
La Palma	0.20 \pm 0.05	0.14 \pm 0.05	0.05 \pm 0.05

Table 9.4 shows the measured counts per second of the solar disk center for zero air mass at each wavelength for dates in May 2003 and for dates in 2004 when the 2ND2 was used. This is the coefficient $I_{0,\lambda}$ discussed earlier. In each case a linear fit is made to the observed log(solar intensity) as a function of air mass during the morning hours using air mass values between 1.0 and 4.0.

Table 9.4 – Measured instrumental count rate (ADU per sec / 10^8)

Site - Date	450nm	530nm	890nm
BBSO 15 May 2003	4.12	11.74	6.04
19 May 2003	3.83	10.14	5.75
24 May 2004	3.18	8.73	2.78
22 July 2004	3.27	9.05	2.79
04 Aug 2004	3.26	8.98	2.74
Haleakala 8 May 2003	5.32	13.1	3.69
15 May 2003	5.17	12.8	3.70
19 Mar 2004	3.54	8.81	2.38
08 Jun 2004	3.40	8.60	2.53
10 Aug 2004	3.48	8.99	2.69
La Palma 05 May 2003	6.20	12.85	3.58
26 May 2003	5.9	12.29	3.48
07 Jul 2004	3.19	6.50	1.43
03 Aug 2004	3.15	6.84	1.68
20 Aug 2004	3.15	7.40	2.20

The variations seen here are more troubling. It is most likely that they arise from an improper value for the transmission of the ND filter used in the occulter in each case. If the variation was due to a linear instrumental drift, then the measurements using the 2ND2 filter from Big Bear and Haleakala would show more variation during the 3 and 5 month periods over which they were collected. The measurements using a single occulter are internally consistent with no systematic time variability, so this points to the incorrect transmission value of the ND filter as the likely source of the variations.

The medians and standard deviations of these values were used in the data analysis; the values are listed in Table 9.5.

Table 9.5 – Instrumental count rate used in analysis (ADU per sec / 10^8)

Site	450nm	530nm	890nm
Big Bear	3.27+/-0.42	9.05+/-1.25	2.79+/-1.71
Haleakala	3.54 +/-0.97	8.99+/-2.28	2.69+/-0.65
La Palma	3.19+/-1.58	7.40+/-3.12	2.20+/-1.00

9.4.2.2 INTERNAL CONSISTENCY CHECK FOR GLOBAL CALIBRATION METHOD

How do these approximations affect the data? We can compare the sky brightness using these two techniques for the May 2003 data, where presumably the local calibration method is not affected by pinholes, and gives the “right” answer. Histograms for all three sites for all wavelengths are shown in Figure 9.14. The agreement with the BBSO data is very good, with no systematic differences between the local and global calibration methods. The Haleakala and La Palma data do show some systematic variations at low sky brightness, when the global calibration method appears to systematically increase the measured sky brightness from the value obtained with the local calibration method. This only seems important at sky brightness values less than about 10 millionths. This must reflect some correlation

between changing sky brightness and changing atmospheric extinction during excellent sky conditions that is not accounted for in the global calibration technique.

Apart from this deviation at the very best sky conditions, the differences between the two techniques are small, and the global calibration technique was used for the data analysis.

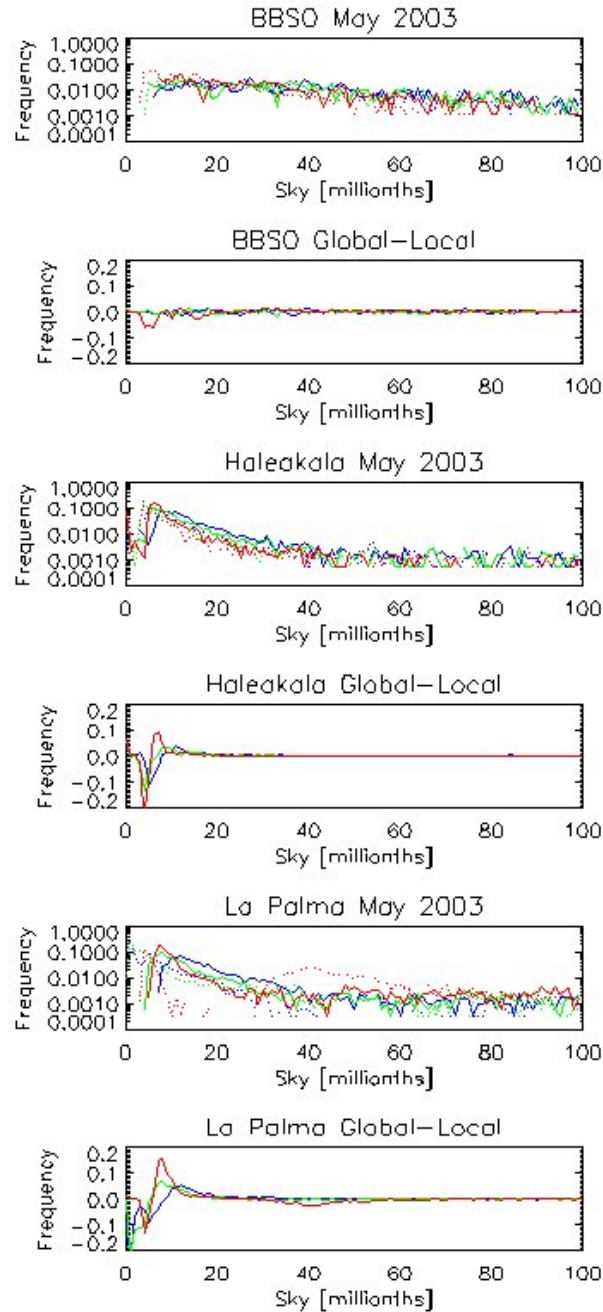


Figure 9.14: Histograms of the global (solid) and local (dashed) calibration technique sky brightness data for May 2003 from each site at all wavelengths. The second plot shows the difference, with the global-local histograms showing the differences between the techniques.

9.4.2.3 INSTRUMENTAL SCATTERED LIGHT

Measuring the instrumental scatter has proven to be the most difficult task involved in the data analysis of the SBM observations. The techniques for making this measurement require stable sky conditions; at Haleakala there seem to be several days of stable skies and the instrumental scattered light measurements taken there show the least scatter. At the other two sites however, sky conditions stable enough to make this measurement seem are difficult to find. It is likely that the instrumental scattered light changes with the use of different occulters, and this is suggested by the Haleakala data, but the measurements from the other sites have such a large inherent scatter that no systematic behavior is seen as the SBM occulters are changed.

The instrumental scatter for the SBM was derived by assuming that the sky brightness for any given wavelength (normalized by the solar intensity) follows $I_{\text{sky}}/I_{\text{sun}} = \Phi \kappa M + B$, where Φ is the atmospheric scattering function, κ is the extinction, M is the air mass and B is the instrumental scattered light. Knowing the air mass for each observation, a plot of normalized sky brightness versus air mass was made, the slope of which gives the sky brightness per air mass (see later discussion) but the intercept gives the instrumental scattered light. This value is calculated for several dates when ND4 and 2ND2 data was taken and the values are listed in Table 9.6 below.

The instrumental stray light must always be positive to have physical meaning, and so the negative values in Table 9.6 reflect the difficulty in making this measurement from the data. The color dependence of the instrumental stray light probably mostly depends on the wavelength properties of the internal paint used inside the SBM telescope tube and on the internal baffles.

Table 9.6. Values in millionths for the instrumental stray light for various dates

Site – Date	450nm	530nm	890nm
Big Bear 15 May 03	-3.45	-4.11	0.04
19 May 03	11.64	12.41	9.17
24 May 04	1.83	2.19	5.39
22 Jul 04	5.29	5.55	8.71
04 Aug 04	6.97	6.96	9.54
Haleakala 8 May 03	5.15	4.39	4.57
15 May 03	3.65	3.00	3.79
19 Mar 04	1.95	2.33	3.21
8 Jun 04	1.04	1.25	2.49
10 Aug 04	1.57	1.58	2.50
La Palma 5 May 03	-0.25	0.18	2.61
26 May 03	2.07	1.74	3.54
7 Jul 04	0.46	0.67	-0.09
3 Aug 04	-38	-25.5	-4.06
20 Aug 04	1.18	1.27	-0.20

The median values plus and minus the standard deviation of the measurements is shown in Table 9.7. In the discussion of the median sky conditions we describe another method to estimate the instrumental scattered light.

Table 9.7. – Median of instrumental scattered light values.

Site	450nm	530nm	890nm
Big Bear	5.29+/-5.66	5.55+/-3.87	8.71+/-4.01
Haleakala	1.95+/-1.70	2.33+/-1.25	3.21+/-0.89
La Palma	0.46+/-17.40	0.67+/-11.85	-0.06+/-2.97

Another approach to compute the instrumental scatter values has proved to be more successful; basically it takes the median of the many sky brightness measurements and then computes the fit, rather than taking the median of the fit coefficients. First, a set of days with good sky conditions are identified for each site, based on the daily minimum sky brightness values in the 890nm channel. Next, the sky brightness in the morning at each site from only those days is binned in air mass, in intervals of 0.1 air masses from 1.0 to 4.0. The median sky brightness in each bin is computed, and a linear fit is made to the median sky brightness as a function of air mass.

The results are shown in Table 9.8 below, where the values for the linear fit intercept are shown, along with the number of days used to compute the median sky brightness. All of the values lie within the large error bars listed in Table 9.7. The values computed for Haleakala all lie within 0.5 millionths of the values listed in Table 9.7. But unlike the values listed in Table 9.7, the instrumental scatter values computed with this technique are all positive, and when compared to the daily minimum sky brightness measured at the sites (see Figure 4 below) these instrumental scatter values lie below the majority of the sky brightness measurements as one would expect.

The instrumental scatter values at Big Bear are larger than the instrumental values at the other sites, except for the scatter at 890nm. This is the strangest result from this technique, and suggests a possible problem with the calculation of the instrumental scatter at Big Bear at this wavelength. The instrument scatter at La Palma at 450nm seems a little low, although it is within 1.5 millionths of the scatter at Haleakala.

Table 9.8. – Instrumental scatter values computed from median of dark sky morning data

Site	Days	450nm	530nm	890nm
Big Bear	86	6.27	3.00	1.27
Haleakala	104	2.28	1.90	3.61
La Palma	75	0.97	1.09	3.44

9.4.2.4 ERROR ANALYSIS

Each measurement of sky brightness includes the mean value of the sky within the valid observation window and a value of the standard deviation of the sky brightness within that window. This is treated as the error in the sky brightness measurement and referred to as σ_{SB} . Using standard error propagation techniques we can derive the error in the sky brightness measurement using the global calibration technique. The error depends on the error in the sky brightness measurement, σ_{SB} , the error in the extinction value for each site (taken as the width of the observed extinction distributions) σ_K , and the error in the instrumental count rate (taken as the standard deviation of five count rate measurements) σ_I .

9.4.3 Extrapolation to compute IRspec

The ATST Site Requirements document describes the goal sky brightness at a wavelength of 1075 nm and a radial height of 1.1 solar radii. This goal is stated as a sky brightness of less than 25 ± 10 millionths at a distance of 1.1 radii, with a radial coefficient less than 1.0. This goal is referred to as the “IRspec” for the sky brightness. Since the SBM instrument does not observe at 1075 nm or at 1.1 solar radii, the SBM

data must be extrapolated using the radial and wavelength coefficients γ and β and the measured sky brightness at 890nm.

Since the average distance for the SBM mean sky brightness is about $6 R_{\text{SUN}}$, the sky brightness at $1.1 R_{\text{SUN}}$ can be computed with $B_{1.1} = (5.45)^\gamma B_6$ where γ is the radial coefficient. Since the wavelength coefficient is computed as β the sky brightness at 1000 nm can be computed from the 890 nm brightness with $B_{1000} = (0.89)^\beta B_{890}$ and so the sky brightness at $1.1 R_{\text{SUN}}$ and 1000 nm can be computed as:

$$B_{1.1,1000} = (0.89)^\beta (5.45)^\gamma B_{6,890}$$

9.5 CLEAR TIME FRACTION

The fraction of time that the sky is clear at the sites is determined from the DC scintillometer data. This data, shown in Figure 9.15, displays the usual intensity variation that results from the varying atmospheric thickness as a function of zenith angle.

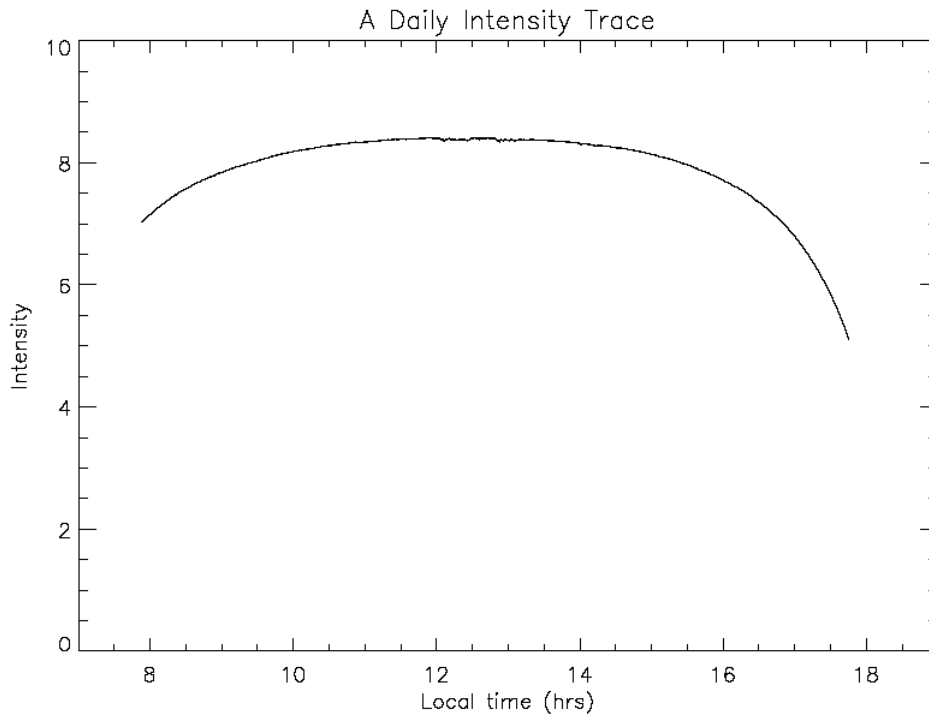


Figure 9.15: A trace of the intensity recorded during a clear day at Haleakala.

The existence of a cloud at a given observational time was operationally defined by the following steps:

- Within a five-minute period centered on the observation time, compute the temporal derivative of the intensity, dI/dt .
- Count the number of times that dI/dt changed sign within the five minute period.
- If the number of sign changes is greater than or equal to 2, define the observation as cloudy, otherwise it is clear.
- Move to the adjacent time sample and repeat

The clear time fraction was then computed as (the number of clear points) divided by (the number of clear plus the number of cloudy points). The results of this computation were found to be sensitive to the

choice of treatment of the SHABAR 8 and 10 flags discussed in section 9.2. Thus, we performed the analysis in two ways: designating all of the flags as cloudy, or designating all of the flags as instrumental down time. Assignment of the flagged points as cloudy significantly reduces the estimated clear time fraction, and impacts the results of the analysis discussed in section 9.8.

9.6 STATISTICS

The statistics of the various measured quantities were computed using standard techniques. The quantities are the mean, median, standard deviation, 10th percentile and 90th percentile values. Both relative and cumulative frequency distributions were obtained on a monthly and complete data set basis.

9.7 TIME BLOCK DISTRIBUTION

The distribution of time blocks was determined by applying a threshold to the data, locating all points above the threshold, and then essentially taking a derivative of the index of the surviving points. A jump in this derivative by a value greater than 1 indicates the end points of a contiguous block of time. The difference in these indices gives the length of the block. This data set can then be statistically analyzed.

9.8 CORRECTION FOR OBSERVING SCHEDULE AND WEATHER

A difficulty with our site-survey program is that the survey instruments measure the site quality with incomplete time coverage. Thus, the expectation value of the number of hours per day satisfying some condition (excellent seeing, for example) must be extrapolated from the number of hours actually observed. In the simplest case, one performs this extrapolation by writing

$$\langle G_a \rangle = G_{tot} / Nu_{tot}$$

where G_a is the estimated actual good hours per day, the angle brackets indicate expectation value, G_{tot} is the total number of good hours observed during the survey, N is the total number of days spanned by the survey, and u_{tot} is the survey instrument's fractional "up" time, that is, the hours that it was capable of taking observations, divided by the total possible hours of observations within the survey span. Here "capable of taking observations" means that the Sun was up (which for this purpose will be taken to mean that the local time is less than 7 hours before or after local solar noon), that the hardware was functional, and that the operators were present or otherwise able to take observations. Hardware failures and times when the instrument was shut for reasons other than bad weather count as "down" time. Times when the instrument was capable of observing, but because of bad weather it did not, count as "up" time and as "bad" conditions. Finally, one finds occasional observations yielding invalid results, for reasons that often are unknown. These invalid observations count as "down" time. For easier comparison with later results, it is helpful to define the total number of "up" hours in the survey as H_{tot} , with (by virtue of the definitions above)

$$H_{tot} \equiv 14Nu_{tot}$$

Then

$$\langle G_a \rangle = 14 \frac{G_{tot}}{H_{tot}} \quad (9.8.1)$$

This procedure is justifiable if there is no correlation between the times when conditions are good and the times when the survey instrument operates. In practice, we find (possibly) significant variations from site to site in the number of hours per day that the survey instruments have been operated, and also in the distribution of observations during the day. Since all sites show variation in the quality of observing conditions during the day, it is possible that a simple correction for fractional "up" time may give significantly incorrect results.

There follows a derivation of a simple correction to the extrapolation procedure in Eq. 9.8.1, taking into account the daily variation of seeing quality and of instrumental up time (averaged over the entire interval

studied in the survey) . This discussion will be described in terms of seeing quality, but the technique applies equally to other interesting observing conditions, such as coronal sky conditions.

First, some more definitions:

Let t be the hour angle of the Sun as seen from the site in question.

Let $g(t)$ be the probability that seeing at a particular site is “good” (whatever one chooses that to mean) at time t . Clouds and bad weather count as bad seeing. For purposes that follow, we will assume that, within a normalizing factor z , this function can be estimated by forming the following ratio, with the data binned by solar hour angle: (hours of observations with good seeing) divided by (hours of valid observations). Thus,

$$g(t)z \cong G_{tot}(t) / H_{val}(t), \quad (9.8.2)$$

where $G_{tot}(t)$ is as before, except binned according to t , and $H_{val}(t)$ is the total time during which valid observations were obtained, also binned by t . Eq. 9.8.2 amounts to assuming that the existing observations provide an adequate estimate of the shape of the daily variation of the probability of good seeing, but that the magnitude of g is uncertain within a factor z because the time sampling is incomplete on a day-to-day basis. Both G_{tot} and H_{val} must be smaller for a real system than for a perfect one. For a well-run survey, z will therefore be roughly unity, but it might be either larger or smaller.

Let u be the probability that the site is “up” at any time during a given day. Note that this not a function of time of day. An operational way to estimate u is to form the ratio (number of days on which some observations were obtained, plus number of days lost to bad weather) divided by (total days spanned in the survey). Alternatively, one might compute (number of days on which some observations were obtained) divided by (number of days on which the weather allowed some observations). In either case, the estimate of days that were or were not ruined by bad weather should be determined from some independent, e.g. GONG, data set.

Let $j(t)$ be the probability that, if the site was “up” on a given day, it is actually “up” at time t on that day. Thus, the total probability that the site is observing the Sun at any given time is $u_{tot}=uj(t)$. We estimate $j(t)$ by forming, for each bin of solar hour angle, the ratio (total number of observations in the data set, plus number of possible observations on bad-weather days) divided by (u times the number of possible observations in the time span covered by the data set).

What we want to know is: how many hours of good seeing are available per day (on average). Given the definitions, this is

$$\langle G_a \rangle = \int_{-7}^{+7} g(t) dt \equiv 14 \overline{g}. \quad (9.8.3)$$

Notice that we cannot immediately evaluate $\langle G_a \rangle$ by simply integrating our operational estimate of $g(t)z$, because the latter differs from the true $g(t)$ by the unknown normalizing factor z .

What we have measured is the actual number of good seeing hours per day during the times when the site was “up”:

$$G_{tot} = Nu \int_{-7}^{+7} g(t) j(t) dt \quad (9.8.4)$$

We can also measure the average number of “up” hours per day:

$$H_{tot} = Nu \int_{-7}^{+7} j(t) dt \equiv 14Nu \overline{j}. \quad (9.8.5)$$

Now write

$$g = \bar{g} + g'(t), \quad (9.8.6)$$

where $\int_{-7}^{+7} g'(t) dt = 0$, and in a similar fashion,

$$j = \bar{j} + j'(t). \quad (9.8.7)$$

That is, we break g and j into the sum of their mean values and the variation around the mean. Then expand out Eq. 9.8.4 to get

$$\begin{aligned} G_{tot} &= Nu \int_{-7}^{+7} [\bar{g} + g'(t)] [\bar{j} + j'(t)] dt \\ &= 14Nu (\bar{g}\bar{j} + \langle g'j' \rangle), \end{aligned} \quad (9.8.8)$$

where $\langle g'j' \rangle = \frac{1}{14} \int_{-7}^{+7} g'(t) j'(t) dt$ and the cross-terms vanish because g' and j' give zero when integrated onto a constant.

The number of good-seeing hours is then

$$\begin{aligned} 14 \frac{G_{tot}}{H_{tot}} &= 14(1/j') (\bar{g}\bar{j} + \langle g'j' \rangle) \\ &= 14\bar{g} \left(1 + \frac{\langle g'j' \rangle}{\bar{g}\bar{j}} \right) \end{aligned} \quad (9.8.9)$$

So, by comparison with Eq. 9.8.3,

$$\langle G_a \rangle = 14 \frac{G_{tot}}{H_{tot}} \left(1 + \frac{\langle g'j' \rangle}{\bar{g}\bar{j}} \right)^{-1}. \quad (9.8.10)$$

Now notice that if we replace $g(t)$ in Eq. 9.8.6 with our operationally defined $g(t)z$, then

$$g(t)z = \bar{g}z + g'z \quad (9.8.11)$$

If we use the operationally defined $g(t)z$ in Eq. 9.8.10, the unknown factor z then cancels in the correction term $\langle g'j' \rangle / (\bar{g}\bar{j})$. Notice that u (the site fractional up time) also drops out. This is so because we have implicitly assumed that the days when the site is “up” are uncorrelated with the days when the seeing is good. Thus, all of the things on the right hand side of Eq. 9.8.10 can be estimated from the seeing and site operation statistics that are available. We use $\langle G_a \rangle$, estimated in this fashion, as our measure of the likely amount of good seeing at each site.

10. RESULTS

10.1 DATA COVERAGE

Table 10.1 summarizes the seeing data included in this report.

Table 10.1 – Data coverage

Site	Start Date	End Date	Days Spanned	Days Closed for Weather	Valid Data points
Big Bear	18 Jul 2002	30 Aug 2004	774	40	820434
Haleakala	6 Aug 2002	30 Aug 2004	755	60	713678
La Palma	28 Sep 2002	30 Aug 2004	702	60	718370

10.2 SEEING

We present here the current results for the analysis that combines the SHABAR and S-DIMM data. Figure 10.1 shows the median and average value of r_0 as a function of height above the ground for the sites. All valid estimates of r_0 have been included in these curves.

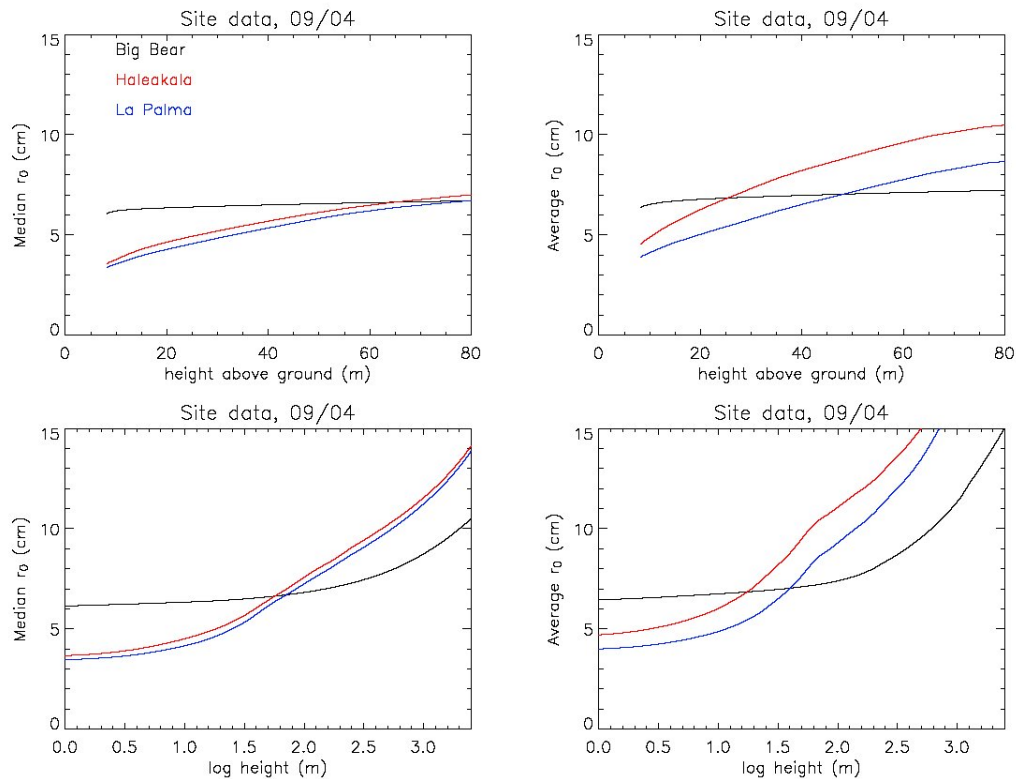


Figure 10.1 – The median and average values of r_0 as a function of height above the ground estimated from the fit to the combined SHABAR/S-DIMM data. These curves include all valid estimates for each site. The curves are shown with a logarithmic height scale in the bottom panels, and on a linear height scale near the ground in the top panels. Results are from the IAC analysis.

The detailed seeing results for all six sites are contained in Appendix 3.11. These appendices show the variation of r_0 with season, time of day, wind speed and wind direction. Some of the features of these plots for the top group of sites are:

- Big Bear: The seeing is better in the summer and fall, and in the early morning. It is poor when the wind blows from the north, the landward side of the site. It is best when the wind is onshore, from the south or from the west. The seeing deteriorates when the wind speed is large.
- Haleakala: The seeing is best in the winter months, and early in the morning. It is best when the wind is from the south or blowing strongly.

- La Palma: The seeing is best in the summer and early in the morning. It is best when the wind comes from the north, but there is little dependence of the seeing on wind speed.

One of the strengths of the SHABAR+S-DIMM analysis is that it provides an estimate of the structure function, $C_n^2(h)$. Figure 10.2 shows the median and average values of $\log C_n^2(h)$ for all valid estimates.

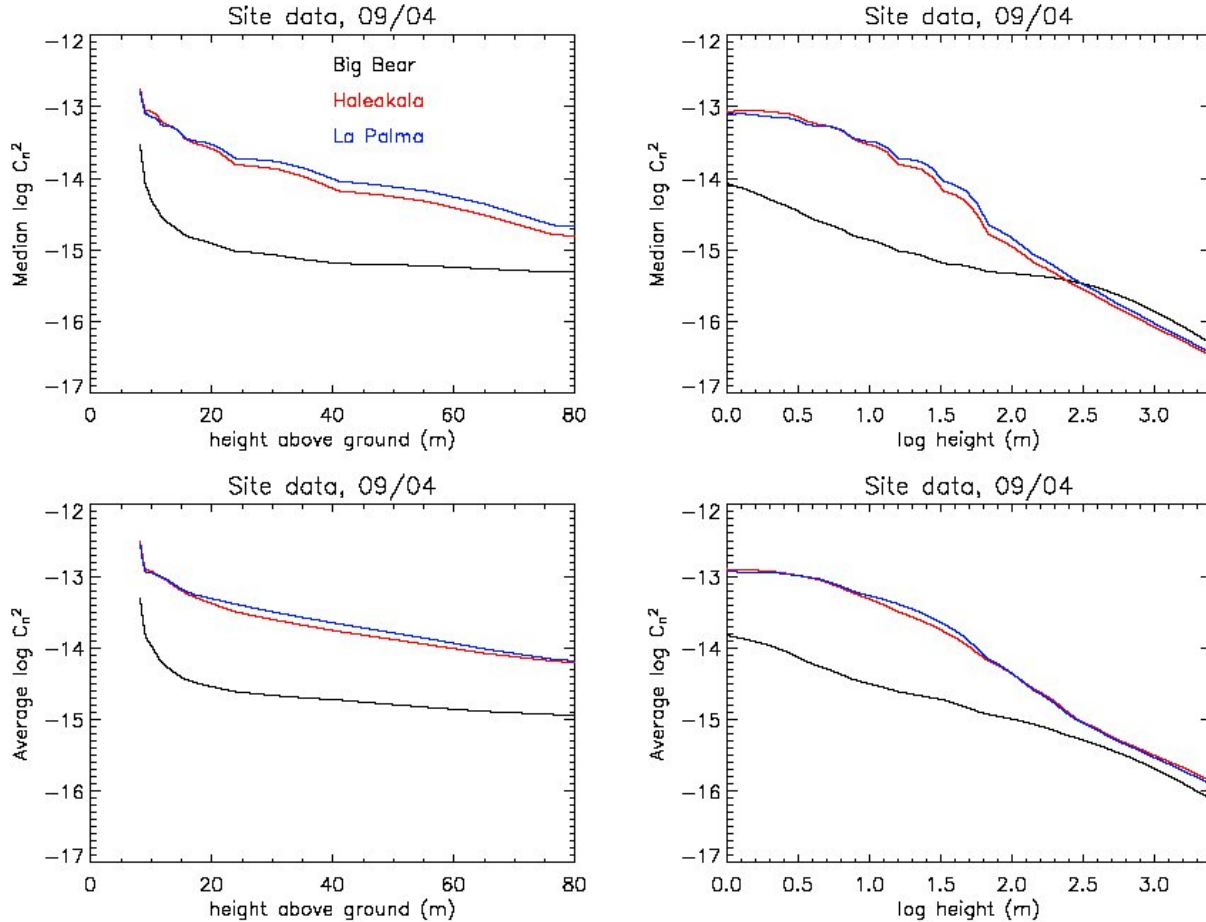


Figure 10.2 – The median and average $\log C_n^2(h)$ for all valid estimates from the IAC method.

Figure 10.2 shows the absence of a ground layer at the lake site (Big Bear), which is present at the other two sites without lakes. It also suggests that the high altitude seeing is better for the two ocean islands than for the continental lake. Results are from the IAC analysis.

Figures 10.3 and 10.4 show the cumulative distribution of the measurements of r_0 obtained from the S-DIMM (Figure 10.3), and from the IAC analysis of the combined S-DIMM and SHABAR measurements at four heights (Figure 10.4). A comparison of these distributions determined from the two analyses (IAC and HAO) is shown in Figure 9.3.

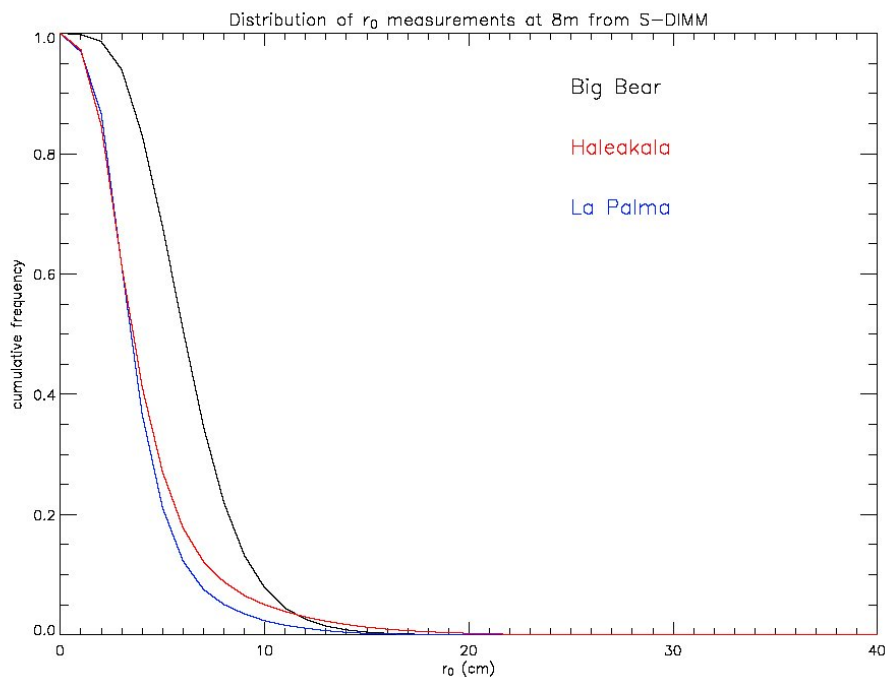


Figure 10.3: The cumulative frequency distribution of the r_0 measurements from the S-DIMM at a height of 8 m above the ground at the three sites.

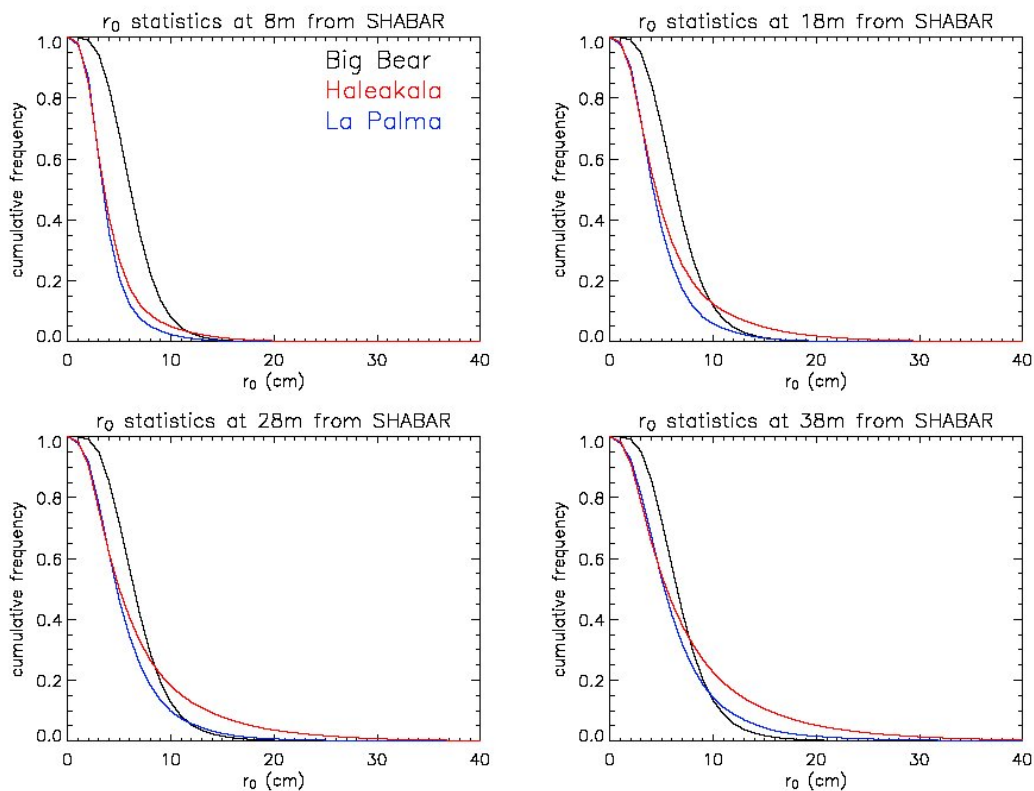


Figure 10.4: The cumulative frequency distributions of r_0 obtained from the IAC analysis of the combined S-DIMM and SHABAR data at four heights of 8, 18, 28, and 38 m above the ground.

10.2.1 Seeing Time Distribution

We have applied the correction for observing practices discussed in section 9.8 to the results of the seeing analysis. The results of the analysis are dependent on the way the clear time fraction is computed. Thus, we present in this section the results of two choices of approaches:

- Case 1: With instrumental flags considered as cloudy points
- Case 2: With instrumental flags considered as down time points

The two cases produce different observational coverage patterns for the sites. These are shown in Figures 10.6 to 10.8. The observing probability function $j(t)$, discussed in Section 9.8, is shown in Figure 10.5. The seeing probability functions, $g(t)$, are shown in Figures 10.9 and 10.10 for the good ($r_0 > 7$ cm) and the excellent ($r_0 > 12$ cm) cases. Note that these functions treat bad weather as observations with $r_0 = 0$ and, for Big Bear, go to zero at high absolute hour angles. This is due to the small number of observations taken during those times, which then produces a probability dominated by the days closed but marked cloudy on the log sheets. In addition, the latitude of the site affects these plots and Figure 10.5 since the higher-latitude sites sample the extreme hour angles less frequently during the year. Figure 10.11 shows an example of the probability of observing r_0 above a threshold of 5 cm, ignoring clouds.

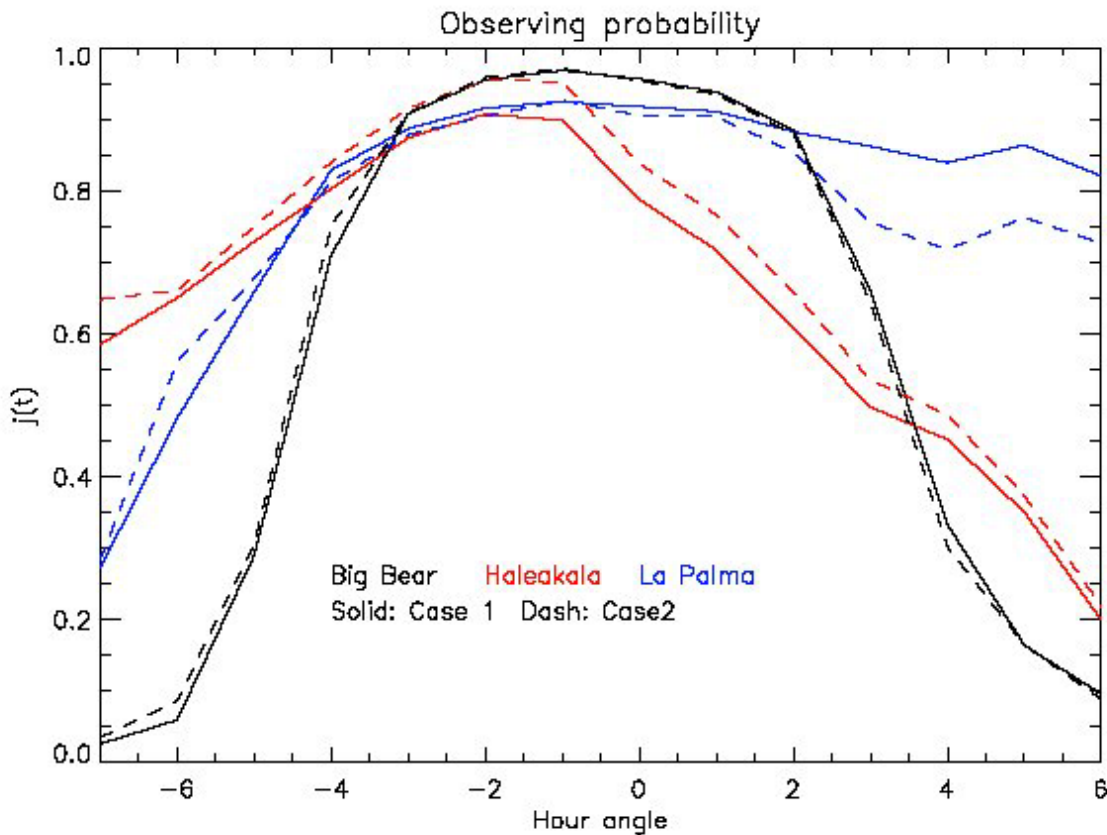


Figure 10.5: The observing probability, $j(t)$, as a function of hour angle for the three sites and the two cases of clear time fraction computation.

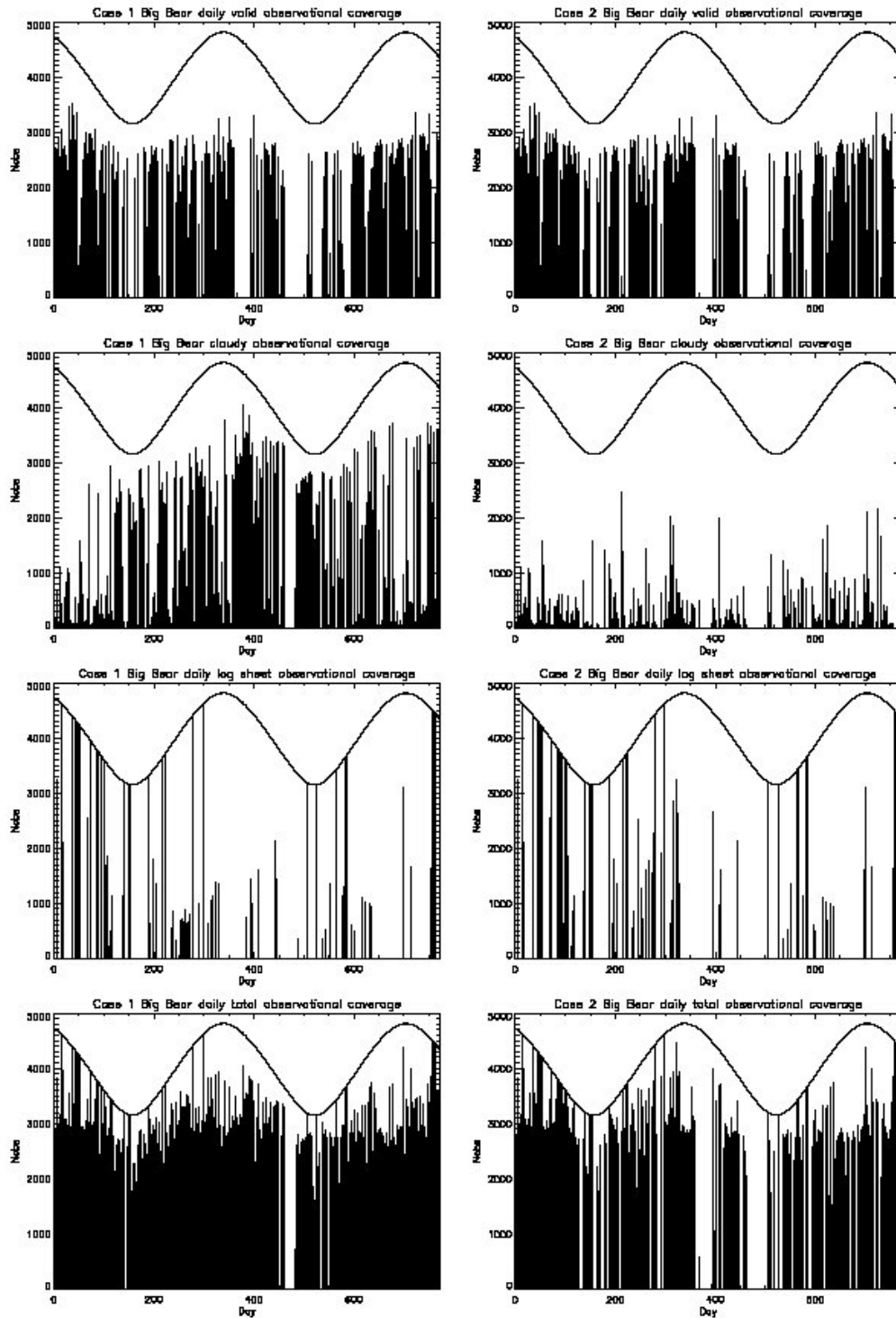


Figure 10.6: The observational coverage at Big Bear. Top Row: Daily number of valid seeing observations. Second row: Daily number of cloudy observations. Third row: Daily number of observations when instrument was closed and the log sheets indicated bad weather. Bottom row: total of the other three rows. Left column: Case 1 (flagged points indicate clouds), right column: Case 2 (flagged points indicate instrument down).

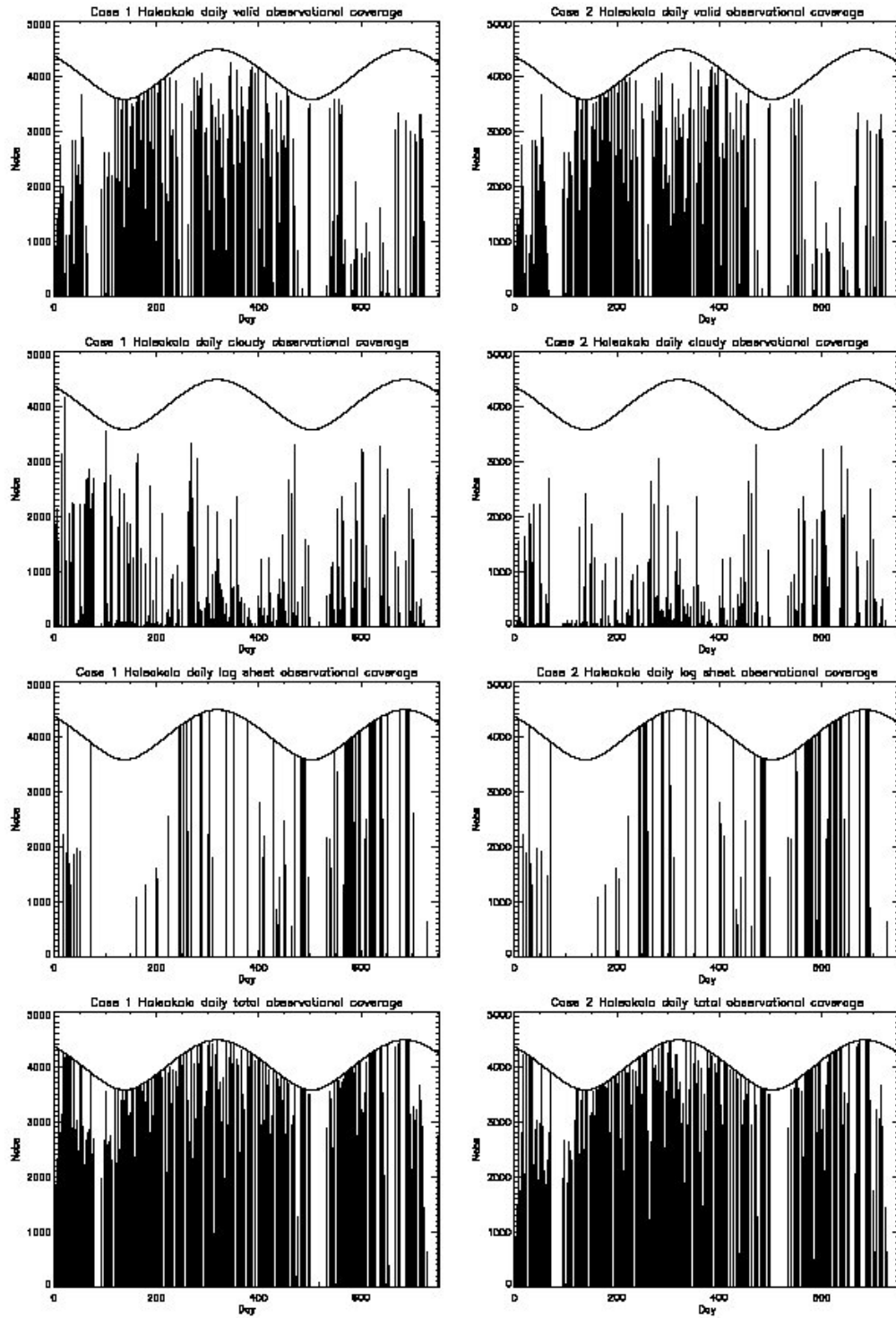


Figure 10.7: As Figure 10.6, but for Haleakala

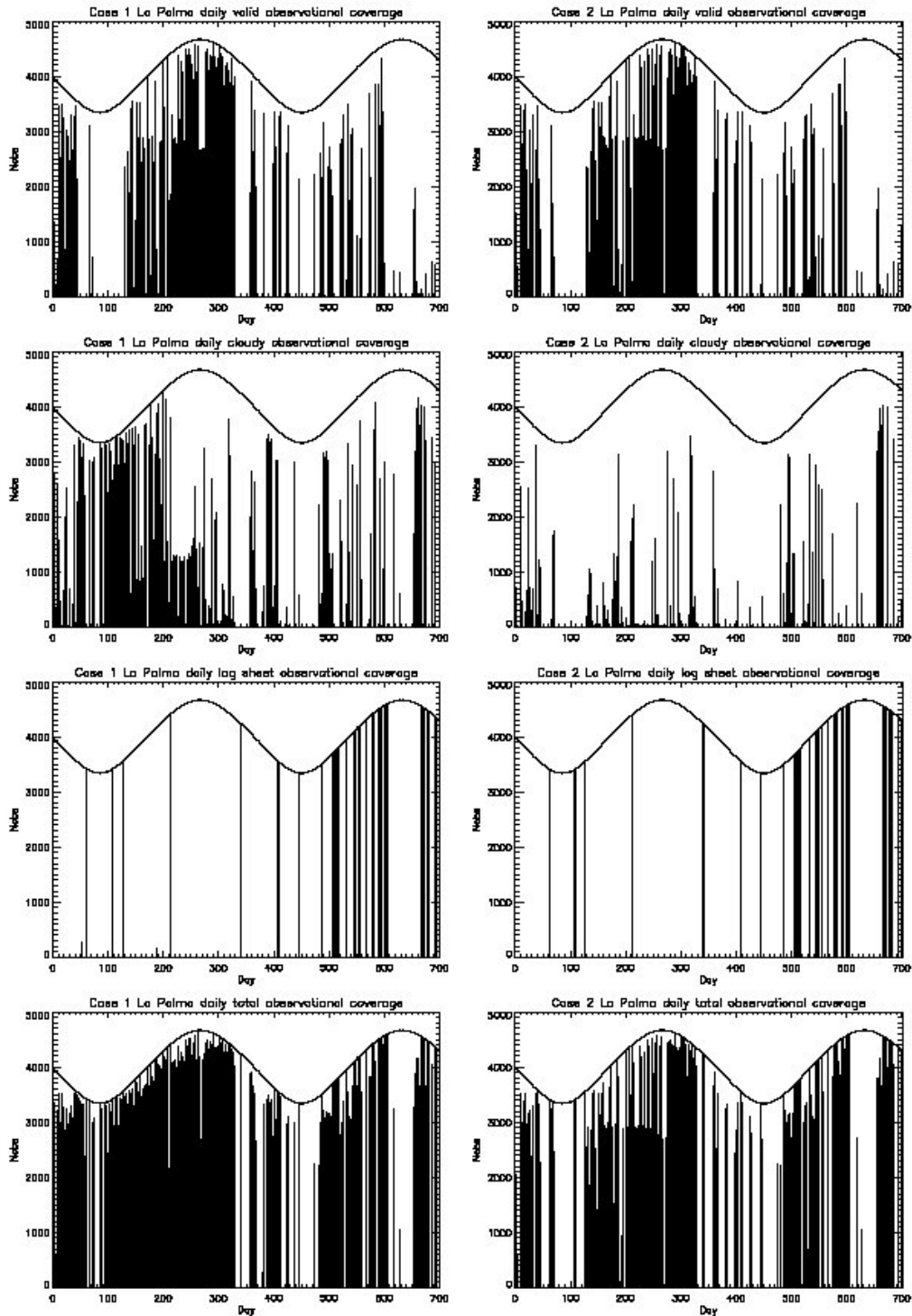


Figure 10.8: As Figure 10.6, but for La Palma

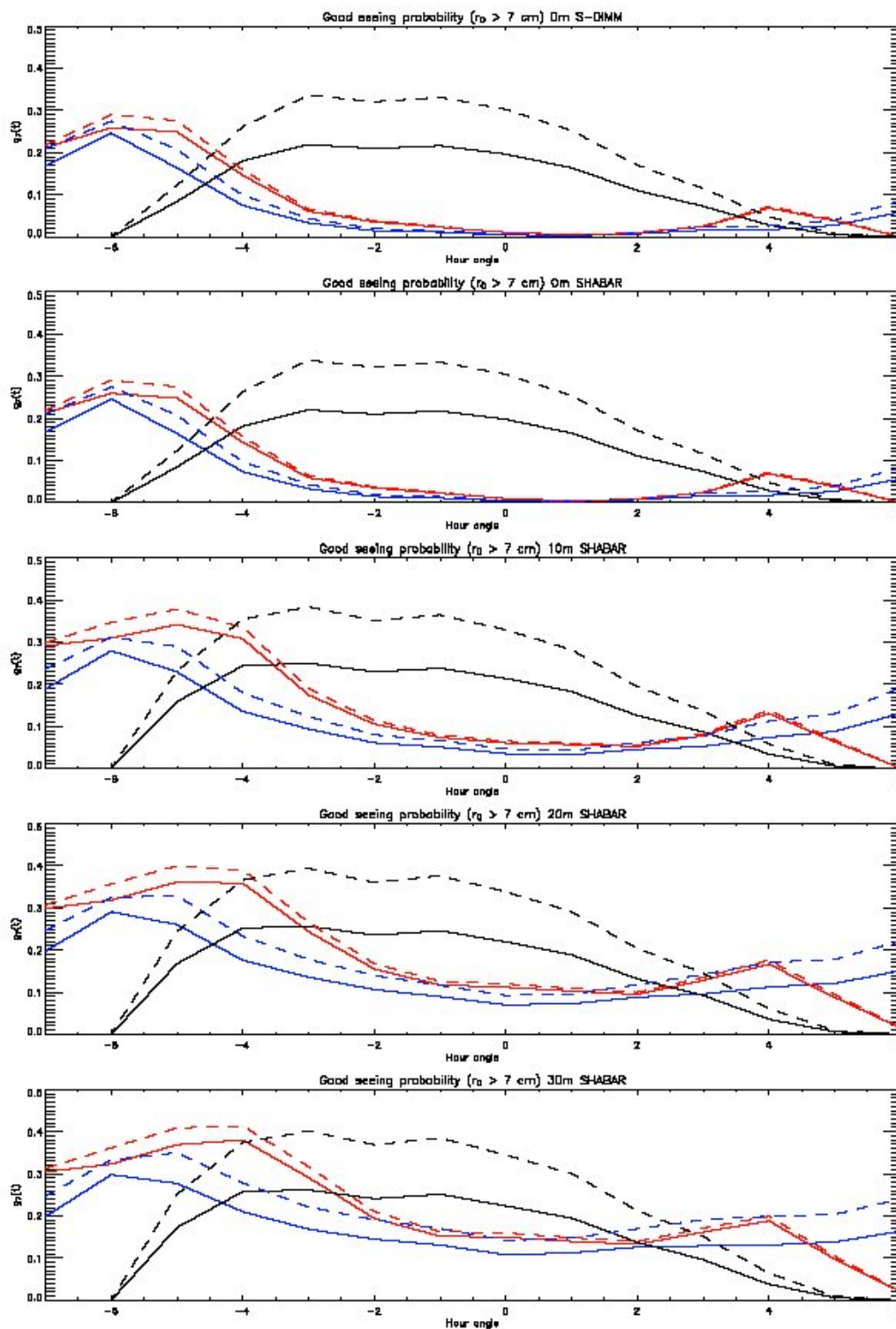


Figure 10.9: The probability $g(t)$ of obtaining good seeing ($r_0 > 7$ cm) as a function of hour angle. Black: Big Bear; red: Haleakala; blue: La Palma. Solid line: Case 1; dashed line: Case2. Top to bottom: S-DIMM data; SHABAR at 8 m above the ground; 18 m; 28; and 38 m. These plots count bad weather as $r_0=0$. The apparent decrease of $g(t)$ at Big Bear at the extreme hour angles is due to the small number of observations at those times which results in the statistics being dominated by cloudy days on which the instrument was shut down.

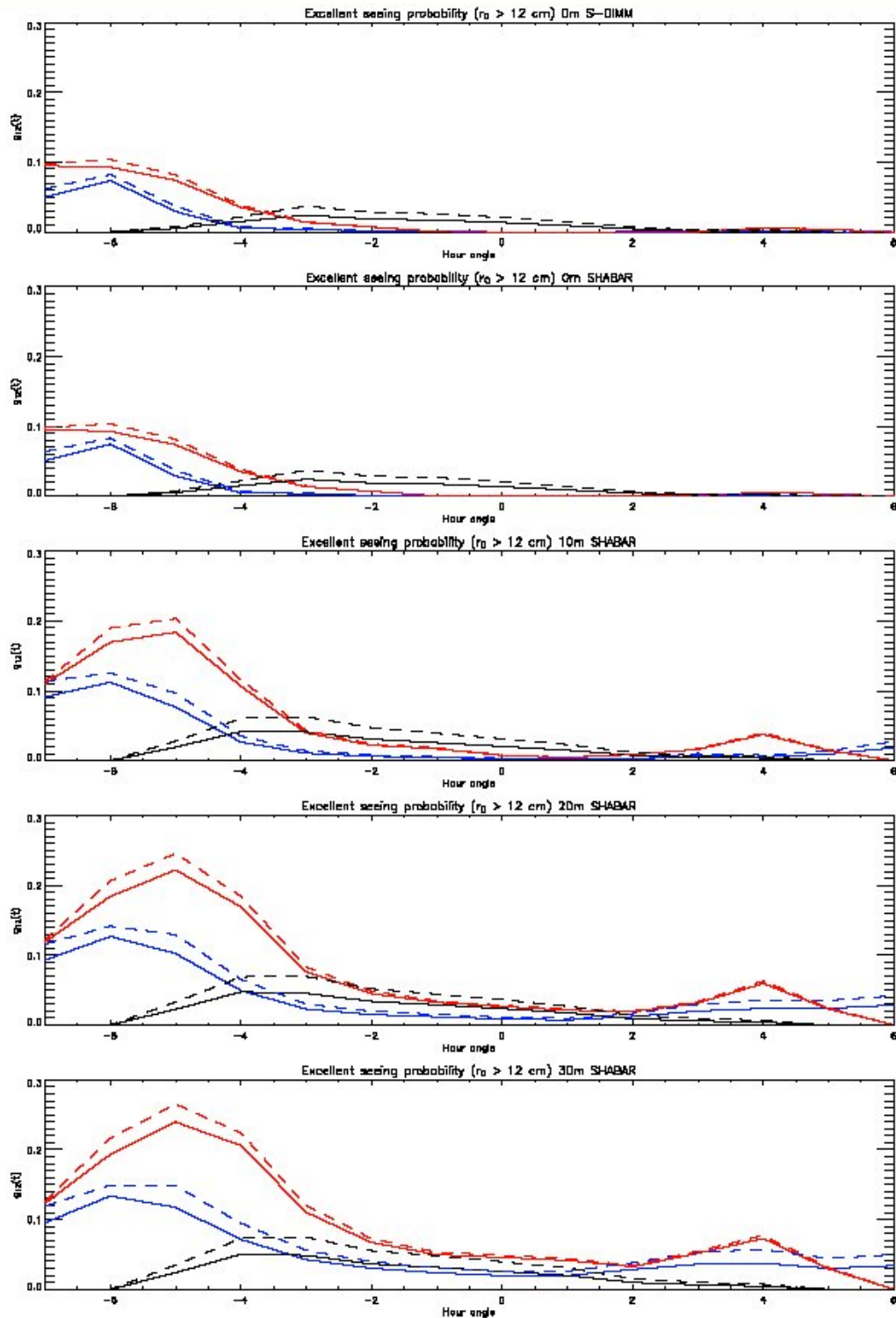


Figure 10.10: As figure 10.9, but for excellent seeing ($r_0 > 12$ cm).

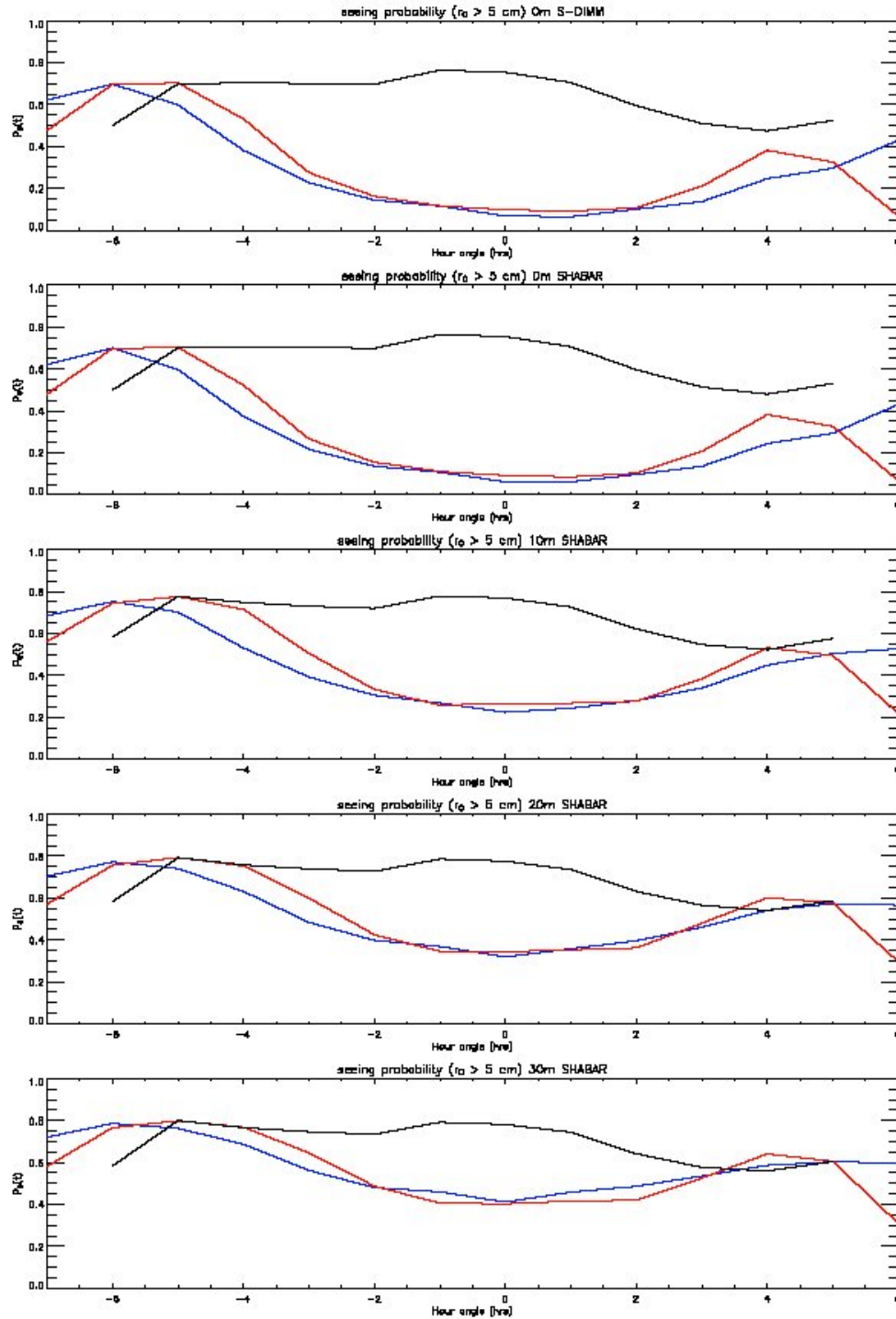


Figure 10.11: The probability functions for $r_0 > 5$ cm as a function of hour angle and height at the sites. These functions, unlike the functions $g(t)$ shown in figures 10.9 and 10.10, do not include bad weather and so do not exhibit end effects at Big Bear.

Tables 10.2 through 10.4 show the results for Case 1, with instrumental flags considered as cloudy points. These tables show the raw observed and corrected annual hours for good seeing ($r_0 > 7$ cm) and excellent seeing ($r_0 > 12$ cm) as derived from the S-DIMM observations, and the IAC analysis of the combined S-DIMM/SHABAR measurements at heights of 8, 18, 28, and 38 m above the ground. The table also

contains the derived correction factor as defined by Eq. 9.8.10. Lastly, the table contains the observed and corrected annual values of the number of 2-hour time blocks of good and excellent seeing. These numbers are corrected by the same factors used for the individual hour counts. Tables 10.5 through 10.7 show the results for Case 2, with the flags treated as instrumental down time.

Table 10.2 CASE 1 Results for Big Bear

Total Hours Observed: 4903 Clear Weather Fraction: 0.465							
Good Seeing ($r_0 > 7\text{cm}$)	Raw observed hours	Naïve annual hours	Correction factor	Corrected Annual hours	Raw N 2-hr blocks	Naïve annual N 2-hr blocks	Corrected Annual N 2-hr blocks
S-DIMM 8m	802	836	1.493	560	59	61	40
SHABAR 8m	808	842	1.493	564	47	49	32
SHABAR 18m	926	965	1.447	666	65	68	47
SHABAR 28m	957	997	1.444	690	75	78	54
SHABAR 38m	982	1023	1.443	708	76	79	55
Excellent Seeing ($r_0 > 12\text{cm}$)	Raw observed hours	Naïve annual hours	Correction factor	Corrected Annual hours	Raw N 2-hr blocks	Naïve annual N 2-hr blocks	Corrected Annual N 2-hr blocks
S-DIMM 8m	61	63	1.522	42	1	1	1
SHABAR 8m	62	64	1.520	42	0	0	0
SHABAR 18m	109	114	1.440	79	1	1	1
SHABAR 28m	123	129	1.435	90	1	1	1
SHABAR 38m	134	139	1.438	97	1	1	1

Table 10.3 CASE 1 Results for Haleakala

Total Hours Observed: 3451 Clear Weather Fraction: 0.574							
Good Seeing ($r_0 > 7\text{cm}$)	Raw observed hours	Naïve annual hours	Correction factor	Corrected Annual hours	Raw N 2-hr blocks	Naïve annual N 2-hr blocks	Corrected Annual N 2-hr blocks
S-DIMM 8m	253	374	1.044	358	10	15	14
SHABAR 8m	250	370	1.043	355	10	15	14
SHABAR 18m	514	762	1.075	709	31	46	43
SHABAR 28m	670	992	1.077	921	55	81	75
SHABAR 38m	782	1158	1.082	1071	72	107	97
Excellent Seeing ($r_0 > 12\text{cm}$)	Raw observed hours	Naïve annual hours	Correction factor	Corrected Annual hours	Raw N 2-hr blocks	Naïve annual N 2-hr blocks	Corrected Annual N 2-hr blocks
S-DIMM 8m	62	92	1.042	88	1	1	1
SHABAR 8m	62	92	1.041	88	1	1	1
SHABAR 18m	176	261	1.066	245	2	3	3
SHABAR 28m	269	398	1.084	367	7	10	10
SHABAR 38m	348	515	1.094	471	12	18	16

Table 10.4 CASE 1 Results for La Palma

Total Hours Observed: 4196 Clear Weather Fraction: 0.475							
Good Seeing ($r_0 > 7\text{cm}$)	Raw observed hours	Naïve annual hours	Correction factor	Corrected Annual hours	Raw N 2-hr blocks	Naïve annual N 2-hr blocks	Corrected Annual N 2-hr blocks
S-DIMM 8m	153	186	0.747	249	6	7	12
SHABAR 8m	152	185	0.745	249	7	9	14
SHABAR 18m	348	423	0.868	487	20	24	34
SHABAR 28m	509	620	0.916	677	31	38	47
SHABAR 38m	645	785	0.945	831	44	54	62
Excellent Seeing ($r_0 > 12\text{cm}$)	Raw observed hours	Naïve annual hours	Correction factor	Corrected Annual hours	Raw N 2-hr blocks	Naïve annual N 2-hr blocks	Corrected Annual N 2-hr blocks
S-DIMM 8m	22	26	0.604	44	0	0	0
SHABAR 8m	22	27	0.601	45	0	0	0
SHABAR 18m	64	78	0.709	110	1	1	2
SHABAR 28m	116	141	0.802	176	2	2	3
SHABAR 38m	178	217	0.864	251	2	2	3

Table 10.5 CASE 2 Results for Big Bear

Total Hours Observed: 3201 Clear Weather Fraction: 0.712							
Good Seeing ($r_0 > 7\text{cm}$)	Raw observed hours	Naïve annual hours	Correction factor	Corrected Annual hours	Raw N 2-hr blocks	Naïve annual N 2-hr blocks	Corrected Annual N 2-hr blocks
S-DIMM 8m	802	1281	1.496	856	59	94	62
SHABAR 8m	808	1290	1.496	863	47	75	49
SHABAR 18m	926	1478	1.454	1017	65	104	71
SHABAR 28m	957	1528	1.451	1053	75	120	83
SHABAR 38m	982	1567	1.450	1081	76	121	84
Excellent Seeing ($r_0 > 12\text{cm}$)	Raw observed hours	Naïve annual hours	Correction factor	Corrected Annual hours	Raw N 2-hr blocks	Naïve annual N 2-hr blocks	Corrected Annual N 2-hr blocks
S-DIMM 8m	61	97	1.527	64	1	2	1
SHABAR 8m	62	99	1.525	65	0	0	0
SHABAR 18m	109	174	1.454	120	1	2	1
SHABAR 28m	123	197	1.449	136	1	2	1
SHABAR 38m	134	213	1.452	147	1	2	1

Table 10.6 CASE 2 Results for Haleakala

Total Hours Observed: 3203 Clear Weather Fraction: 0.619							
Good Seeing ($r_0 > 7\text{cm}$)	Raw observed hours	Naïve annual hours	Correction factor	Corrected Annual hours	Raw N 2-hr blocks	Naïve annual N 2-hr blocks	Corrected Annual N 2-hr blocks
S-DIMM 8m	253	403	1.035	389	10	16	15
SHABAR 8m	250	399	1.034	386	10	16	15
SHABAR 18m	514	820	1.068	768	31	49	47
SHABAR 28m	670	1069	1.073	997	55	88	82
SHABAR 38m	782	1247	1.978	1157	72	115	106
Excellent Seeing ($r_0 > 12\text{cm}$)	Raw observed hours	Naïve annual hours	Correction factor	Corrected Annual hours	Raw N 2-hr blocks	Naïve annual N 2-hr blocks	Corrected Annual N 2-hr blocks
S-DIMM 8m	62	99	1.033	96	1	2	2
SHABAR 8m	62	99	1.033	96	1	2	2
SHABAR 18m	176	281	1.053	267	2	3	3
SHABAR 28m	269	428	1.073	399	7	11	10
SHABAR 38m	348	555	1.085	511	12	19	18

Table 10.7 CASE 2 Results for La Palma

Total Hours Observed: 3123 Clear Weather Fraction: 0.639							
Good Seeing ($r_0 > 7\text{cm}$)	Raw observed hours	Naïve annual hours	Correction factor	Corrected Annual hours	Raw N 2-hr blocks	Naïve annual N 2-hr blocks	Corrected Annual N 2-hr blocks
S-DIMM 8m	153	250	0.801	313	6	10	14
SHABAR 8m	152	249	0.799	311	7	11	17
SHABAR 18m	348	569	0.900	632	20	33	43
SHABAR 28m	509	833	0.940	887	31	51	60
SHABAR 38m	645	1055	0.965	1093	44	72	80
Excellent Seeing ($r_0 > 12\text{cm}$)	Raw observed hours	Naïve annual hours	Correction factor	Corrected Annual hours	Raw N 2-hr blocks	Naïve annual N 2-hr blocks	Corrected Annual N 2-hr blocks
S-DIMM 8m	22	36	0.679	53	0	0	0
SHABAR 8m	22	36	0.676	54	0	0	0
SHABAR 18m	64	104	0.767	136	1	2	2
SHABAR 28m	116	190	0.845	225	2	3	4
SHABAR 38m	178	292	0.899	324	2	3	4

Figures 10.12 and 10.13 show the average and median values of r_0 as a function of hour angle, site, and height above the ground. These values do not depend on the choice of clear time fraction computation. In addition, since these numbers are derived from the valid seeing observations alone, they are free of the end effects seen in Figures 10.9 and 10.10.

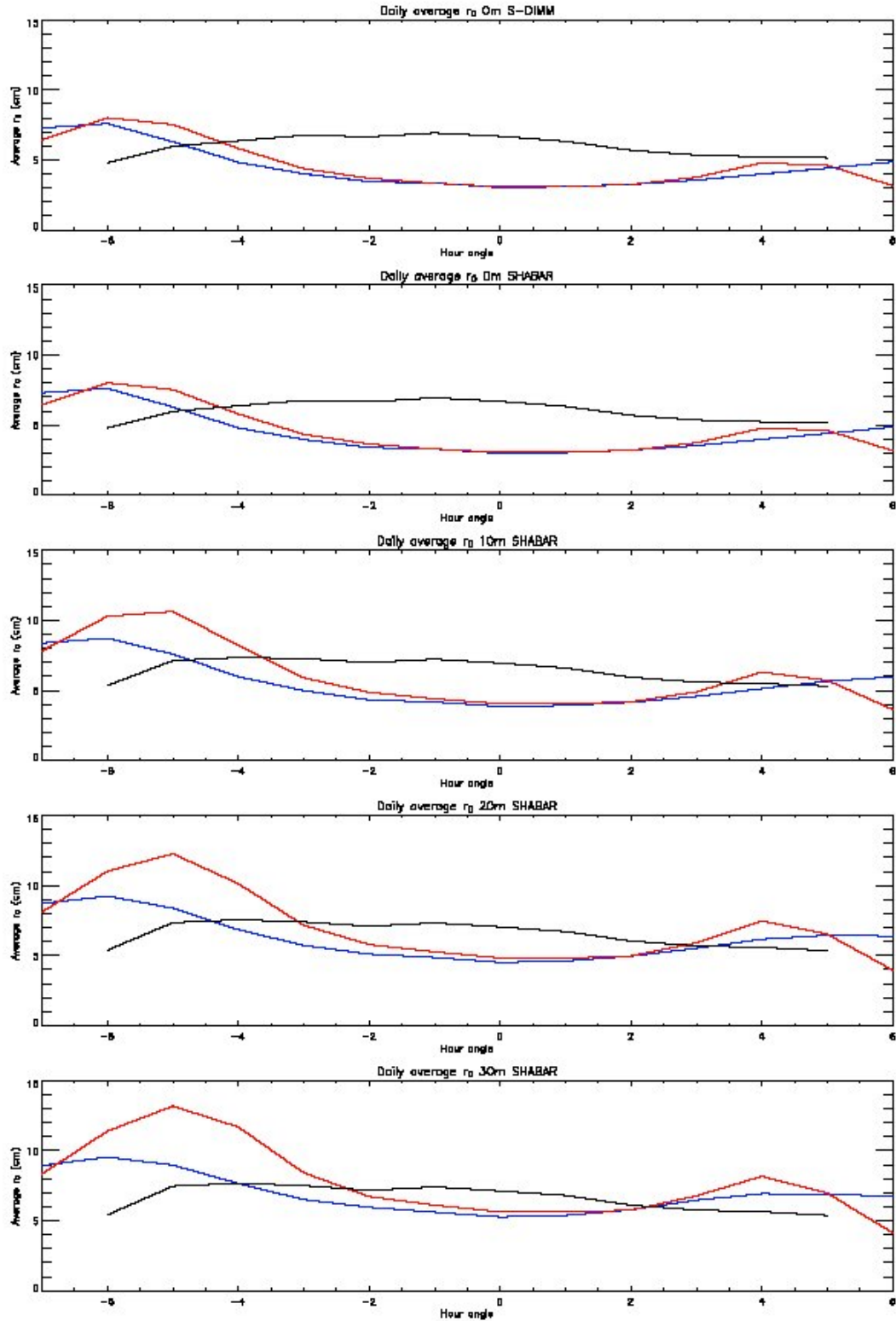


Figure 10.12: The average value of the valid measurements of r_0 as a function of hour angle. Black: Big Bear; red: Haleakala, blue: La Palma. Top to bottom: S-DIMM data; SHABAR at 8 m above the ground; 18 m; 28; and 38 m.

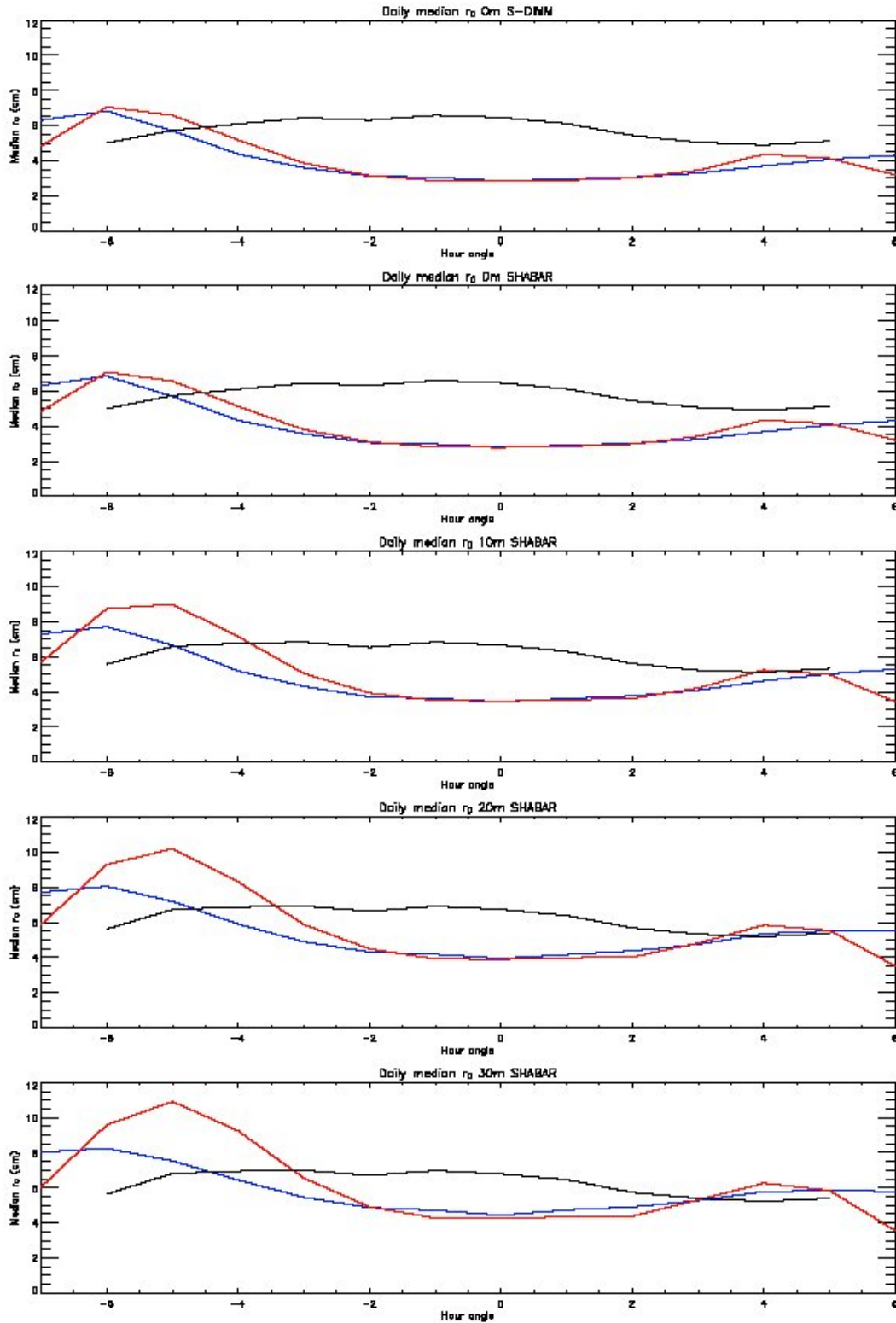


Figure 10.13: As figure 10.12, but showing the median value of r_0 .

10.3 CLEAR TIME

The clear time fraction (CTF) estimated for the three sites is shown in table 10.8, using the two cases of treating the instrument flags:

- Case 1: With instrumental flags considered as cloudy points
- Case 2: With instrumental flags considered as down time points

Also shown are the results of the GONG site survey (Hill et al. 1994) for Big Bear, Haleakala, and Teide (as a proxy for La Palma). The results for Case 2 agree well with the GONG measurements, while the Case 1 estimates are substantially lower. Note that Case 2 is the same approach that was used in the GONG analysis. In reality, it is likely that at least some of the flagged points were indeed cloudy, so the values from the two cases provide lower and upper limits.

Table 10.8: Clear Time Fractions

	Big Bear	Haleakala	La Palma
CTF, ATST, Case 1	0.465	0.574	0.475
CTF, ATST, Case 2	0.712	0.619	0.639
CTF, GONG	0.714	0.647	0.708

These fractions can be used to estimate the total annual number of clear hours at the sites. These can be corrected using the method of section 9.8. Table 10.9 shows the results.

Table 10.9: Estimated Annual Clear Time Hours

	Big Bear	Haleakala	La Palma
Case 1 Raw Hours	2375	2935	2427
Correction Factor	1.411	1.077	1.010
Corrected hours	1684	2725	2402
Case 2 Raw Hours	3638	3162	3265
Correction Factor	1.411	1.079	1.021
Corrected hours	2579	2931	3197

Figure 10.14 shows the average daily dependence of the clear time fraction at the sites.

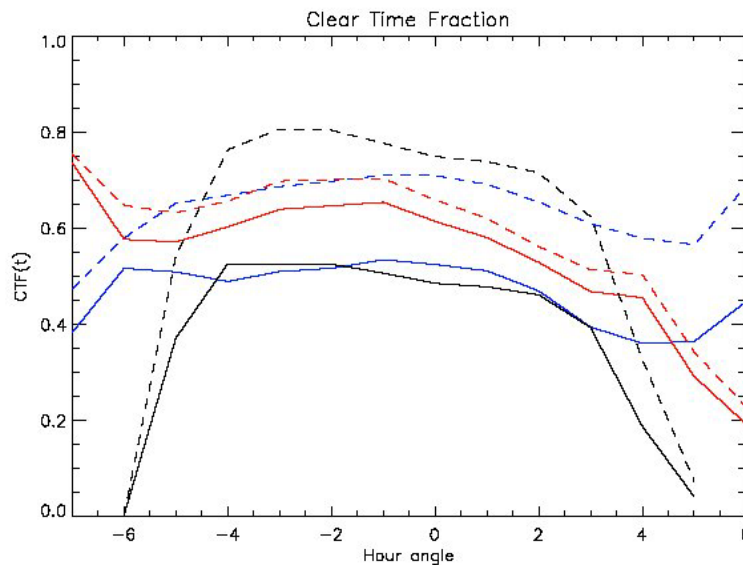


Figure 10.14: The daily variations of the clear time fraction, corrected for cloudy days from the log sheets. Black: Big Bear, red: Haleakala, blue: La Palma. Solid: Case 1, dashed: Case2.

10.4 SKY BRIGHTNESS

10.4.1 Results of the Global Calibration Analysis

The global calibration technique was applied on all the data that was taken from the three sites up through observation on 31 August 2004. The data from Haleakala spanned the largest number of calendar days since the SBM operated there the longest.

10.4.1.1 DISTRIBUTION OF SKY BRIGHTNESS AT EACH SITE

Shown in Figure 10.15 are the distributions of the sky brightness at each site for each wavelength. The scale is logarithmic, and the y-axis is simply the sum of the total number of hours from each site. This is not corrected by the number of days observed nor by any annual sunlight illumination factor. Because the total number of days from each site which is used in this plot is about 200 days, the plots from the three different sites can be compared in a general way.

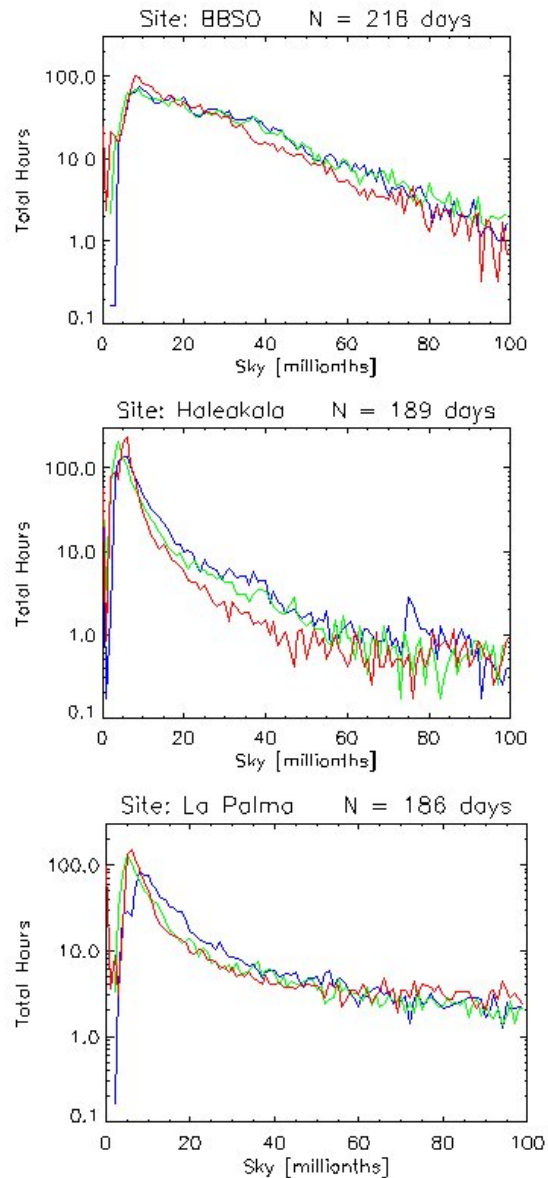


Figure 10.15: Distribution of sky brightness measurements for each site for each wavelength. Blue: 430 nm, green: 530 nm, red: 890 nm.

The distributions of sky brightness at Haleakala and at La Palma are similar, and both are different from the distribution observed at Big Bear. The source of the long tail of bright sky values at Big Bear is not exactly known, but it is consistent with the fact that the atmospheric extinction measured at Big Bear is the largest of the three sites.

10.4.1.2 SAMPLES OF THE BEST SKY AT EACH SITE

Shown in Figure 10.16 are plots of the lowest sky brightness seen at each site during each day of SBM observations. The range of possible instrumental scattered light values is also shown on this plot. The Figure shows that Big Bear has the largest range of best daily sky conditions while Haleakala shows the most consistent best sky conditions during the SBM observing period.

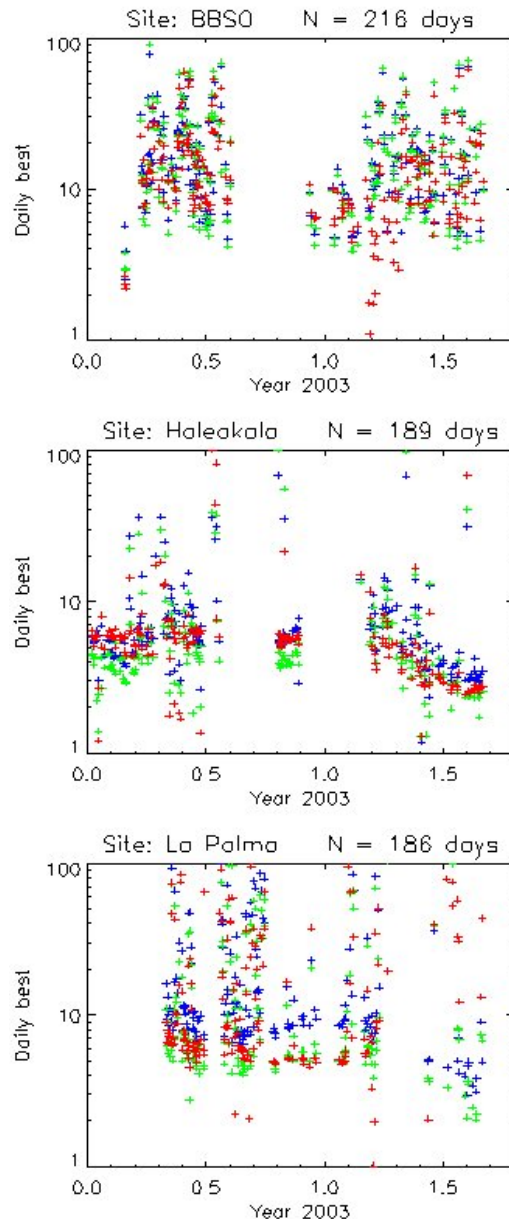


Figure 10.16: The lowest sky brightness value in each wavelength on each day of SBM observations at the three sites.

This plot is also useful to examine to detect any trends which might exist in the instrumental parameters which could affect the global calibration analysis. For example, if the SBM CCD gain degraded over time, or if the transmission of the sky light to the CCD were hindered by dust collecting on the filter, this figure would show a linear trend toward lower sky brightness as a function of time. Such a trend is seen in the Haleakala data taken in the year 2004. The best sky conditions seem to drop from about five millionths in early 2004 to about three millionths later in the year. This suggests that the assumption about constant SBM instrumental response may be incorrect at this level. The data from the other two sites has too much inherent scatter to see if this effect is present with those instruments.

The linear fits from the best coronal days selected for the instrumental scatter determination can also be used to measure the sky brightness, in this case the produce of the atmospheric scatter and the extinction ($\Phi \kappa$) is measured, which represents the increase in the sky brightness in millionths per unit air mass. The values from these fits are shown in Table 10.10 listed as “N = x median”.

Another way to examine the best sky conditions present at the sites is to compare the slope of the sky brightness versus air mass plots which were produced for the instrumental scattered light analysis. Shown in Table 10.10 are the values for this slope, equal to the produce of $\Phi \kappa$ in the previous equation. It shows that while a large range in values exists, the two mountain sites have darker sky (particularly at 890nm) than found at the Big Bear site, during the best days.

Table 10.10: Morning sky brightness per air mass (in millionths) for sample best days

Site – Date	450nm	530nm	890nm
Big Bear 15 May 03	13.97	12.71	5.06
19 May 03	10.47	8.49	1.39
24 May 04	8.17	6.05	2.35
22 Jul 04	0.91	-0.31	-1.65
04 Aug 04	10.45	8.97	5.34
N=86 median	9.65	10.56	8.95
Haleakala 8 May 03	3.79	2.87	1.24
15 May 03	2.43	1.75	0.78
19 Mar 04	3.37	2.38	0.82
8 Jun 04	2.23	1.40	0.33
10 Aug 04	1.65	0.99	0.19
N=104 median	2.06	1.54	0.81
La Palma 5 May 03	5.64	3.82	1.67
26 May 03	3.17	2.09	0.78
7 Jul 04	3.62	2.43	0.23
3 Aug 04	22.55	15.2	2.42
20 Aug 04	2.48	1.57	0.24
N=75 median	4.35	2.84	1.09

10.4.1.3 THE MEDIAN SKY AT EACH SITE

The entire SBM data set from each site in each wavelength was grouped into bins of 0.1 air mass, from an air mass of 1.0 to 4.0, and the median of each bin was taken. This can be used to examine the typical conditions at the site. If the daily variation in the sky brightness dominates the variation seen at the site, then we should see a linear trend in the sky brightness as a function of air mass as mentioned above. However, if the day-to-day variations dominate the daily variation, we may not see any trend with the sky brightness as a function of air mass.

Shown in Figure 10.17 is the median sky brightness as a function of air mass for the three sites for each wavelength. A linear fit is made to each set of points, and the fit coefficients are listed in Table 10.11. From these coefficients we can determine a value for the instrumental scatter (intercept) as well as the median sky brightness per air mass (slope). For the Big Bear data, the intercept values for the fits do not correspond well with the values previously computed for the instrumental scatter, and the sky brightness at 450nm seems to decrease slightly with air mass. It is likely that the temporal variations dominate the air mass variation in the data, and that we should not expect a simple relationship for this site. This is supported by the fact that when just the morning observations from Big Bear are analyzed in a similar method, the fit is much better; perhaps changing atmospheric conditions in the afternoon dominate the variations. The data from the other two sites does show linear trends in the sky brightness as a function of air mass, and intercept values that roughly agree with the expected instrumental scatter. It is likely that the slopes in these values then represent the median sky brightness conditions during the SBM observations at these sites.

Table 10.11: Fits to the median sky brightness versus air mass (intercept, slope)

Site	450nm	530nm	890nm
Big Bear	26.27, -0.78	22.44, 0.84	7.89, 6.55
Haleakala	1.83, 2.17	1.47, 1.64	3.39, 0.83
La Palma	-1.90, 10.34	-3.36, 9.58	1.84, 5.39

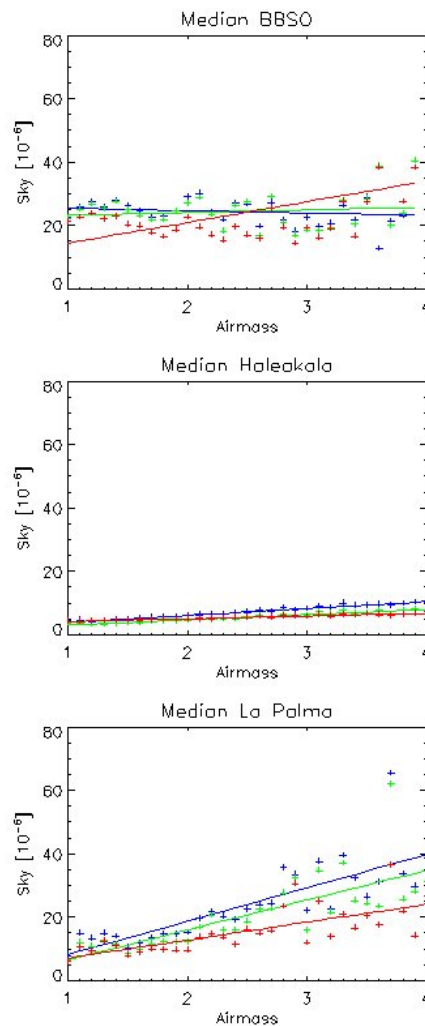


Figure 10.17: Fits to the median sky brightness binned in increments of 0.1 air masses.

10.4.2 Extrapolation from the IR requirement to measured values

10.4.2.1 MEASURED VALUES OF RADIAL SLOPE AND COLOR

In observations with good central neutral densities when the solar disk position can be determined the radial slope of the sky brightness can be measured. Here the sky brightness is fit with a power law in radial distance, $I_{\text{sky}} = I_0 (R/R_{\text{sun}})^{-\gamma}$. Shown in Figure 10.18 are the distributions of the measured radial sky brightness exponent from 2ND2 data from 2004 and from ND4 data in May 2003. The 2004 data from La Palma suffers from low counts and the power law fits are not very good.

The color of the sky brightness can be measured using a power law in wavelength as discussed before where $I_{\text{sky}} = I_0 \lambda^{-\beta}$. This is probably more accurate when the local calibration technique is used, but is in theory possible for all the observations. The color power law exponent was calculated only for 2ND2 and early ND4 observations during the same periods as the radial slope calculations. The distributions of values are shown in Figure 10.19, and again the 2ND2 data from La Palma suffer from low counts due to a short instrumental exposure time. (Note: there are just 20 days during that time period).

Median values were computed from the distributions shown in Figures 10.18 and 10.19, and the values for these medians and an estimate of the error based on the width of the distributions is shown in Table 10.12. These values are used to compute the infrared sky brightness; this process of course assumes constant sky color and radial intensity behavior throughout the year.

Table 10.12: Sky radial and color power law exponents and scale factor

Site	Radial (γ)	Color (β)	$(5.45)^\gamma (.89)^\beta$
Big Bear	2.20 +/- 0.17	0.32 +/- 0.4	40 +/- 9.0
Haleakala	1.03 +/- 0.17	0.53 +/- 0.4	5.4 +/- 1.2
La Palma	1.92 +/- 0.57	0.51 +/- 0.4	21 +/- 16

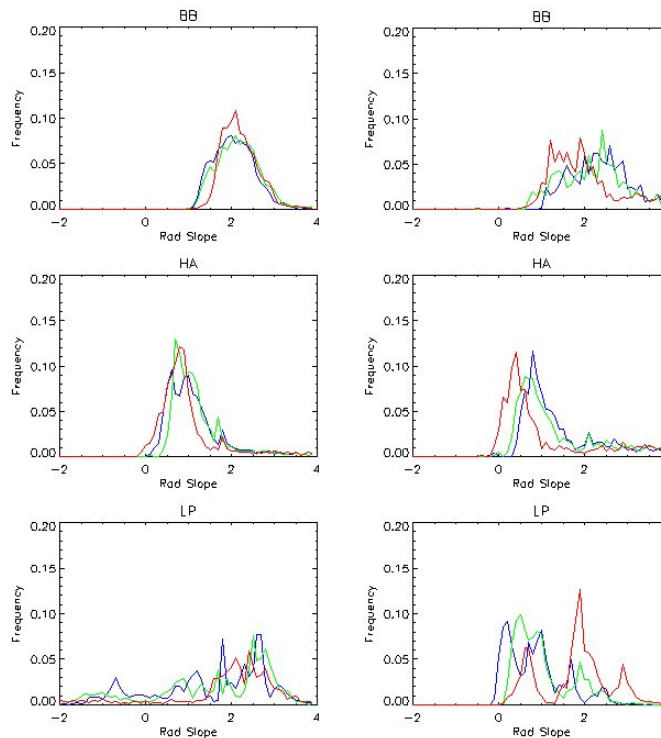


Figure 10.18: Distribution of the radial gradient for the sky brightness measured in 2004 (left column) with the 2ND2 occulter and in May 2003 (right column) with the ND4 occulter.

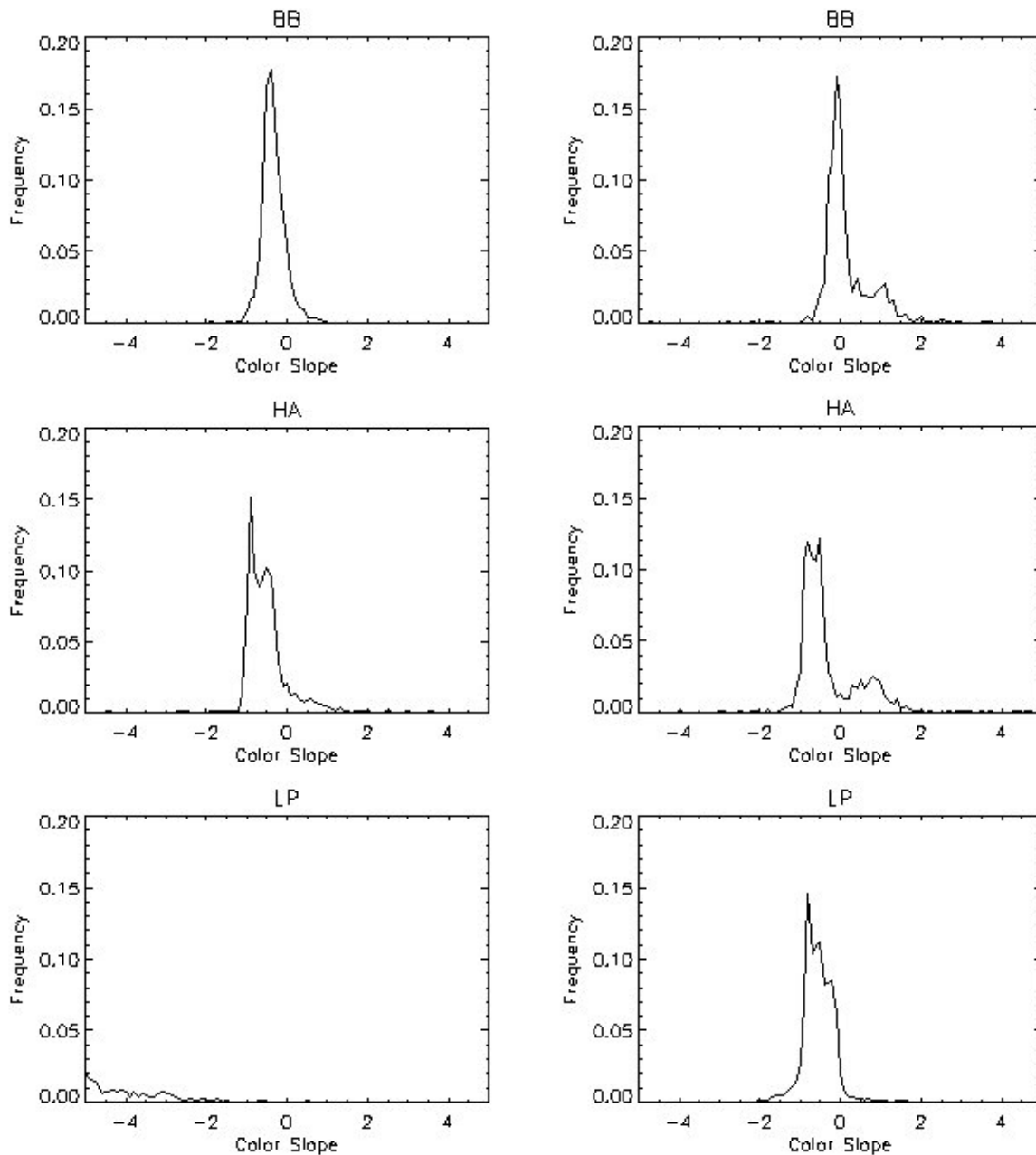


Figure 10.19: Distributions of the exponent of the color power law for the mean sky brightness for the 2ND2 2004 data (left column) and the May 2003 ND4 data (right column). The sky brightness values in 2004 at La Palma with the 2ND2 filter suffered from very short exposure times at 890 nm and give spurious power law fits.

10.4.2.2 THE INFRARED SKY BRIGHTNESS EXTRAPOLATED TO $1.1R_{\text{SUN}}$

Shown in Figure 10.20 is the integrated distribution of the computed sky brightness at 1.1 solar radii at 1000 nm. As can be predicted from Table 10.12, the largest changes are seen in the Big Bear and La Palma distributions, whereas the Haleakala distribution is altered less, compared to the 890 nm data. The two dashed lines are produced by assuming that the Haleakala scale factor should be applied to the Big

Bear and La Palma data sets (rather than the scale factor computed in Table 10.12) and that the instrumental stray light at Big Bear at 890 nm is equal to the Haleakala instrument value and the La Palma stray light is 3.1 millionths at 890 nm. Both of these dashed lines then represent a best-case scenario for the extrapolation of the La Palma and Big Bear 890 nm sky brightness measurements.

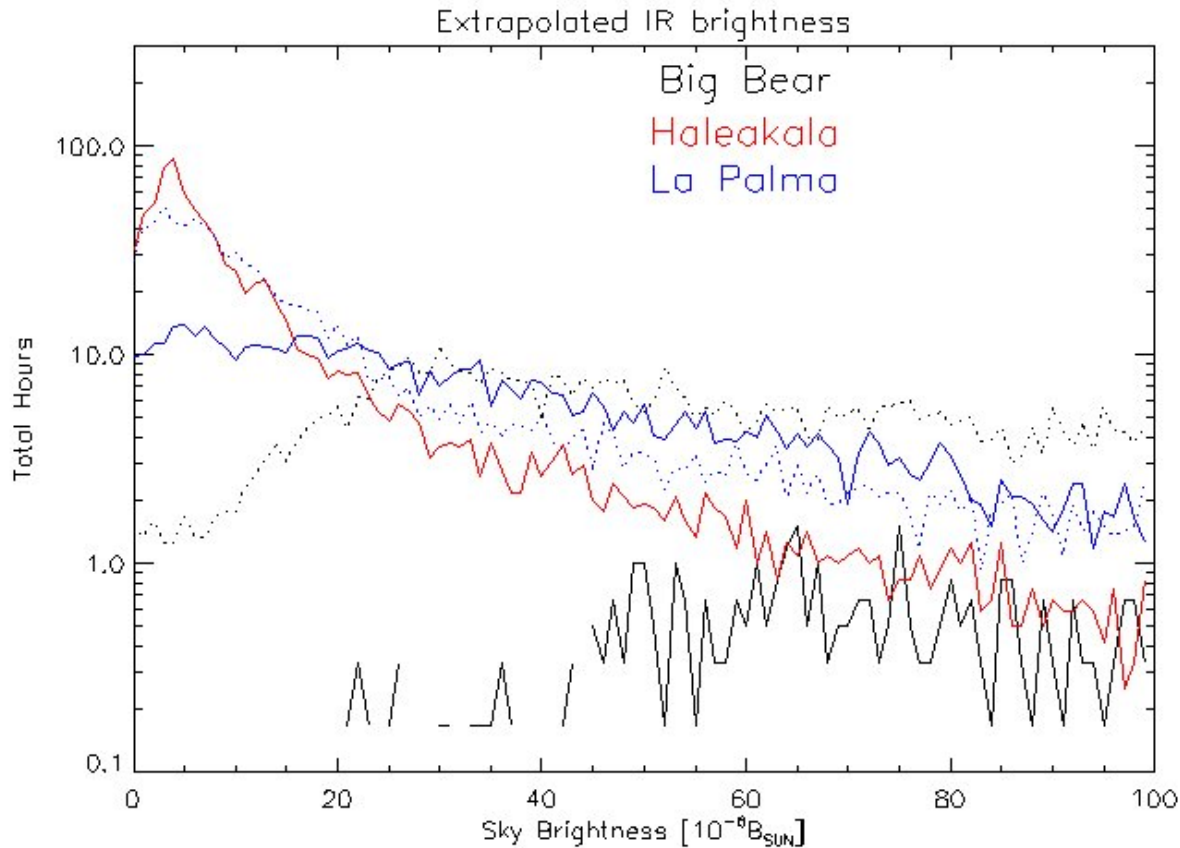


Figure 10.20: Sky brightness measurements from each site extrapolated from 890 nm to 1000 nm, and from about 6 solar radii to 1.1 solar radii. The units are in total hours from each site and are not corrected for instrumental down time or different durations of SBM observations at the sites. The solid lines represent the data scaled by the factors listed in Table 10.12. The dashed lines for Big Bear and La Palma represent “best case” extrapolation scenarios, where the Haleakala scale factor is used.

10.4.3 Comparison with Sky Brightness Goals

Only a simple correction for instrumental down time is applied here. Referring to Section 9.8, if the instrumental down-time is computed on a daily basis rather than by hour, the factor N_{tot} simplifies to just the total number of days that the instrument was up. To compute the annual hours at each sky brightness, we simply multiply the total number of hours by $(365/N_{\text{up}})$ where N is the number of days the SBM instrument was operational (including cloudy days) at each site.

In Table 10.13 the number of days where the instrument was operational at each site is shown, and the correction factor is computed.

Table 10.13: Annualizing facts for SBM observations

	Big Bear	Haleakala	La Palma
Span	03/2/25-04/8/31	03/1/3-04/8/31	03/4/23-04/8/31
Total Days N	554	607	497
SBM up N_{up}	356	260	283
SBM down N_{down}	198	347	214
Scale Factor ($365/N_{up}$)	1.025	1.404	1.290

Table 10.14 shows information about the number of images and the total observing time at each site. Note for most of the SBM observations, the SBM image cadence at Big Bear was 10 minutes, while at the other two sites it was 5 minutes.

Table 10.14: Other facts about SBM observations

	Big Bear	Haleakala	La Palma
N_{days}	216	189	186
N_{best}	86	104	75
N_{scans}	12759	15547	20108
N_{images}	51036	62188	80432
N_{hrs}	2126.5	1295.6	1675.7

A total of 193656 images were taken which comprised 29.75 Gbytes of raw data.

Figure 10.21 shows the integrated histograms for the annually corrected extrapolated infrared sky brightness at all sites. The dashed lines show the “best-case” scenarios for Big Bear and La Palma where the radial power law measured with the Haleakala SBM is used instead of the radial power law measured at those two sites. The point at sky brightness of 25 millionths and 480 annual hours represents the ATST requirements goal value, and the horizontal bar represents the error bar stated in the ATST requirements document.

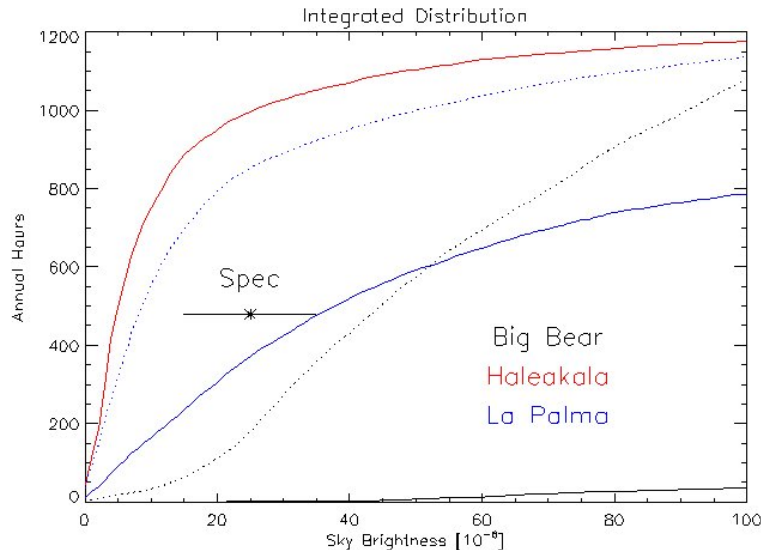


Figure 10.21: Integrated sky brightness distribution for each site after correcting for the instrumental down times. The number of annual hours at or below a given sky brightness is plotted for the extrapolated sky brightness at 1.1 solar radii at 1000 nm. For Big Bear and La Palma two lines are shown; each solid line extrapolates to the IR value using the sky brightness radial power law measured using the SBM at the site and the dashed line extrapolates using the power law measured at Haleakala. The dashed lines are considered a best-case scenario for these two sites.

The figure shows that the Haleakala site exceeds this spec; the La Palma site meets the spec or exceeds the spec depending on the radial exponent which is used, and the Big Bear site does not meet the spec even with the most optimistic radial extrapolation.

Table 10.12 lists the median values for the measured radial slope from each site. Each site meets the ATST spec of 0.8 for the radial slope power law.

The number of continuous four hour blocks was estimated as simply the number of days with one four hour block of sky brightness at or below the level of 25 millionths at 1000nm at 1.1 Rsun. The actual criterion was that the sky brightness for 95% of the time samples within the four hour block were below the threshold value, so if 3 points were actually above the threshold the block would still be counted. It is possible that one day would contain two four-hour blocks, but this is unlikely given the strong dependence of the sky brightness on hour angle. The range of values shown for La Palma and Big Bear are computed based upon the two types of radial extrapolation which were used. Finally the number of blocks observed with the SBM was multiplied by the factors for each site to compute the annual number of blocks. Both Haleakala and La Palma meet the goal of having 40 continuous 4-hour blocks annually, and Big Bear does not meet this goal.

Table 10.15 shows some median values for each site.

Table 10.15: Median values

	Big Bear	Haleakala	La Palma
Time Start	03/2/25	03/1/3	03/3/23
Time End	04/8/31	04/8/31	04/8/31
N days	216	189	186
N valid pts	51036	62188	80432
Median, 1000nm, 1.1Rsun	96-800	5.8	31-114
Median, 890nm, 6Rsun	20	1.1	5.4
Median, 530nm, 6Rsun	21	2.4	11
Median, 450nm, 6Rsun	19	3.1	14
Median β	2.20	1.03	1.92
Median γ	0.32	0.53	0.51
Median 940nm κ	0.12	0.10	0.09
Corrected Annual Spec Hrs	2 – 198	1004	384 – 861
Number Annual 4hr blocks	0 – 4	212	62 – 107

10.4.4 Caveats and Future Work

Several more items could be investigated using this data if given enough time.

10.4.4.1 COMPARISON WITH VISUAL PHOTOMETER DATA

The visual sky photometers (VSP) built by Evans were shipped to the three sites and data was taken during SBM observations. The idea was to directly compare the visual observations (taken in the green) with the 530nm channel SBM observations taken at the same time. The original idea was to verify that no blunders were being made in the SBM sky brightness measurements, and that “coronal” conditions as measured with the SBM corresponded to “coronal” conditions measured with the Evans VSP.

While being shipped to the various sites the VSP instruments suffered misalignments, and although a cross-calibration was performed before the instruments were shipped, the shipping misalignments

probably undid the calibration efforts. Data taken at Haleakala and BBSO shows that the VSP instruments measure different sky values than the SBM, but that the sky intensities are correlated. Data taken from La Palma does not show such a correlation, and it is thought that the VSP shipped to La Palma has become seriously misaligned.

While the sky brightness measurements with the SBM and VSP are correlated, unfortunately they show different slopes. Figure 10.22 shows that when the SBM measures an increase in the sky brightness, the VSP only measures half of that increase. Figure 10.23 shows that during the calibration of the SBM instrument at Haleakala, the relationship was inverted.

The current conclusion is that the VSP measurements have trouble from possible misalignment of the instrument, and from the visual nature of the measurement. It is felt that the SBM data is much more reliable and certainly more linear in its response to the true sky brightness. The comparison between the VSP and SBM doesn't show any blunders, and for a detailed comparison linking the SBM data with historical VSP records at these sites, a much more detailed cross-calibration of the two instruments is required.

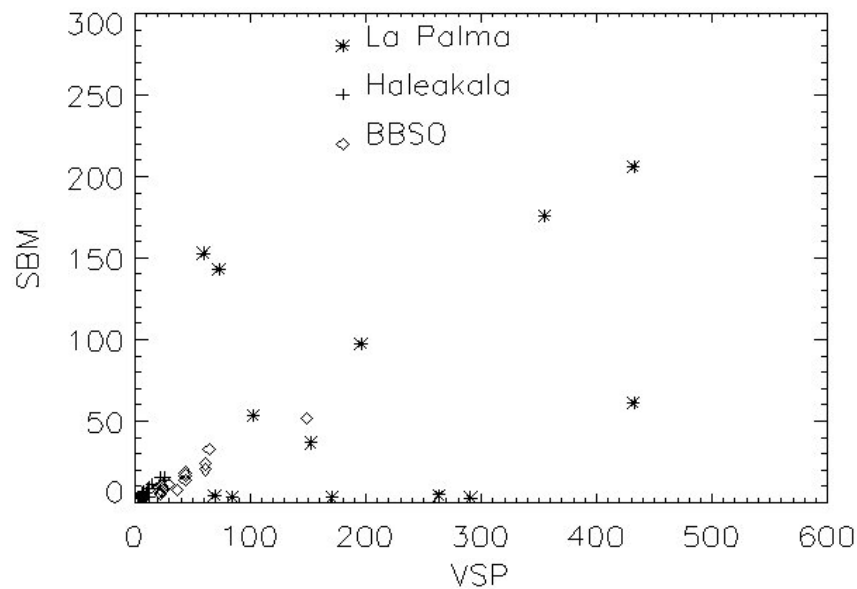


Figure 10.22: Comparison between the VSP and SBM sky brightness measurements at the three sites.

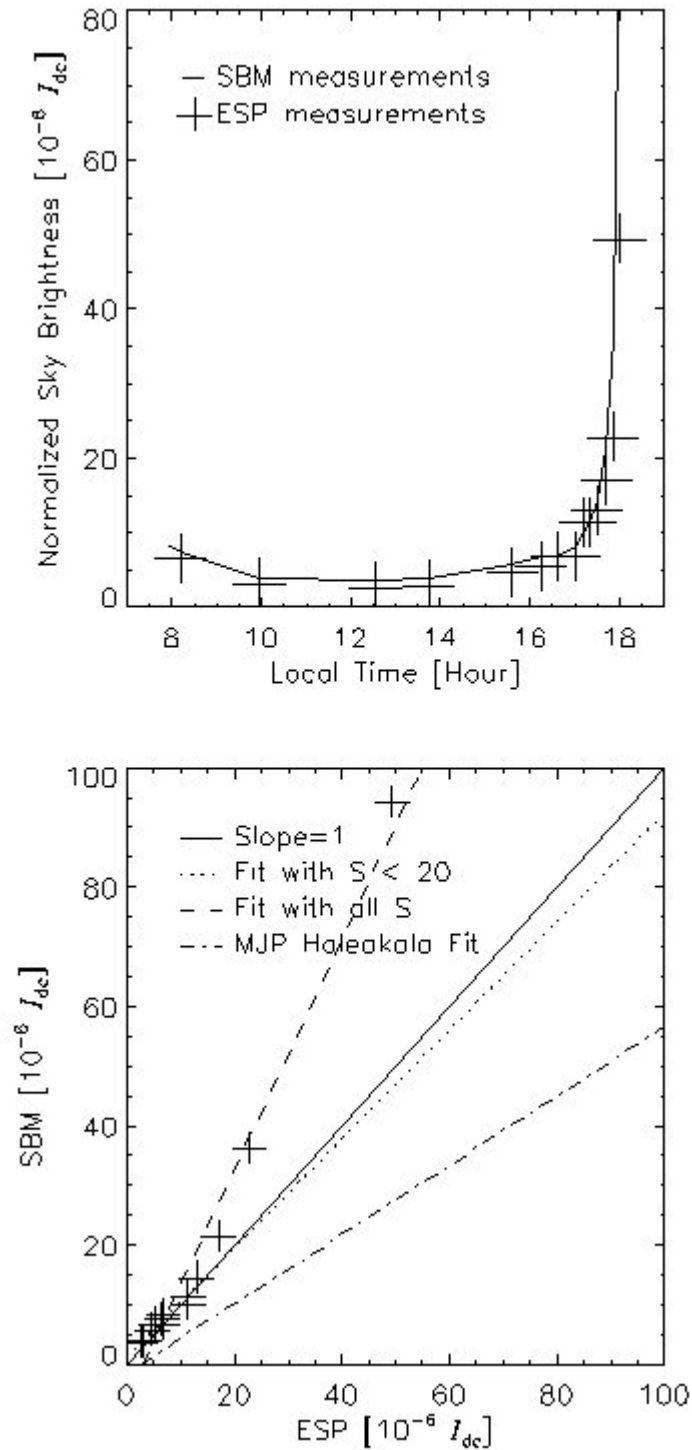


Figure 10.23: Original calibration data from SBM and VSP (listed as ESP on the x-axis) during early tests at Haleakala. The relationship shows a slope=2 value, whereas data taken in 2004 shows a slope=1/2 value. It is thought that the VSP measurements are very sensitive to instrument alignment and observer bias.

10.4.4.2 SBM INSTRUMENTAL SCATTERED LIGHT: POST EXPERIMENT TESTING AT HALEAKALA

A study of the instrumental scattered light after the experiment is complete at one site would help to confirm the stray light values. The instruments should be shipped to Haleakala, where apparently the most consistent sky conditions are found, in order to make a side-by-side test of the SBMs.

The radial variation of the instrumental scattered light has not been accounted for when computing the radial power law values. Although this was originally done in the SBM data analysis paper, the value obtained for Haleakala at that time was about 0.2, as compared with a value near 1.1 for this study. This value has a large bearing on the extrapolated, near sun IR sky brightness which is computed. An addendum to this report is in preparation discussing this issue. A cross-comparison test would help to solve this problem.

The color power law obtained in this study is also not corrected for instrumental stray light. While this has a much smaller influence on the extrapolated near sun IR sky brightness, it would be good to understand this parameter more fully. Again, cross-calibrations at a site with consistent sky brightness conditions would help.

10.4.4.3 SECOND ORDER ANNUAL CORRECTION

The ATST site survey seeing data has been corrected with a second order annualization routine that is more detailed than the values used herein. The sky brightness measured at the sites is a very strong function of air mass, and therefore time of day, so there may be correlations between the observing window at each site and the sky brightness there. A second order correction would hope to remove that correlation from the prediction of the annual hours of sky brightness.

Figure 10.24 shows plots of the measured sky brightness as a function of hour angle at each site, and also the number of observations from each site at each hour angle (the data is binned in hour angle bins of width 1.0). A more detailed analysis of this data using this relationship would help.

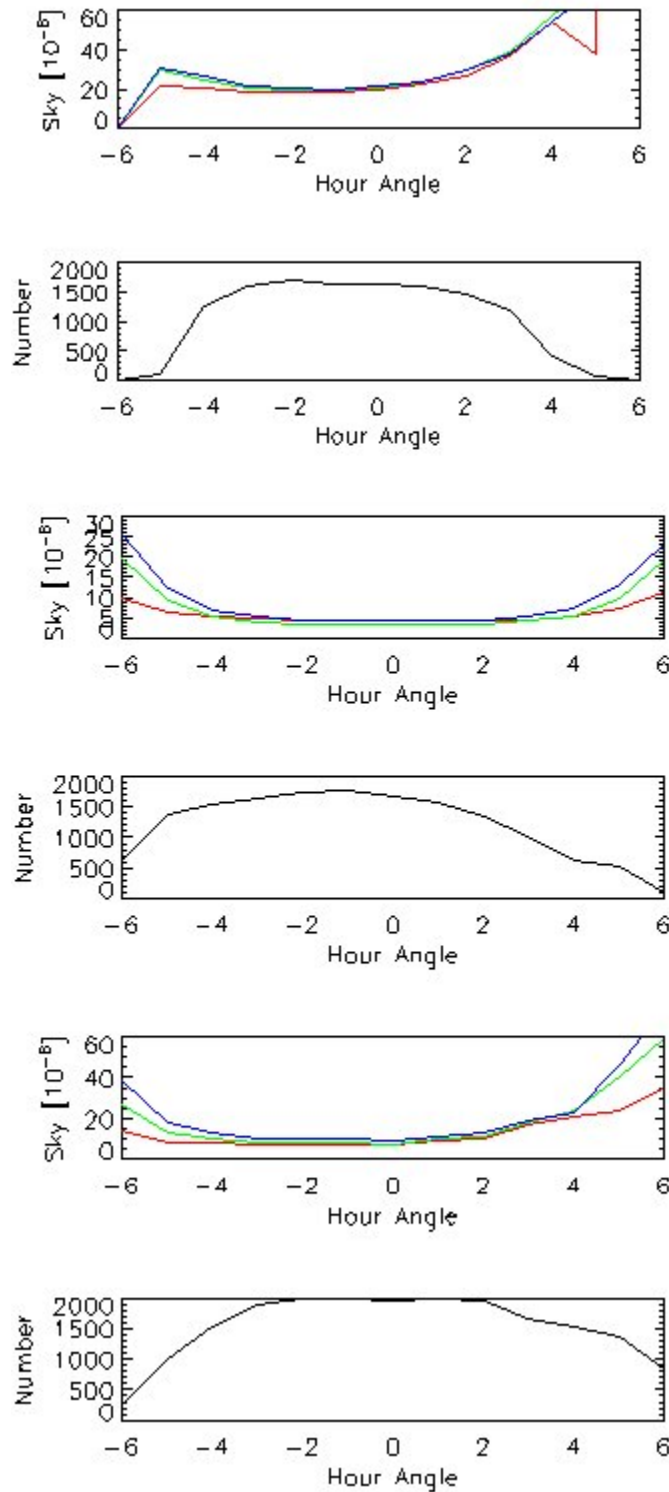


Figure 10.24: Presentation of the sky brightness as a function of hour angle from each site shown for all three wavelengths. The measured sky brightness is a strong function of hour angle (due to changing air mass). Below the colored graph in each case is the number of observations in each hour angle bin from the sites. From the top the sites are BBSO, Haleakala and La Palma.

10.5 WATER VAPOR

A simple proxy for the water vapor absorption is computed for the May 2003 and the 2004 2ND2 filter data. The extinction at 890nm was simply subtracted from the extinction value at 940 nm; this procedure differs slightly from the previous procedure used for the six-site study by the small factor of 1.054^α where α is the power law exponent for the extinction versus wavelength behavior.

The distributions of this extinction difference are shown in Figure 10.25. As with the sky brightness color power law exponent, the 2004 2ND2 distribution for the La Palma water absorption significantly varies from the 2003 La Palma distribution. It is ignored due to the fact that there are low counts in the 890 and 940 nm 2ND2 La Palma data, and that there are only 20 days of observations. Only the May 2003 data is used for the La Palma median calculation, which is shown in Table 10.15 along with the median values for the other sites.

It is not a simple feat to compute the atmospheric precipitable water vapor from this water absorption factor. There is a non-linear relationship between the two values, and this must be modeled with atmospheric absorption spectra and the SBM 940 nm filter profiles. This task has not yet been done.

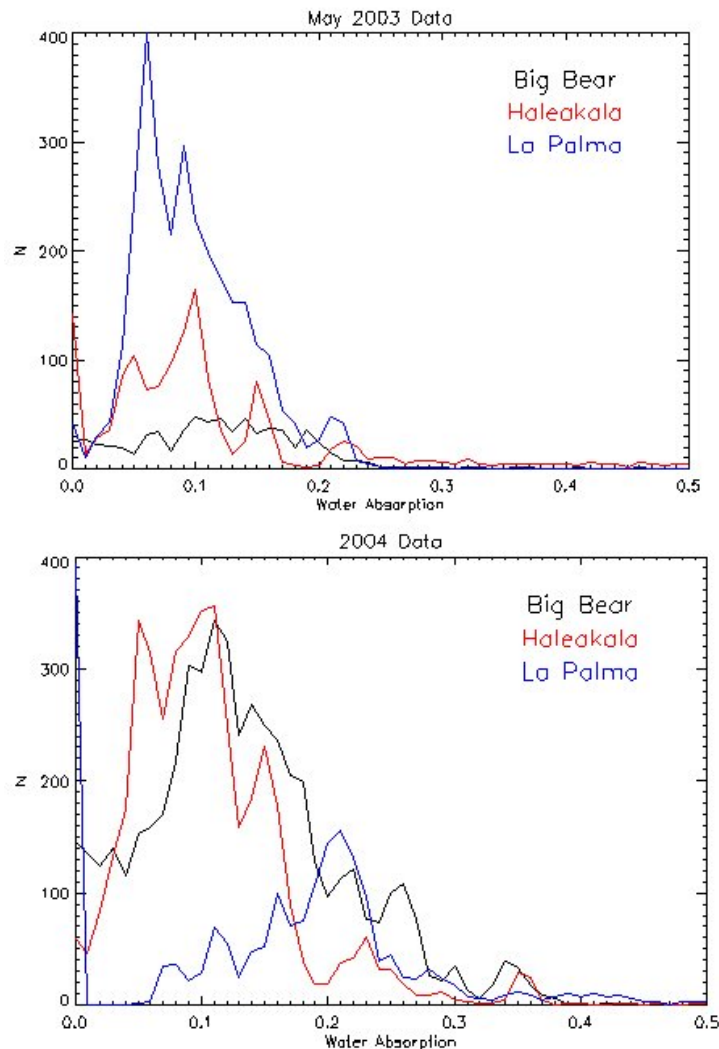


Figure 10.25: The distribution of water absorption coefficients at the three sites for the ND4 2003 data and the 2ND2 2004 data. The low counts in the La Palma 2ND2 data likely explain the strange distribution for that data.

10.6 DUST

The dust counter obtains a sample every 10 minutes. These numbers have been analyzed to provide the statistical distribution for each of the five particle sizes at all six sites. The detailed distributions are provided in Appendix 13.14. The medians are contained in table 2 in the Executive Summary. Figure 10.26 provides an example of the temporal behavior of dust during August 2003 at Big Bear.

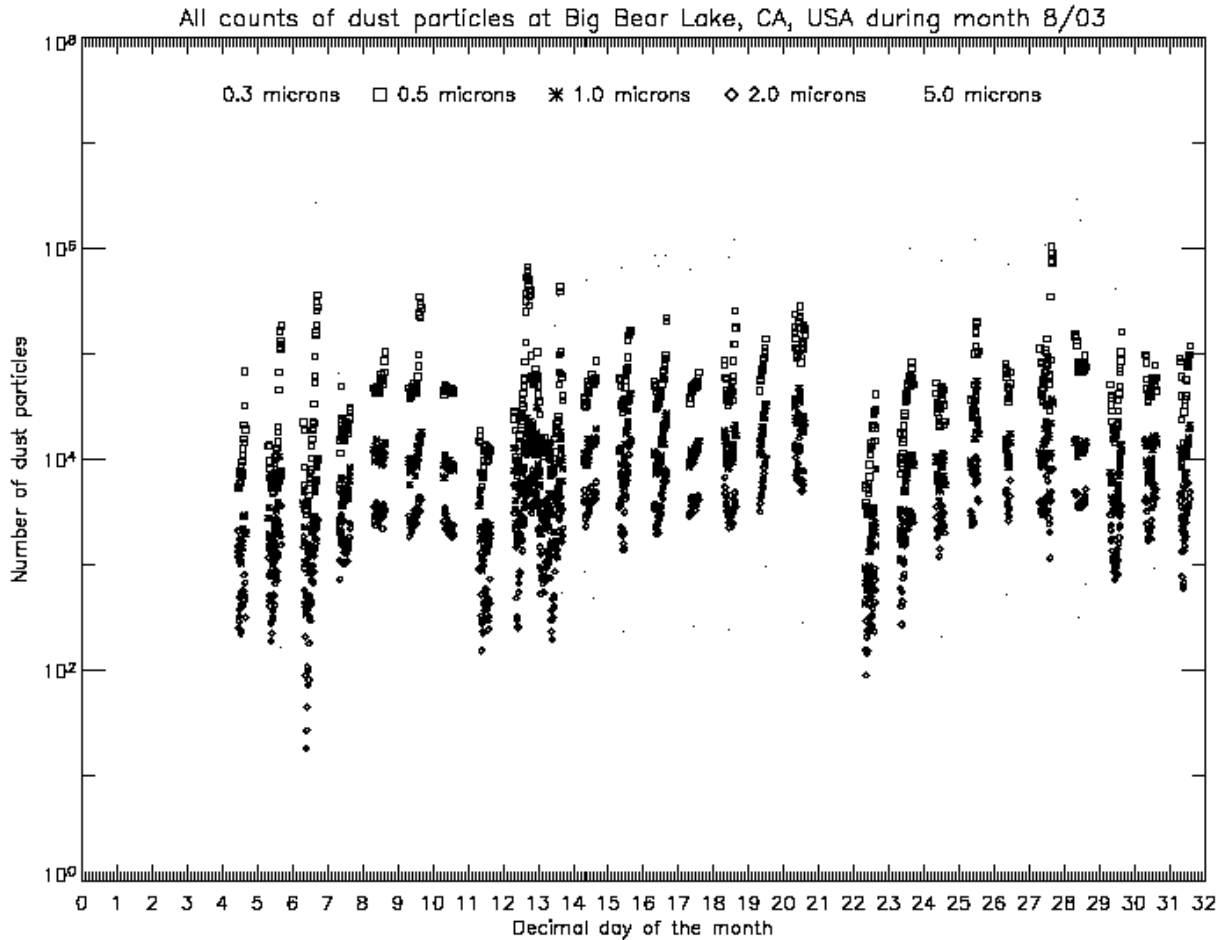


Figure 10.26: An example plot of the dust counts during August 2003 at Big Bear.

10.7 METEOROLOGY

Detailed weather results can be found in Appendices 13.12 and 13.13. Here we present an overview summary of the median quantities.

	Big Bear	Haleakala	La Palma
Median wind Speed (m/s)	4.7	4.5	3.6
Maximum wind gust (m/s)	26	53	25
Median wind direction azimuth (0: N, 90: E)	247	292	247
Median ground temperature (F)	62	57	51
Median tower temperature (F)	57	52	51
Median temperature gradient (top-base) (F)	-5	-4	0

10.8 CONCLUSIONS

The ATST site survey is one of the few comparative studies of solar site characteristics to be carried out with consistent instrumentation and analysis methods. It incorporates a new technique of combined differential image motion and scintillation measurements to estimate the seeing and the structure function over a range of heights. The survey also includes a multi-band miniature coronagraph to estimate sky brightness and water vapor content.

This effort has produced a considerable data base of information on the six sites tested. While some issues remain concerning the reliability of the seeing analysis method and the length of time spanned by the survey, the ATST Site Survey Working Group believes that the information in this report will provide useful input to the ATST site selection process

11. ACKNOWLEDGMENTS

This survey is a substantial undertaking, involving approximately 50 people. Their names are mentioned in the list of contributors, the Site Survey Working Group section, and the technical staff sections. In addition to those dedicated people, the ATST SSWG would like to thank the Big Bear Water District Board, the Dixie National Forest Service, Dan Weedman, Gloria Koningsberger, Ed Seykora,, Goran Scharmer, and Rob Rutten.

12. REFERENCES

Beckers, J. M., 2001, *Exp. Astron.* **12**, 1.

Brandt & Wöhl, 1982, *A&A* **109**.

Hill et al, 1994, *Solar Phys.* **152**, 351.

Hill, F., Beckers, J., Brandt, P., Briggs, J., Brown, T., Brown, W., Collados, M., Denker, C., Fletcher, S., Hegwer, S., Horst, T., Komsa, M., Kuhn, J., Lecinski, A., Lin., H., Oncley, S., Penn, M., Rimmele, T., Socas-Navarro, H., and Streander, K. 2004: SPIE Proc. **5489**, submitted: Solar site testing for the Advanced Technology Solar Telescope.

Kuhn, J., Waterson, M., Northcott, M., Maberry, M., nd Tokunaga, A., “A Comparative Look at the Atmospheric Optical Characteristics of Haleakala”, AMOS conference paper, 2002.

Labonte, B. J., 2003, *Solar Phys.* **217**, 367.

Oncley, S., and Horst, T., “Calculation of Cn² for visible light and sound from CSAT3 sonic anemometer measurements”, 2004, available at <http://www.atd.ucar.edu/homes/oncley/bao2004/background.pdf>.

Press et al, *Numerical Recipes*

Wesely, 1976, The combined effect of temperature and humidity fluctuations on refractive index, *Journal of Applied Meteorology*, V 15, 43-49

Zirin & Mosher, 1985, *Solar Phys.* **115**, 183.

13. APPENDICES

13.1 SEEING INSTRUMENTATION PAPER (EXP. ASTRON,)

13.2 CN2 ANALYSIS REPORT (RPT-0014)

13.3 HECTOR'S INTEGRAL

13.4 CRANE TEST DETAILS

13.5 HALEAKALA STELLAR DIMM DATA

13.6 SBM INSTRUMENTATION PAPER

13.7 SBM ANALYSIS PAPER

13.8 VSP CALIBRATION

13.9 QUICK-LOOK PLOT EXAMPLE

13.10 LA PALMA HEIGHT COMPARISON

13.11 DEPENDENCE OF SEEING ON SEASON, TIME OF DAY, WIND SPEED, WIND DIRECTION

13.12 WEATHER STATISTICS

13.13 HIGH-ALTITUDE WINDS

13.14 DUST STATISTICS